Preparations for the Mu3e experiment: Magnet commissioning, beamline studies and a study of fake tracks

Ioannis Paraskevas

Department of Physics & Astronomy

University College London

Submitted to UCL in fulfilment of the requirements for the award of the degree of **Doctor of Philosophy**

December 20, 2021

Declaration

I, Ioannis Paraskevas confirm that the work presented in this thesis is my own. Where information has been derived from other sources, I confirm that this has been indicated in the thesis.

Ioannis Paraskevas _____

Abstract

The Mu3e experiment at the Paul Scherrer Institute in Switzerland will search for the rare decay of a positive muon to two positrons and one electron. Phase I of the experiment aims for a sensitivity of one in 10^{15} muon decays and Phase II aims for a sensitivity of one in 10^{16} muon decays which is four orders of magnitude better that previous experiments. The Standard Model process $\mu^+ \rightarrow e^+e^-e^+$ via a neutrino loop is suppressed to unobservable levels $O(< 10^{-50})$ and does not play a practical role. Therefore, any measurement of this decay would be a clear sign of new physics. To achieve its goal, Mu3e relies on a high rate of muons being detected in a spectrometer with a wide kinematic acceptance, excellent momentum and vertex resolutions and precise timing information. As of September 2021, data taking is expected to begin in 2022 at a muon rate of 10^8 μ^+/s. The full rate of $2 \times 10^9 \mu^+/s$ will not be reached before 2026. The main subject of this thesis is the preparations for the experiment which include the magnet commissioning, a magnet simulation, beamline simulation studies, beam measurements at the πE5 beamline and an analysis of fake tracks in simulation.

Impact Statement

Scientific research increases our understanding of the world around us. The Mu3e experiment at PSI, will try to make very precise measurements to establish the presence of new physics beyond our current theories. The work described in this thesis has a direct contribution in the preparations for the experiment. At the time of writing this thesis, Mu3e is in the preparation phase and probably a year before the start of Phase I data taking. Preparations include the magnet commissioning and testing of the system, a magnet simulation, beamline simulation studies, beam measurements at the πE5 beamline and a study of fake tracks in simulation. Beamline simulation studies were conducted in order to optimise the available beam rate for the experiment and in May/June 2021 the first ever beam measurements were carried out at the centre of the magnet, using the complete beamline setup. If signs of new physics are observed, it will be one of the biggest fundamental discoveries so far in the field of experimental particle physics of the 21st century. As has been the case in the past, fundamental discoveries in particle physics were later able to significantly benefit humanity technologically, beyond their original scope of research. For example, proton therapy is now an established procedure to cure cancer, with its origin rooted in particle accelerators. There is one famous story with Michael Faraday and the usefulness of scientific discoveries which appears in various forms in the works of the 19th and 20th century writers. As the story is usually told, the prime minister of the United Kingdom or some other senior politician was given a demonstration of electromagnetic induction by Faraday. When asked “What good is it?” Faraday replied: “One day, Sir, you may tax it.”. It remains to be seen what other technological advancements will be enabled by new physics.

Acknowledgements

First and foremost I would like to express my deepest gratitude to my supervisor, Dr. Gavin Hesketh, for always being available for questions, helpful discussions and advice. Gavin, I greatly value all the advice and encouragement that you have given me over the last four years. This work would have not been possible without your support. Thank you!

I am also grateful to Dr. Andreas Knecht for his support and discussions throughout my stay at PSI. Andreas, it was a pleasure working with you and thank you for giving me the opportunity to learn new things on the magnet and beamline of the experiment. I have learnt so much from you.

Many thanks to all members of the Mu3e collaboration and my fellow PhD students for the interesting and eventful meetings that took place before the COVID-19 pandemic. It was a pleasure to work with such passionate people. Special thanks to Dr. Frank Meier and Dr. Stefan Ritt for their support during my stay at PSI.

A huge thanks to my best friends who have always been supportive of all my endeavours. Last but not least, I thank my parents, Adamos and Stella, to whom I dedicate this thesis, for their love and encouragement on my path as a physicist.

This thesis is dedicated to my parents.

Contents

List of Figures

List of Tables

List of Acronyms

SM standard model

QFT quantum field theory

BSM beyond the Standard Model

LFV lepton flavour violation

cLFV charged lepton flavour violation

PSI Paul Scherrer Institute

J-PARC Japan Proton Accelerator Research Complex

FNAL Fermi National Accelerator Laboratory

PMNS Pontecorvo–Maki–Nakagawa–Sakata

SUSY supersymmetry

CP charge-parity

LHC Large Hadron Collider

HiMB high intensity muon beam

IC internal conversion

HV-MAPS high voltage monolithic active pixel sensors

SiMP silicon photomultiplier

CERN European organization for nuclear research

MAMI Mainz microtron

DAC digital-to-analog

HV high voltage

SciFi scintillating fibre

DAQ data acquisition

FPGA field programmable gate arrays

GPU graphical processing unit

MIDAS maximum integrated data acquisition system

GM Gifford-McMahon

OVC outer vacuum chamber

CMBL compact muon beamline

HIPA High Intensity Proton Accelerator

APD Avalanche Photodiode

GUI Graphical User Interface

MS multiple scattering

Personal Contributions

This thesis is divided into 4 main parts.

I. Introduction to elementary particle physics & the Mu3e Experiment.

II. Commissioning of the Mu3e magnet system.

III. Simulation beamline studies and beam measurements at the πE5 area at PSI.

IV. Analysis of fake tracks in Mu3e using the Mu3e simulation software.

In experimental physics usually the work of each scientist is built upon the work of tens of other scientists and graduate students. The author's direct contribution to the Mu3e experiment is listed below:

1. ***Commissioning of the Mu3e magnet system.*** I carried out thorough testing of the magnet and various magnetic field profiles were studied. This is presented in chapter 3. In addition to that, I developed a magnet simulation presented in chapter 4.

2. ***Simulation beamline studies and beam measurements at the πE5 area at PSI.*** I studied the effect of a moderator and collimators using a G4beamline simulation, which is presented in chapter 6. The simulation had initially been set up in the past by other members of the collaboration, but I implemented the new elements (moderator & collimators) into the simulation. In May/June 2021, the first ever beam measurements were conducted at the centre of the Mu3e magnet, presented in chapter 7. In particular, I developed the software that controls the brand new APD scanner. The preparations and the analysis of the measurements are the result of a collaborative work produced by Dr. Andreas Knecht (PSI), Giovanni Dal Maso (PSI) and the author of the thesis.

3. ***Fake tracks in Mu3e.*** In Mu3e, decay particles can make several turns inside the central station of the pixel tracker. This can produce fake tracks due to ambiguity in the direction of the track. I carried out the analysis presented in chapter 9, using the Mu3e simulation software which was developed by several members of the collaboration over the last years.

Part I

Introduction

1 | A Theory of Almost Everything

"The first principles of the universe are atoms and empty space;
everything else is merely thought to exist."

(Democritus [1])

The statement above made by Democritus might not hold true today, but it shows us the desire of human kind to search for answers to one of the oldest questions in human history: What are the smallest building blocks in nature? What are we made of? The idea that matter is made up of discrete units is not a new idea as it appears in many ancient cultures. Despite the fact that science has advanced through the centuries and ancient ideas of atoms may not directly apply to our world today, these ideas have always motivated thousands of scientists and philosophers over the last millennia to search for answers to such profound questions. The curiosity of humans eventually led to a successful description of all elementary particles and their interactions, which is known as the Standard Model of Particle Physics (SM). The SM is a quantum field theory (QFT) describing all known matter particles and three of the four fundamental forces: the electromagnetic, weak nuclear and strong nuclear force. It is our current best understanding of fundamental physics describing how particles interact with each other. Mathematically, the SM is a gauge QFT containing the internal symmetries of the unitary product group $\mathrm{SU}(3)_\mathrm{C} \times \mathrm{SU}(2)_\mathrm{L} \times \mathrm{U}(1)_\mathrm{Y}$, with $\mathrm{SU}(3)_\mathrm{C}$ corresponding to the strong interaction and $\mathrm{SU}(2)_\mathrm{L} \times \mathrm{U}(1)_\mathrm{Y}$ being the group for the electroweak interaction. The theory is described by a Lagrangian, containing 26 free parameters whose numerical values are established by experiments. The SM describes the behaviour of a set of quantised fields, corresponding to the known fundamental particles of the Universe. Figure 1.1 shows all the elementary particles of the SM. They are divided into two main categories: ***bosons***

and ***fermions***. In the SM, bosons and fermions are particles with integer spin (0, 1, 2. . .) and half odd integer spin (1/2, 3/2, 5/2. . .) respectively.

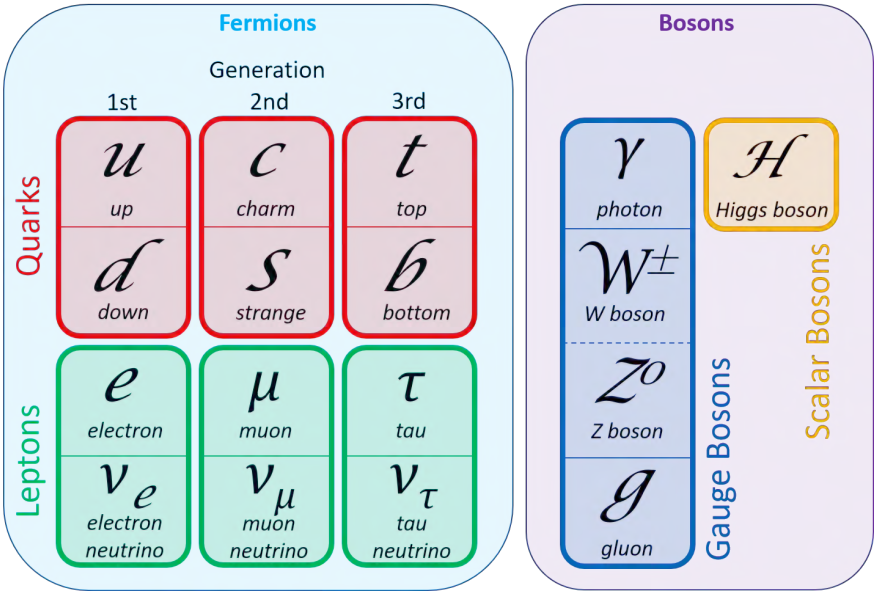

Figure 1.1: Elementary particles and force carriers according to the Standard Model of particle physics.

Bosons are responsible for the interactions between the particles as described below:

- The massless neutral photon mediates the electromagnetic force between electrically charged particles.
- The massive neutral Z and charged W bosons are the force carriers of the weak interaction and couple to particles with weak isospin.
- The massless neutral gluons are the force carriers of the strong interaction and couple to particles with colour charge. All gluons have a colour charge hence they also interact with other gluons.
- The massive Higgs boson interacts with all massive particles.

All elementary bosons have spin-1 hence they are called vector bosons. The only exception is the Higgs boson which is the only known elementary spin-0 boson, hence it is called a scalar boson. Vector bosons are also called gauge bosons and are introduced by requiring gauge invariance of the Lagrangian. An example

of this is the Lagrangian for a free fermion where the fermion-photon coupling is introduced by requiring a local U(1) invariance. The required local gauge symmetry is expressed naturally as the invariance of the Lagrangian under a local phase transformation of the fields:

$$\psi(x) \rightarrow \psi'(x) = e^{iq\chi(x)}\psi(x) \tag{1.1}$$

where $\chi(x)$ is the local phase and ψ are spin-1/2 Dirac spinor fields for the free fermion. The Lagrangian for a free spin-1/2 particle is given by:

$$\mathcal{L} = i\bar{\psi}\gamma^{\mu}\partial_{\mu}\psi - m\bar{\psi}\psi \tag{1.2}$$

This Lagrangian is not gauge invariant, but the invariance can be restored by using the following substitution:

$$\partial_{\mu} \rightarrow D_{\mu} = \partial_{\mu} + iqA_{\mu} \tag{1.3}$$

where A_{μ} is a new field which transforms as:

$$A_{\mu} \rightarrow A'_{\mu} = A_{\mu} - \partial_{\mu}\chi \tag{1.4}$$

This leads to a new gauge invariant form of the Lagrangian:

$$\mathcal{L} = i\bar{\psi}\gamma^{\mu}\partial_{\mu}\psi - m\bar{\psi}\psi - q\bar{\psi}\gamma^{\mu}A_{\mu}\psi \tag{1.5}$$

where the last term corresponds to the interaction between the fermion and the new field, which in the case of the electron is the photon field.

Fundamental fermions are the particles that are the main constituents of matter. These are divided into two categories, ***quarks*** and ***leptons***, as described below:

- All quarks are charged elementary particles (+2/3 or -1/3 of the electron charge) with colour charge which interact via all three forces.

- All leptons are elementary particles possessing no colour charge hence they do not feel the strong interaction. Charged leptons (-1 of the electron charge) interact via the electromagnetic and weak interaction whereas neutral leptons interact only via the weak interaction.

Fermions can be categorised in three generations or families. The first generation of quarks contains the up quark (u) and the down quark (d). Along with the electron (e^-) and electron neutrino (ν_e) which are part of the first generation of leptons, they form the stable matter in our universe. The other two generations consist of heavier unstable particles (essentially heavier copies of the first generation particles) and quickly decay via the weak interaction to the particles of lower generation. In each generation, a flavour number (L_e, L_μ, L_τ) equal to -1 or $+1$ is assigned to each lepton and its antiparticle respectively. Table 1.1 shows an overview of the leptons and their corresponding flavour numbers.

	e^-/ν_e	μ^-/ν_μ	τ^-/ν_τ	$e^+/\bar{\nu}_e$	$\mu^+/\bar{\nu}_\mu$	$\tau^+/\bar{\nu}_\tau$
L_e	+1	0	0	-1	0	0
$L\mu$	0	+1	0	0	-1	0
$L\tau$	0	0	+1	0	0	-1

Table 1.1: Leptons and their flavour numbers.

1.1 Limitations of the Standard Model

The SM has been proven many times to be extremely precise in its predictions. However, various experiments hint that the SM is incomplete, even with the inclusion of massive neutrinos. It is considered as being a low energy limit of a broader theory of beyond the SM (BSM) physics. The exact values of the neutrino masses, as well as their ordering and the mechanism under which they are generated are not described by the SM. Gravity, being one of the four fundamental forces is not part of the SM yet as to this day there is no working QFT of gravity. Observations of the Cosmological Microwave Background indicate that only about 5% of the universe's energy density arises from particles described by the SM [2]. Dark Matter accounts for another 26% completed by 69% Dark Energy. Dark Matter is possibly an indication that there are undiscovered particles in the universe but dark energy remains a complete mystery for now. The lightest supersymmetric particle could be a component of dark matter as there are many theories suggesting it cannot decay to SM particles. Moreover, the SM fails to explain why the universe is dominated by matter and not antimatter, as in principle they must have been created in equal amounts

during the early universe. In 1967, Andrei Sakharov proposed [3] a set of three necessary conditions that a baryon-generating interaction must satisfy to produce matter and antimatter at different rates. The three necessary Sakharov conditions are:

1. Baryon number violation.
2. C-symmetry and CP-symmetry violation.
3. Interactions out of thermal equilibrium.

CP-symmetry states that the laws of physics should be the same if a particle is interchanged with its antiparticle while its spatial coordinates are inverted. Violation of CP symmetry will result in an imbalance between matter and antimatter and this would explain today's dominance of matter over anti-matter in the universe. However CP symmetry predicted by the SM in the quark sector is not enough to explain the whole picture (order of 10^{-3}). The number of fermion generations is another unsolved puzzle in the SM which is established experimentally but there is no theoretical constraint that forbids the existence of more than three generations. New BSM theories could explain and give answers to some of these problems.

1.2 Lepton Flavour Violation

One lepton of particular interest is the muon. Muons are unstable elementary particles and they decay via the weak interaction. They have a mass of 105.7 MeV/c^2 and a lifetime of 2.2 μs. The dominant muon decay channel is called the Michel decay, named after Louis Michel, in honour of his work on muons. This decay has a branching fraction of almost 100% and it is the simplest decay channel, where a muon decays to an electron, an electron antineutrino and a muon neutrino. An additional photon may be radiated with a branching fraction of 1.4% and this photon can then be converted to an e^+e^- pair with a branching fraction of 3.4×10^{-5} [4]. These processes are shown in Figure 1.2.

One of the main goals of particle physicists is to test the SM in order to find new physics and there are two ways to go about this. They can conduct direct searches as performed at the Large Hadron Collider (LHC) at CERN, where the idea is to find new particles and processes by going to previously unprecedented energy scales.

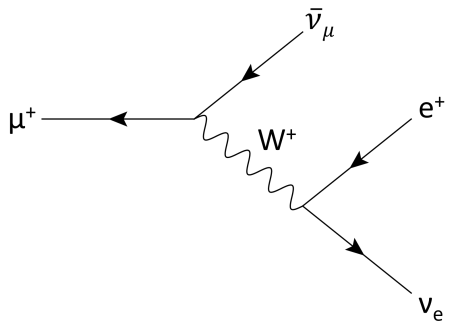

(a) Michel decay.

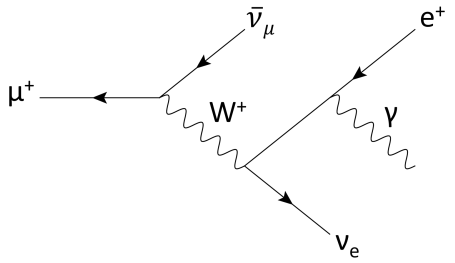

(b) Michel decay with an additional photon.

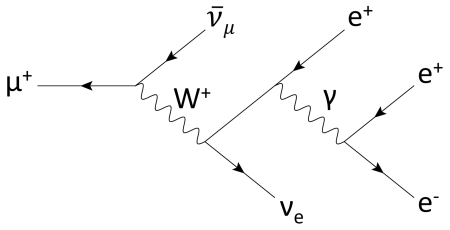

(c) Michel decay with internal conversion to an e^+e^- pair.

Figure 1.2: Muon decay modes.

On the other hand they can also probe for new physics by performing precision measurements, such as trying to detect rare decay modes where the lepton flavour is not conserved. This will be a clear sign that there is new BSM physics [5]. Lepton flavour violation (LFV) is any process where the lepton number is not conserved. Noether's theorem [6] relates any continuous symmetry of the Lagrangian to a conserved quantity. There are however some quantities which seem to be accidentally conserved in nature, one of which is the lepton flavour. Lepton flavour is not a theoretically motivated symmetry of the SM Lagrangian. In fact, physicists back in the 50's introduced the notion of lepton flavours and their conservation due to the absence of LFV in their experiments, in the channels $\mu^+ \to e^+\gamma$ and $\mu^- N \to e^- N$. In the SM it was also assumed that the neutrinos are massless which means that the lepton flavour mixing in both the neutral and the charged lepton sector would be absent. However, the observation of neutrino oscillations by experiments such as SuperKamiokande [7] is a direct proof of LFV in the neutral sector of leptons [8]. Particle physicists have been on the hunt for charged LFV (cLFV) decays for 70 years now. The most sensitive and promising cLFV searches currently rely on

muons. In principle, the tau lepton can also be used to probe for cLFV decays. The higher tau mass should result in a larger effect from BSM physics, but they are hard to make and they also have a very short lifetime, so the measurements are much more challenging. The fact that muons are available in huge quantities at many different places makes muon cLFV searches much more powerful. For the muon, the following channels [9] are of great interest:

- $\mu^+ \to e^+\gamma$. The most recent results for this channel are reported by the MEG experiment, installed at Paul Scherrer Institute (PSI). The experiment stops positive muons on a thin target at the core of the detector where they undergo decay at rest. The event topology of the process consists of a positron and a photon emitted simultaneously back to back with momenta exactly equal to half the muon mass.

- $\mu^+ \to e^+e^-e^+$. The latest limits set on the branching ratio of this channel date back to 1988 and were achieved by the SINDRUM experiment [10]. The Mu3e experiment, which is the successor of SINDRUM, will be described in detail in Chapter 2.

- $\mu^- N \to e^- N$. The experimental signature of this process is very distinct, consisting of a single mono-energetic electron with momentum very close to the muon rest mass. During this process a small fraction of the momentum is absorbed in the recoiling nucleus. The main source of backgrounds to this process are electrons from pion decays originating along the beam line. Several experiments in this class are under preparation at J-PARC in Japan [11] and FNAL in the USA [12].

Figure 1.3 shows an overview of current, past and future experiments for cLFV searches involving muons. All these experiments aim to improve the corresponding branching ratio by some orders of magnitude. So far, no cLFV decay has ever been observed. Nevertheless the upper limits on the branching ratio of cLFV muon decays have been greatly improved over the last decades, as shown in Table 1.2. For each one of the cLFV channels involving muons, there is at least one experiment aiming to push the boundaries currently under construction or being upgraded, as indicated in Table 1.3.

Channel	Experiment	BR Upper Limit	Year	Facility	Reference
$\mu^+ \to e^+\gamma$	MEG	4.2 $\times 10^{-13}$	2016	PSI	[13]
$\mu^+ \to e^+e^-e^+$	SINDRUM	1.0 $\times 10^{-12}$	1988	PSI	[10]
$\mu^- N \to e^- N$	SINDRUM II	7.0 $\times 10^{-13}$	2006	PSI	[14]

Table 1.2: Current experimental limits (90 % confidence level) for cLFV muon decay channels.

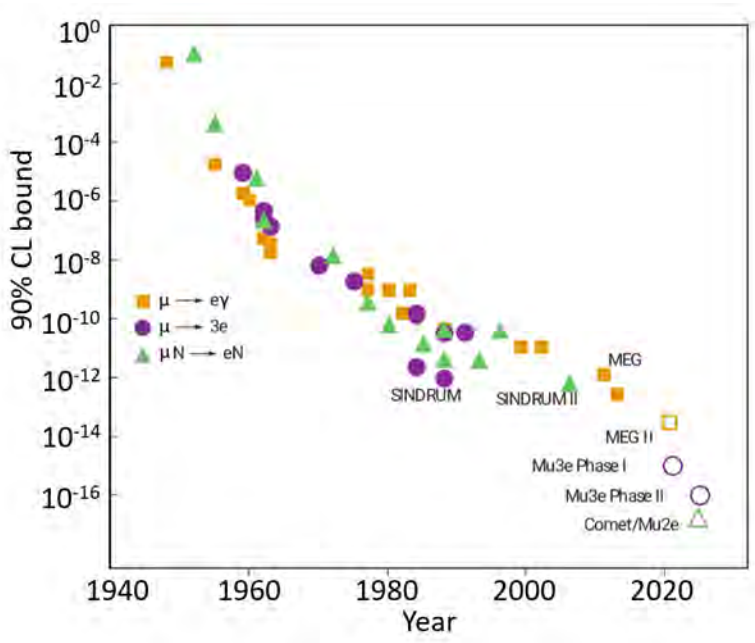

Figure 1.3: Past and future experiments searching for cLFV using muons. Hollow markers represent future experiments and solid markers represent currently running or already concluded experiments [15].

Process	Experiment	Sensitivity	Facility	Reference
$\mu^+ \to e^+\gamma$	MEG II	6.0 $\times 10^{-14}$	PSI	[16]
$\mu^+ \to e^+e^-e^+$	Mu3e Phase I	2.0 $\times 10^{-15}$	PSI	[17]
	Mu3e Phase II	1.0 $\times 10^{-16}$	PSI	[17]
$\mu^- Al \to e^- Al$	COMET	2.7 $\times 10^{-17}$	J-PARC	[18]
	Mu2e	2.9 $\times 10^{-17}$	FNAL	[19]

Table 1.3: Projected single event sensitivity of planned cLFV experiments with muons.

1.2.1 Neutrino Oscillations

The neutral leptons (i.e. neutrinos) can mix through the unitary Pontecorvo-Maki-Nakagawa-Sakata (PMNS) matrix [20]. The neutrino mass eigenstates (ν_1,ν_2,ν_3) rotate into flavour eigenstates (ν_e,ν_μ,ν_τ), under the matrix elements U_{li} [21], where $l = e, \mu, \nu$ and $i = 1, 2, 3$.

$$\begin{bmatrix} \nu_e \\ \nu_\mu \\ \nu_\tau \end{bmatrix} = \begin{bmatrix} U_{e1} & U_{e2} & U_{e3} \\ U_{\mu 1} & U_{\mu 2} & U_{\mu 3} \\ U_{\tau 1} & U_{\tau 2} & U_{\tau 3} \end{bmatrix} \begin{bmatrix} \nu_1 \\ \nu_2 \\ \nu_3 \end{bmatrix} \tag{1.6}$$

In the SM, cLFV processes are forbidden at tree level. Due to the fact that the PMNS matrix is not diagonal, neutrinos can oscillate and this in turn can induce cLFV through higher order loop diagrams. An example of this process is shown in Figure 1.4. However, the dominant neutrino mixing loop diagram is strongly suppressed. The Branching Ratio (BR) of this process [22] is extremely small (see Equation 1.7) primarily due to the large mass of the W boson [23] and the very small difference between the neutrino masses [24]. Any observation of cLFV would therefore directly signal physics beyond the SM.

$$BR_{SM}(\mu \to eee) \propto \left| \sum_{i=2,3} U^*_{\mu i} U_{ei} \frac{\Delta m^2_{i1}}{m^2_w} \right|^2 \lessapprox 10^{-50} \tag{1.7}$$

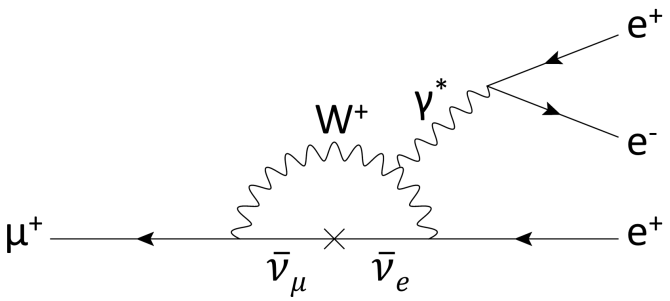

Figure 1.4: Feynman diagram of the $\mu^+ \to e^+e^-e^+$ process via neutrino mixing.

1.2.2 Beyond the Standard Model

There are many BSM theories that predict the BR in Equation 1.7 to be larger and thus possible to be observed experimentally. One of these theories is Supersymmetry (SUSY) [25]. In this theory the decay $\mu^+ \rightarrow e^+e^-e^+$ could be possible via a loop as seen in Figure 1.5. SUSY is an extension to the SM that predicts that each fundamental particle would have an associated supersymmetric particle of spin which differs by a half-integer. Mathematically SUSY is a spacetime symmetry between bosons and fermions. The extra particles predicted by SUSY could solve a number of problems that are present in the SM, with the most important being the hierarchy problem. The question is why the Higgs boson is so much lighter than the Planck mass, as one would expect that the large quantum contributions to the square of the Higgs boson mass would inevitably make the mass huge, unless there is an incredible fine-tuning cancellation between the quadratic radiative corrections and the bare mass. The extra particles predicted by SUSY would cancel out the contributions to the Higgs mass from their SM partners, making a Higgs boson with a mass of 125 GeV/c^2 possible. In the simplest SUSY theories, each pair of superpartners would share the same mass. The negative results from the LHC have already ruled out some of these simplest SUSY extensions to the SM. However, more complex SUSY theories have a spontaneously broken symmetry, allowing superpartners to differ in mass.

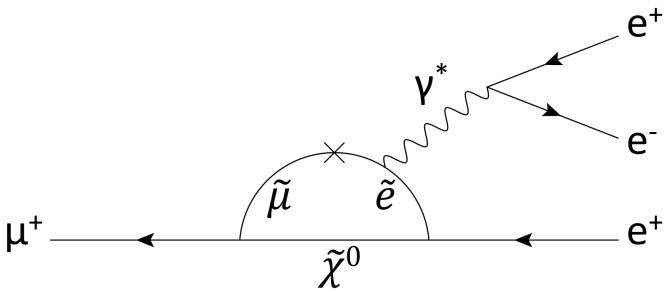

Figure 1.5: Feynman diagram of the $\mu^+ \rightarrow e^+e^-e^+$ involving SUSY particles.

2 | The Mu3e Experiment

The Mu3e experiment aims to search for the lepton flavour violating process of a positive muon decaying to two positrons and one electron. There are currently two planned phases for Mu3e. The goal is to reach a single event sensitivity of 2×10^{-15} and 1×10^{-16} in its Phase I and Phase II respectively. The expected sensitivity will improve on the latest measurements by four orders of magnitude, set in 1988 by SINDRUM. In order to achieve this goal, a continuous and intense beam is required. For Phase I, The πE5 beam line at the Paul Scherrer Insitute (PSI) in Switzerland is the perfect choice as it can provide $10^8 \mu^+/\text{s}$. For Phase II, a more intense beam will be required. This could be made possible by the construction of the high intensity muon beam (HiMB) that is currently under study at PSI [26].

2.1 Signal & Background

In Mu3e the muons stop on the surface of a thin target before decaying at rest. All electrons in the final state of the $\mu^+ \to e^+e^-e^+$ process can be detected. For discriminating signal and background events, energy and momentum conservation must be exploited. The signal decay is identified by two positrons and one electron originating from the same vertex. In addition to that, the following three conditions apply:

1. The vectorial sum of the electron momenta must be equal to 0.

$$\vec{p}_{tot} = \sum_{i=1}^{3} \vec{p}_i = 0 \tag{2.1}$$

2. The sum of the electron energies must be equal to the muon mass:

$$E_{tot} = \sum_{i=1}^{3} E_i = m_\mu \tag{2.2}$$

3. The particles must coincide in time.

An example event topology that fulfills the mentioned requirements is shown in Figure 2.1. There are however other events that can lead to a topology very similar to the signal. These processes can mimic the signal and thus it is crucial for Mu3e to achieve excellent vertex, momentum and timing resolution.

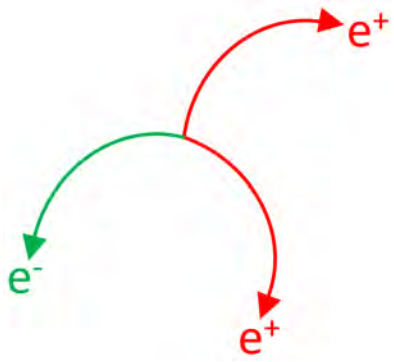

Figure 2.1: Event topology of the signal decay $\mu^+ \rightarrow e^+e^-e^+$.

One of the possible background processes is the radiative muon decay with internal conversion (IC) $\mu^+ \rightarrow e^+e^-e^+\overline{\nu}_\mu\nu_e$. This is shown in Figure 2.2a. It has two extra neutrinos that cannot be detected directly but we can confirm their presence as missing energy. This process occurs with a branching ratio of 3.4×10^{-5} [27]. The three electrons appear simultaneously in time and space. To distinguish this background from the signal, a very good momentum resolution (<1 MeV/c) is necessary. The two neutrinos carry away energy and momentum, thus Equation 2.1 and Equation 2.2 will not hold true. The second type of background is accidental and occurs when a combination of an electron and two positron tracks are generated by different sources. Examples of such event topologies are shown in Figure 2.2b. The main source of these positrons is the Michel decay which has a branching fraction close to 100%. The electrons can emerge from various sources such as Bhabha scattering or Compton scattering. In addition, photons created in the radiative muon decay $\mu^+ \rightarrow e^+\gamma\overline{\nu}_\mu\nu_e$ or via Bremsstrahlung can convert to e^+ e^- pair and thus provide the electron and one of the two positrons. There are other factors which can increase the accidental backgrounds such as inefficiencies in the reconstruction of tracks and fake tracks. In chapter 9, an analysis of a certain category of fake tracks is presented. In particular, these are fake tracks which are present due to misre-

contruction of the direction in which they are travelling. All accidental background processes have one thing in common: There is no common vertex for the three electrons. Figure 2.3 shows the contamination of the signal arising from IC decays as a function of the reconstructed mass resolution. In order to achieve a sensitivity of 2×10^{-15}, with a 2σ cut on the reconstructed muon mass, the average mass resolution has to be better than 0.8 MeV/c.

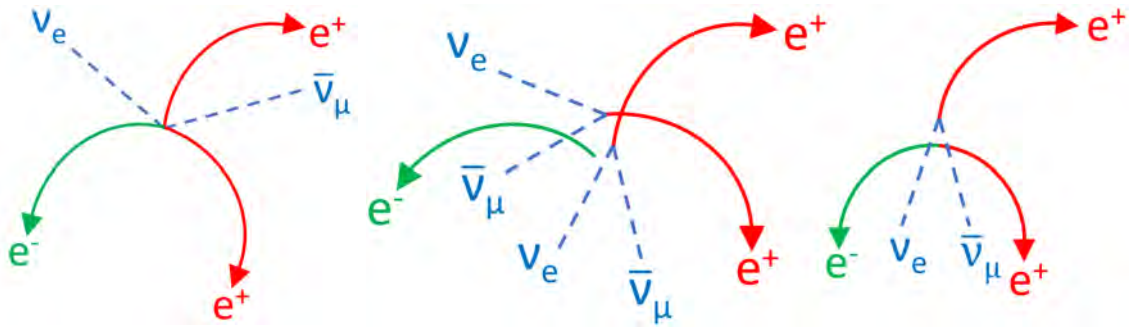

(a) Internal Conversion (b) Accidental backgrounds

Figure 2.2: Examples of background events that are expected for the Mu3e experiment.

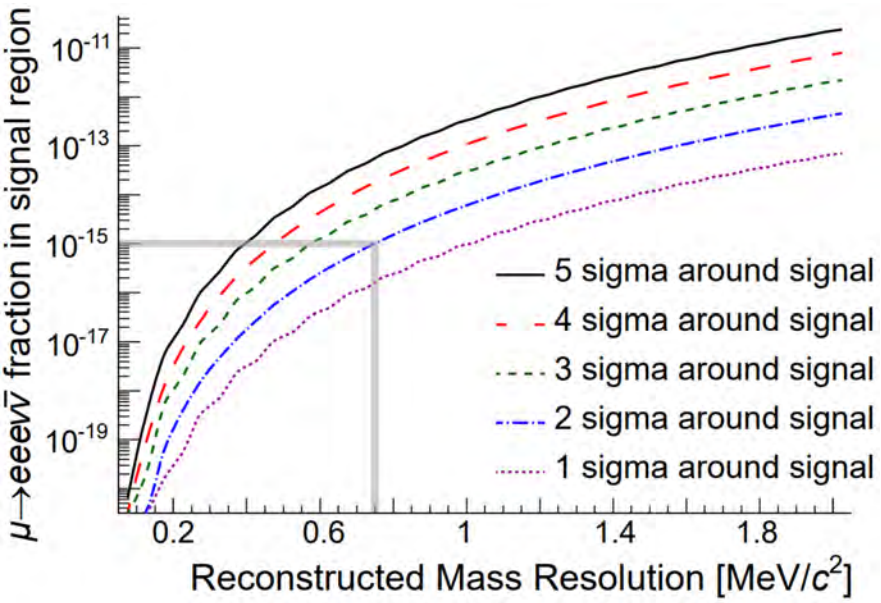

Figure 2.3: Suppression of the IC background as a function of the reconstructed mass resolution [28].

2.2 Detector Concept

The Mu3e detector is a high-resolution spectrometer for low energy electrons emitted when muons decay at rest on the surface of the target. The momenta of the electrons are measured using a silicon pixel tracker in a solenoidal magnetic field. At the energies of interest, multiple Coulomb scattering in the detector material is the dominating factor affecting the momentum resolution. Minimising the material in the detector is thus of the utmost importance. In principle, gaseous detectors such as wire chambers could be used to reduce the multiple Coulomb scattering. However such a detector would not be able to handle the extremely high rates needed to reach the sensitivity goal. For this reason, the tracker relies on High Voltage Monolithic Active Pixel Sensors (HV-MAPS) [29], thinned to 50 μm. The tracker consists of four radial layers of HV-MAPS sensors. The first pair of layers is placed around the target at radii of 2 cm and 3 cm respectively. This is crucial in order to maximise the resolution of the vertex reconstruction. The second pair of layers have an inner radius of 7 cm providing a second set of measurements for the trajectory of the particles. All particles follow a helical paths inside the magnetic field and create four hits, one on each layer. This is the minimum number of hits required to create a track (see chapter 8). Particles can however curl back towards the beam axis, creating longer tracks with more than four hits. For this reason, the outer tracker layers are further duplicated on both sides of the central region. Such longer tracks can also improve the momentum resolution significantly.

Mu3e will use two timing detectors which guarantee good combinatorial background suppression and high rate capabilities. In the central region scintillating fibres will be used, placed just before the third layer of the tracker. This still needs to be as thin as possible since the particle has not travelled through all four layers yet. At each end, silicon photomultipliers (SiPMs) will be placed for photon detection. A recurling track consists of a minimum of six hits so it is possible to use a thicker timing detector in the recurl stations which results in a larger energy deposit for passing particles. This means a high light yield which can give more precise timing information. Therefore, a detector made of scintillating tiles will be implemented on the inside of the recurl stations. It will be composed of individual tiles which will

be read out individually by SiPMs. Figure 2.4 and Figure 2.5 show the total Mu3e detector for phase I of the experiment. For Phase II it was initially planned to have two more recurl stations, one on each side, but longer recurl stations could be used instead.

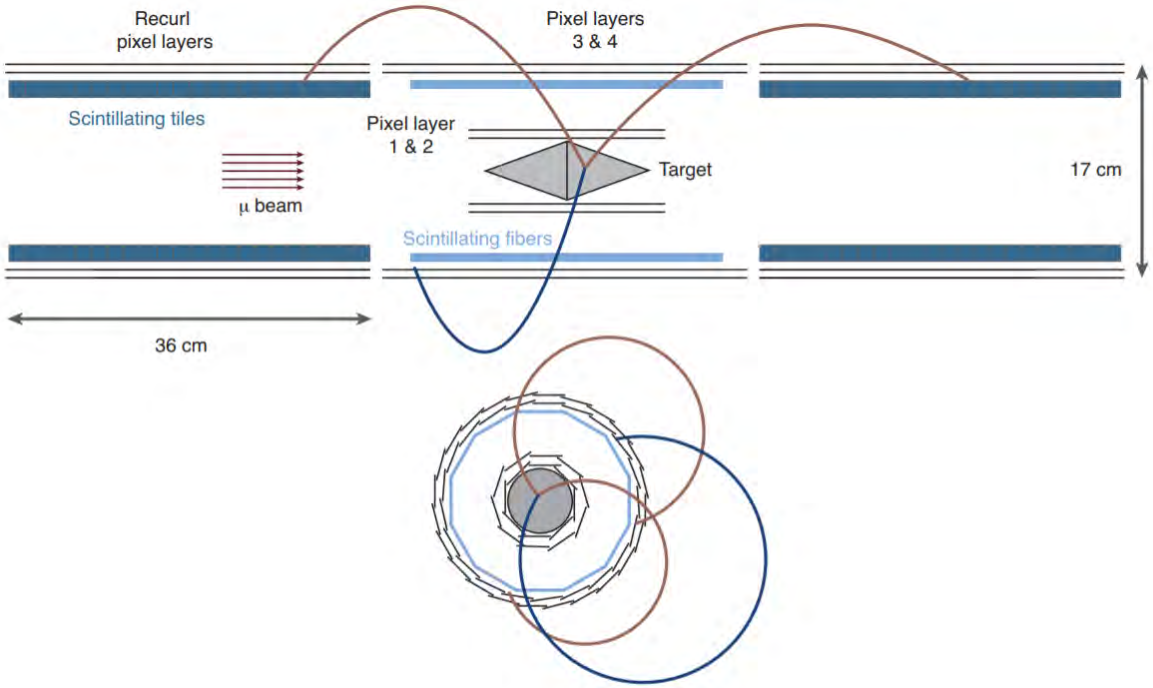

Figure 2.4: Schematic view of the experiment in the phase IB configuration [28]. Phase IA will not have any recurl stations.

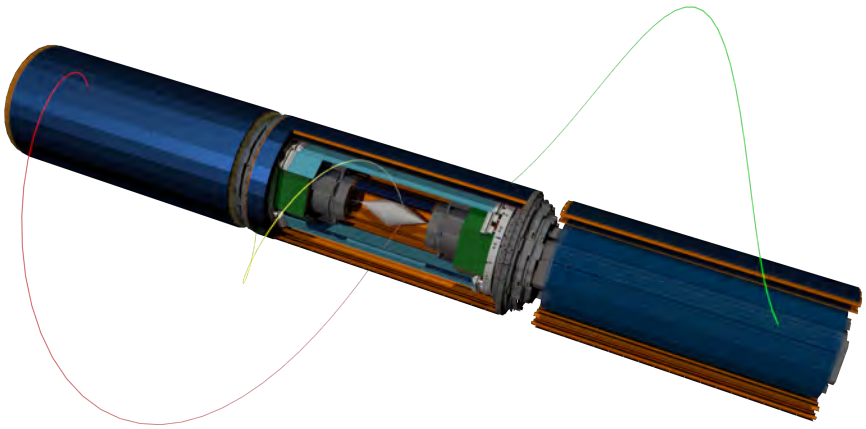

Figure 2.5: Partial CAD model of the Mu3e detector. Some modules have been removed for better visibility [28].

Mu3e is optimized for precise momentum resolution at high particle rate. In order to achieve good momentum and vertexing resolution, there are two important factors that need to be taken into consideration: the positional resolution of the pixel sensor and the multiple Coulomb scattering in the detector material. The resolution of a pixel sensor, σ_x, is derived from the variance of a uniform distribution over the pixel:

$$\sigma_x^2 = \int_{\alpha/2}^{-\alpha/2} x^2 f(x)\, dx = \frac{\alpha^2}{12} \tag{2.3}$$

$$\sigma_x = \frac{\alpha}{2\sqrt{3}} \tag{2.4}$$

where α is the pixel pitch and the uniform distribution function $f(x)$ = 1/α (for 0 $\leq$ x $\leq$ α). It this therefore clear that the resolution depends directly on the size of the pixel sensor. Multiple Coulomb scattering, shown in Figure 2.6, can be approximated by a Gaussian function with a width θ_{MS} which depends on the deflected particle momentum:

$$\theta_{MS} = \frac{13.6\, MeV}{\beta cp} z \sqrt{\frac{x}{X_0}} \left[1 + 0.0038 \ln \left(\frac{x z^2}{X_0 \beta^2} \right) \right] \tag{2.5}$$

where the momentum, velocity and charge number of the incident particle are denoted as p, β and z respectively. x/X_0 is the thickness of the scattering medium in units of radiation length. It is therefore crucial to hold the material budget to a minimum by making the sensors as thin as possible. Additionally, this has the effect that offsets, labelled y in Figure 2.6, become negligibly small and can be neglected.

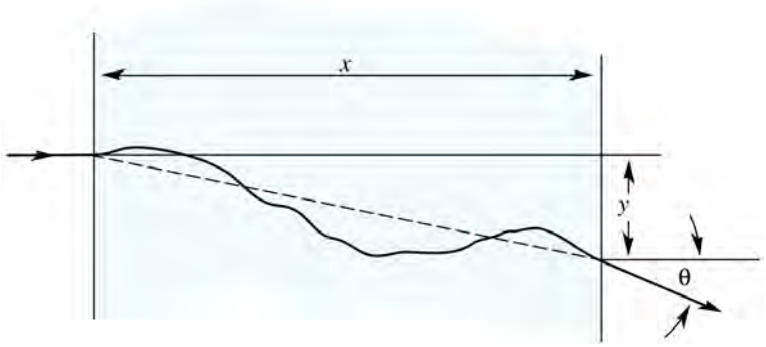

Figure 2.6: Multiple scattering of a particle traversing a material. The scattering angle with respect to the incoming trajectory is denoted by θ [4].

In the Mu3e experiment, muons are stopped and decay at rest, meaning their decay products cannot exceed an energy that corresponds to half the muon mass, i.e. approximately 53 MeV/c. In order to be able to measure the momentum of a particle in the first place, a magnetic field is needed. In a magnetic field the Lorentz force bends the trajectories of charged particles such that they describe a helical motion. By measuring the radius of the helix, one can also calculate the momentum of the corresponding particle via:

$$p_T = 0.3B\rho \tag{2.6}$$

where p_T is the transverse momentum of the particle in units of GeV/c, B is the magnetic flux density in T and ρ is the radius of the helix in meters projected onto a surface perpendicular to the magnetic field. In other words the task is to reconstruct helical tracks, calculate their radius and then calculate the momentum of the particle. From Figure 2.7 it can be seen that the effect multiple scattering has on momentum resolution cancels to first order if a particle is measured again after one or more half turns. Since this is very much desirable, the geometry of the Mu3e tracking detector is chosen such that particles that re-enter the tracking detector, predominantly do so when their bending angle is a multiple of π.

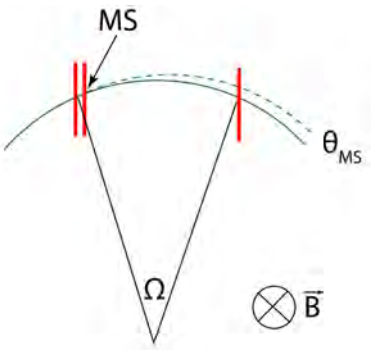

(a) Multiple scattering for measurement planes with a distance $\ll \pi$.

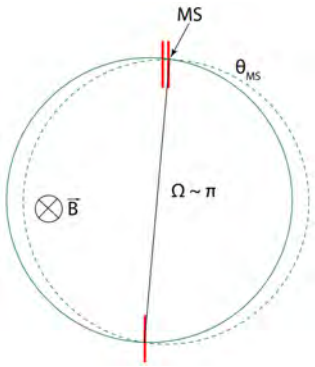

(b) Multiple scattering for measurement planes with a distance of π.

Figure 2.7: Effect of multiple scattering on trajectory offsets after different path lengths. For path lengths multiples of π, the offset due to multiple Coulomb scattering is minimised [17].

2.2.1 Magnet

The Mu3e magnet provides a homogeneous 1 T magnetic field. The field strength is chosen such that all electrons with a transverse momentum greater than 10 MeV$/$c can reach the fourth pixel layer and recurl back. Using a weaker magnetic field some of the decay particles that would otherwise recurl back would be lost and a stronger field would make some of particles recurl back before reaching the fourth pixel layer. Field inhomogeneities ($\Delta B/B$) along the beamline are required to stay below 10^{-3} within $\pm$60 cm around the center. The magnet also serves as a beam optical element for guiding the muon beam to the target. To further improve the field homogeneity, and for matching the magnetic field of the last beam elements of the beamline, a compensation coil and two shim coils are included on either side of the magnet. The system is capable of generating a field up to 2.6 T. An iron shield is included to reduce stray fields to less than 5 mT at a distance of 1 m. This leads to an overall weight of around 30 tonnes. Part II of the thesis gives a detailed description of the magnet system and how it performs in the real world.

2.2.2 Stopping Target

The main challenge for the design of the stopping target is to optimise the stopping power, while also minimising the total amount of material. This is needed to reduce both backgrounds and the impact on the track measurement. Therefore it should contain just enough material in the beam direction to stop most of the muons, but should be as thin as possible to minimise the material in the flight direction of decay electrons. The target is a double-cone made of 70 μm of Mylar in the front part and 80 μm Mylar in the back part, with a total length of 100 mm and a radius of 19 mm. A variety of target shapes were considered and it was concluded that for the given beam parameters and geometrical constraints, the double cone offers the highest stopping fraction with the least material. The simulated stopping distribution along the beam axis for the double cone target is shown in Figure 2.8. A larger amount of muons are stopped at the front part of the target while a smaller amount pass through the first cone and are stopped on the rear part of the target. Furthermore, the decay vertices should be spread out as wide as possible in order

to reduce accidental coincidences of track vertices and to produce a more or less even occupancy in the innermost detector layer. A sketch of the target dimensions and a prototype can be seen in Figure 2.9a and Figure 2.9b respectively.

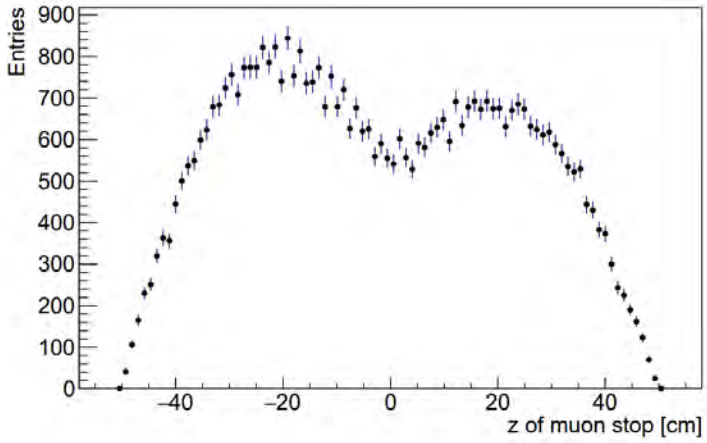

Figure 2.8: Simulated stopping distribution for the double cone target [28].

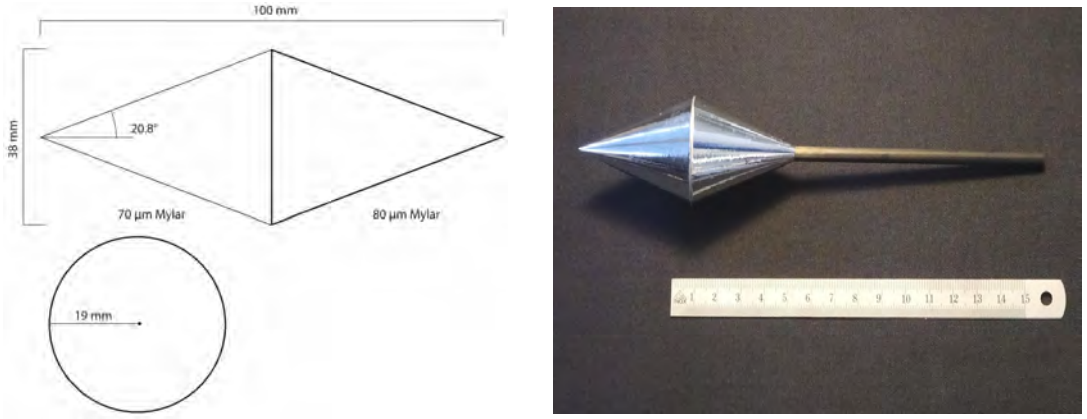

(a) A schematic.

(b) A full model.

Figure 2.9: The Mu3e stopping target [28].

2.2.3 Beamline

Mu3e will be installed in the πE5 channel at PSI which delivers the highest intensity continuous muon beam available in the world. A 1.3 MW cyclotron accelerates protons to 590 MeV kinetic energy at a current of up to 2.4 mA [30]. The protons then hit a primary target (TgE) made of polycrystalline graphite and produce pions. Some of them decay close to the surface of the target producing the so called sur-

face muons whose momentum distribution peaks at approximately 28 MeV/c. A Wien filter separator then separates the positrons from the muons such that an almost pure muon beam can be obtained. The low pion contamination, in addition to the small branching fractions, lead to negligible rates for this background. A CAD model of the πE5 channel can be seen in Figure 2.10. Measuring at least 10^{16} muons with 10^8 μ^+/s would mean a net data taking time of more than three years. Since Mu3e and the MEG II experiment will share the same channel, an additional compact muon beam line (CMBL) [31] section is constructed to divert muons towards the Mu3e detector. After the planned HiMB upgrade, the muon delivery rate will increase to about $10^{10}\mu^+$/s. This is crucial to reach the ultimate sensitivity goal of Mu3e of 1×10^{-16} in a reasonable time frame. Part III of the thesis gives a detailed description of the beamline along with a G4Beamline simulation analysis and the first ever beam measurements at the centre of the Mu3e magnet with the full beamline installed.

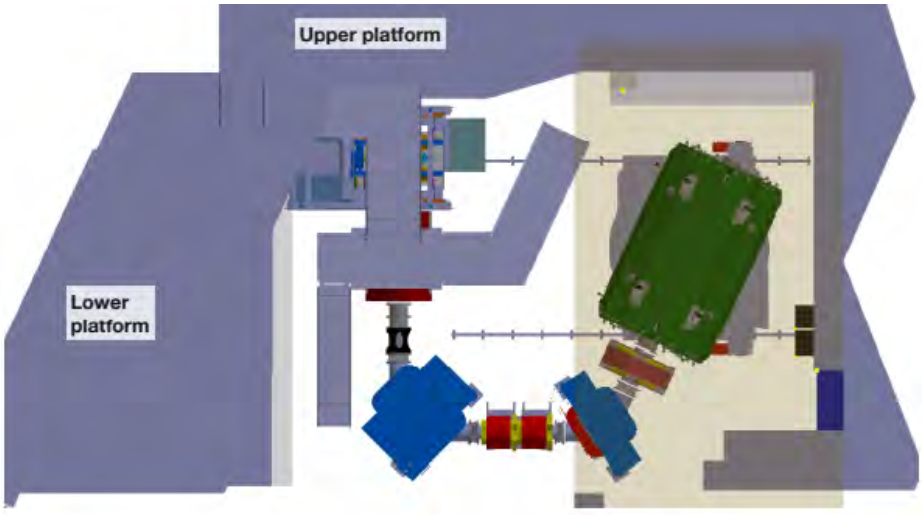

Figure 2.10: CAD model of the πE5 channel and compact muon beam line [28]. The Mu3e magnet is shown in green.

2.2.4 Pixel Tracker

The Mu3e pixel tracker provides precision hit information for the track reconstruction of the electrons and positrons produced in muon decays. Achieving the best possible vertex and momentum resolution measurements for these decay particles is of key importance to the success of the experiment. The geometry of the tracker

layers determines the acceptance and momentum resolution for outgoing tracks. The Mu3e Phase I pixel tracker consists of three parts, the central pixel tracker and two recurl stations, as shown in Figure 2.11. The central pixel tracker has four layers of pixel sensors: two inner layers at small radii and two outer layers at larger radii, as shown in Figure 2.12.

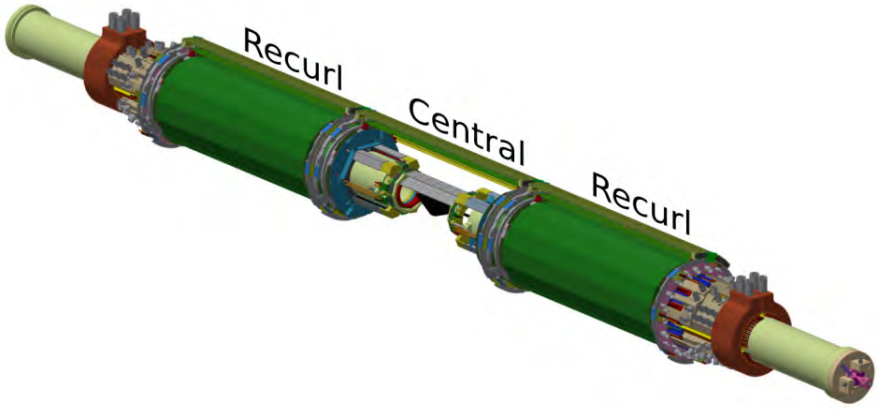

Figure 2.11: CAD model of the pixel tracker for phase I of the experiment. Some modules have been removed for better visibility [28].

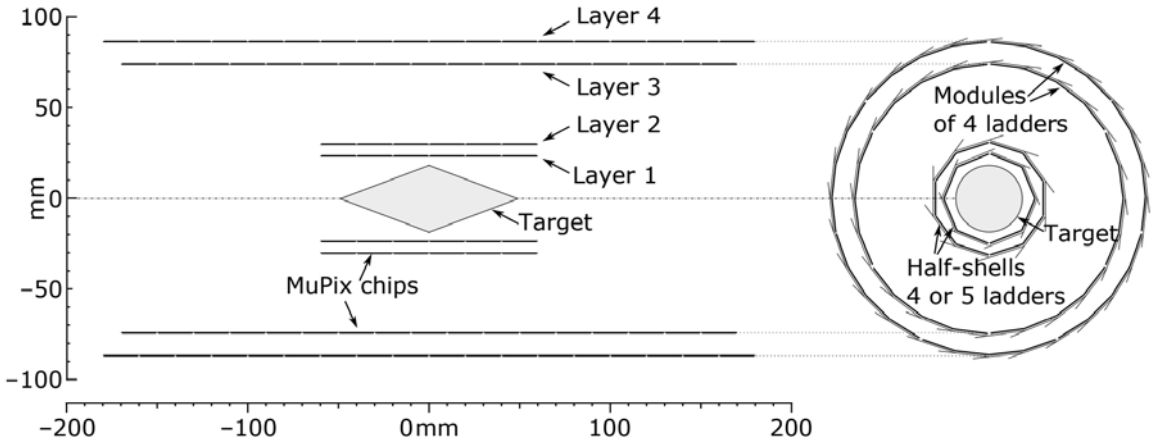

Figure 2.12: Geometry of the central Mu3e pixel tracker [28].

The inner and the first set of double layers is located as close as possible to the target in order to provide the highest possible vertex resolution. The second set of double layers are located at larger radii to provide an improved measurement of the bending radius of a particle. This leads to a better momentum resolution. Due to the fact that electrons have a low momentum and their trajectory is dominated by multiple scattering, a pair or layers with a small gap in between is favoured. Using recurl

stations on both sides it is possible to get another set of measurements for particles that curl back towards the beam axis. The tracker must have a very low material budget and must be capable of achieving a very precise position measurement. The HV-MAPS sensors are capable of achieveing this. Dedicated chips called MuPix are developed specifically for the Mu3e experiment [29]. A single pixel covers an active area of $80 \times 80 \mu m^2$, while one sensor consists of 250×250 pixels incorporated on a surface of $20 \times 20 mm^2$. Multiple MUPIX chips can be glued together to make up ladders that represent the smallest mechanical unit. The ladders of the inner layers carry six sensors each and the outer layers carry 18 sensors each. The ladders have an overlap of 0.5 mm which improves the detector acceptance. The pixel modules consist of several ladders held by an endpiece. Multiple modules are mounted with their endpieces onto an endring to build up cylindrical detector layers. This is shown in Figure 2.13. The geometrical design parameters of the pixel central barrel are listed in Table 2.1.

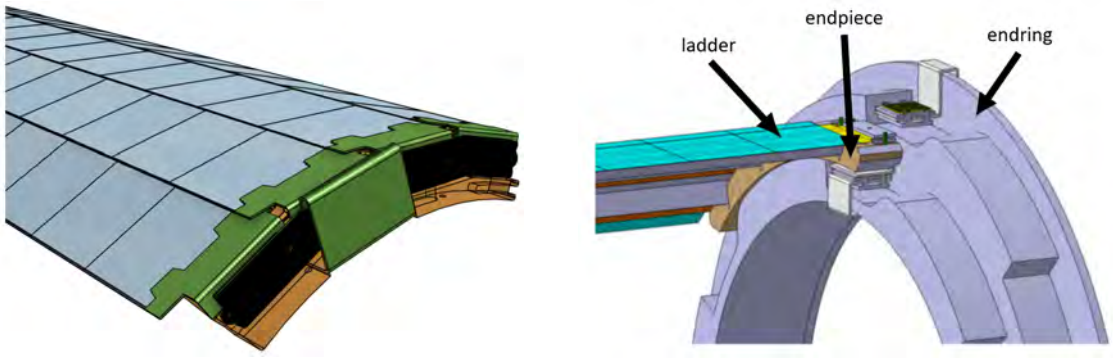

(a) Four ladders.

(b) Ladders mounted onto an endring.

Figure 2.13: CAD models of a pixel module [28].

As of 2020 nine MuPix prototypes have been studied. Single hit efficiencies of MuPix sensors were determined in test beam campaigns at CERN, DESY, MAMI and PSI. Studies were performed as a function of various DAC and HV settings for different comparator thresholds and powering schemes. Beam telescopes were used for the reconstruction of reference tracks and the measurement of single hit efficiencies. The single hit efficiency of the MuPix8 sensor is shown in Figure 2.14 as a function of the threshold. The Mu3e efficiency and noise requirements are fulfilled in a large threshold range of about 40-90 mV.

Pixel Layer	1	2	3	4
Number of modules	2	2	6	7
Number of ladders	8	10	24	28
Number of MuPix sensors per ladder	6	6	18	18
Length [mm]	124.7	124.7	351.9	372.6
Radius [mm]	23.3	29.8	73.9	86.3

Table 2.1: Pixel tracker geometry parameters of the central barrel.

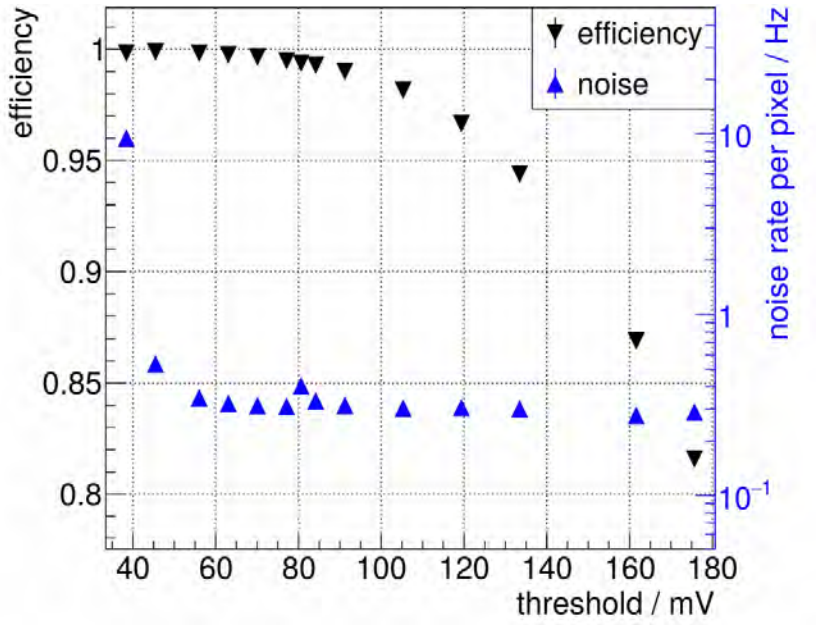

Figure 2.14: Hit efficiency and noise as a function of the charge threshold for the MuPix8 sensor as measured for 4 GeV/c electrons [28].

2.2.5 Timing Detectors

A timing system consisting of scintillating fibres and scintillating tiles is used to suppress the accidental backgrounds and to give timestamps to each track. Since the amount of material in the central region is critical for achieving the projected momentum resolution, a very thin scintillating fibre detector is chosen. At the recurl stations the momentum measurements are completed and therefore a thicker scintillating tile detector can be installed under the pixel tracker to provide superior time information. The Mu3e scintillating fibre (SciFi) detector has a time resolution of 400 ps and a 90% overall efficiency [32]. It consists of fibre ribbons arranged in a

cylindrical shape. Each ribbon consists of three layers of scintillating fibres that are staggered in order to assure continuous coverage and high detection efficiency. The length of each ribbon is 30 cm and it is constructed using 250 μm thick fibres with circular cross-section. Both ribbon ends are equipped with SiPM arrays for photon detection. The tile detector aims at providing the most precise timing information of the particle tracks possible. It is located at the very end of recurling particle trajectories, therefore there are no constraints on the amount of detector material. The detector consists of plastic scintillator segmented into small tiles. Each tile is read out with a SiPM directly attached to the scintillator. The main goal of the tile detector is to achieve a time resolution of better than 100 ps and a detection efficiency close to 100% in order to efficiently identify coincident signals of electron triplets and suppress accidental background. The size of one tile is $6.3 \times 6.2 \times 5.0mm$. Figure 2.15a and Figure 2.15b show the geometry of the submodules of the fibre and the tile detector respectively. Based on prototype tests, resolutions of better than 50 ps and detection efficiencies close to 100% are expected for the tile detector [33].

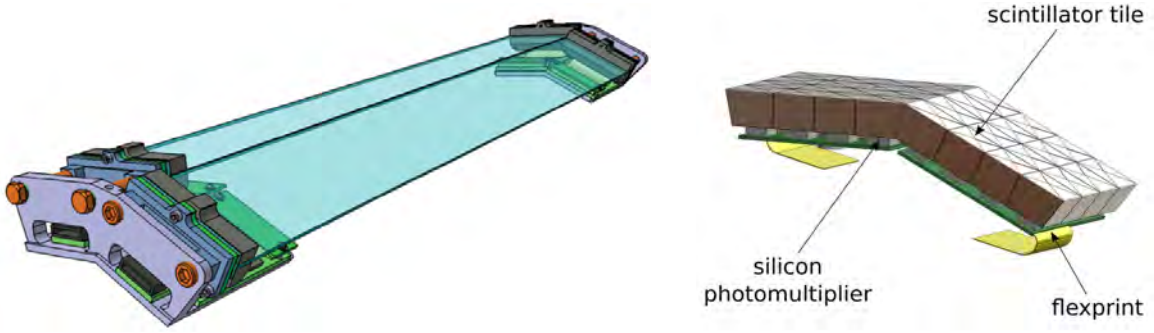

(a) Submodule of fibre detector.

(b) Submodule of tile detector.

Figure 2.15: CAD models of fibres and tiles submodules [28].

2.2.6 Cooling

The detectors, their electronics, the power converters and the data acquisition systems are located inside the densely spaced Mu3e magnet. The heat they produce is transferred to the outside by forced convection cooling. Except for the pixel sensor chips, water cooling is used everywhere else. For the pixels, a novel gaseous helium cooling has been developed. Water cooling is used to cool all the front-end

electronics which are located outside the active volume of the detector. The anticipated heat load per source totals to about 5 kW [28]. To protect the detector from ice buildup, the water inlet temperature is required to be above 2°C. All MuPix chips of the pixel tracker are cooled by gaseous helium of $T_{He} \leq 0$°C at approximately ambient pressure. Assuming a maximum power consumption of the pixel sensors of 400 mW/cm^2 the helium gas system is designed for a total heat transfer of 5.2 kW, which increases the averaged gas temperature by about 18 °C. For this, the helium cooling system has to provide a flow of about 20 m^3/min under controlled conditions split between several cooling circuits.

2.3 Data Acquisition

The Mu3e experiment uses a state-of-the-art data acquisition (DAQ) to handle information coming from all sub-detectors in a triggerless mode of operation. The DAQ system is organized in three logical and physical layers. This is shown in Figure 2.16. The first layer consists of front-end field programmable gate arrays (FPGA) processing raw data from all sub-detectors. Each detector transfers hit information to its corresponding FPGA over 1.25 Gbps low voltage differential signaling (LVDS) links. For the Phase I of the experiment, the expected data rate in this layer is 80 Gbit/s [34]. The FPGAs are programmed to sort and group the hit information in frames of 50 ns. The packets from the front-end FPGAs are delivered to a set of switching boards over optical links with 6 Gbps bandwidth per link. These are dedicated boards that combine the information from all modules of a given sub-detector system and distribute it to FPGAs in an event filter farm. Each PC in the filter farm has access to data from all the detectors during a specific time slice. The data transfer between the switching boards and the filter farm is realized over 10 Gbits optical links. The first component in the event filter farms are the FPGAs that execute event building, buffering and preliminary sorting and clustering operations. They communicate with the filter farm PCs over PCIe lines. The event data from the FPGAs is copied to the memory of high-performance graphics processing units (GPUs). A dedicated tracking and vertex reconstruction algorithm processes the incoming data online. It selects only event topologies close to the Mu3e signals reducing the output by a factor of 100 [34]. The selection requires three tracks coincident in time, consis-

tent with originating at a common vertex and with the expected kinematic properties of signal events. The results are then delivered to a central DAQ computer running the Maximum Integrated Data Acquisition System (MIDAS) software [35]. From there the data is stored to discs for further analysis.

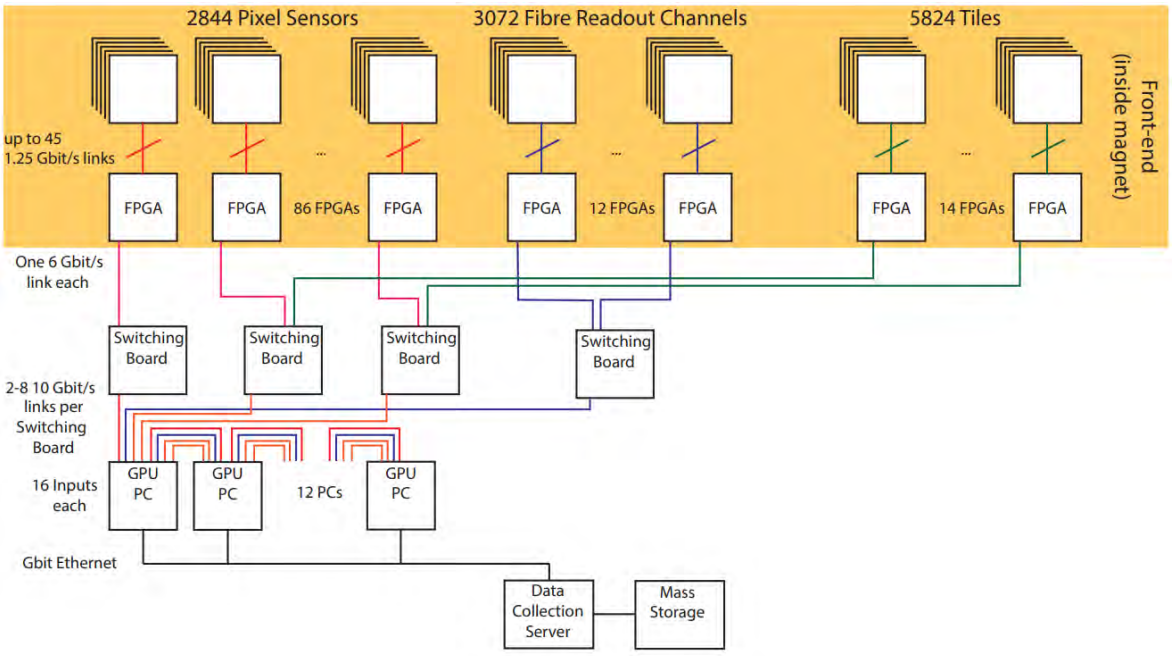

Figure 2.16: Overall Mu3e readout scheme [28].

2.4 The Mu3e Software

A dedicated simulation software based on the GEANT4 toolkit [36] is developed within the Mu3e collaboration. Physics processes, environmental conditions, detector responses and digitization are all taken into account. After the initial particle propagation through the experimental volume, information about the hits in each detector is stored. Tracks are first reconstructed with data from the pixel sensors. Afterwards they are propagated to the fibre or tile detector planes and assigned timestamps based on their proximity to the hits in the corresponding time system. Depending on the number of pixel layers the tracks originate from they are classified into 4, 6, and 8-hit tracks. Part IV of the thesis gives a detailed description of the software package and an analysis of fake tracks in Mu3e.

Part II

Mu3e Magnet System

3 | Magnet Operation

This chapter contains all the tests and measurements that were carried out during the commissioning of the Mu3e magnet system. The magnet is a cryogen-free system (no liquid nitrogen or helium), containing a superconducting solenoid. It was constructed by the company Cryogenic Ltd in the United Kingdom. It comprises of four main components: A cryostat vessel with a room temperature bore tube, a radiation shield linked to the first stage of the cryocoolers, a magnet assembly linked to the second stage of the cryocoolers and a passive high permeability shield to limit the magnetic stray flux. The system sits on a 360° rotating platform which can be used to place the system at the required position. The passive shield is constructed using two dodecagon endplates separated by twelve flux return bars running between the endplates. The cryostat has an aluminium alloy outer body with a stainless steel room temperature bore. There are ports for the cryocoolers, magnet current leads, magnet protection leads, instrumentation, evacuation and overpressure. Access to the room temperature bore is available via the semicircular steel doors. The bore tube assembly is sealed to the cryostat vessel using nitrile O-ring seals.

The magnet and the radiation shield are suspended from the cryostat outer vessel using both axial and radial tie rods. The radial tie rods are glass fibre and the axial tie rods are stainless steel. Each tie rod is thermally grounded to the first stage of the cryocoolers to limit the thermal load to the magnet.

The radiation shield is constructed from a series of high purity aluminium alloy plates and tubes. Its function is to intercept radiant heat from the room temperature surfaces of the outer vacuum vessel and divert it to the first stage of the cryocoolers. It is used as a thermal grounding point for the support structure between the room temperature vessel and the magnet and it is surrounded by optimised multilayer

superinsulation to minimise the thermal load to the first stage of the cryocoolers. It is coupled to all four cryocoolers using flexible thermal links that allow the shield to contract both radially and axially without imposing strain on the cryocooler body.

The system uses four two-stage Gifford-McMahon (GM) cryocoolers (A,B,C,D) to produce temperatures of around 4 K at the coils (see Figure 3.4). Four compressor units supply the cryocoolers with high-pressure Helium gas. The radiation shield is attached to the first stages of the cryocoolers and in operation cools to approximately 40 K. The second stage is attached directly to the magnet and has a base temperature of <4.2K. Temperature sensors are located throughout the system to monitor various internal components during the cooldown and subsequent operation of the system. A nitrogen cooling circuit can be used to speed up cooling of the magnet from room temperature to approximately 80 K. The cooling circuit consists of a copper tube thermally anchored to the individual second stages of the cryocooler and also various points on the surface of the magnet.

The magnet is supported with the cryostat outer vacuum chamber (OVC) using radial and axial tie rods. The OVC is supported within the passive shield using eight radial adjustable pads and four axial adjustable pads. Under normal operating conditions, provided the magnet is properly centred, the array of support pads will be adjusted to rest against the OVC effectively fixing the OVC position within the passive shield. However, for initial setup, the OVC is allowed to move axially so that the magnet can be balanced within the shield and hence minimise any interactive force between the magnet and shield. The radial position of the OVC is set by mechanical measurement and during energisation, any small radial forces that may arise will by default tend to centre the magnet within the shield. Monitoring of the axial position of the magnet within the shield during energisation is possible using four load cells in total, two on each side of the system. The cells produce an output voltage as a result of relative movement of the cryostat and passive shield. If the magnet is positioned correctly within the passive shield it will not generate significant forces on the shield during energisation. The field is generated using four separately energisable circuits. The main coil is used to generate the required field at the centre, whereas the compensation and the two shim coils can be used to further improve the field homogeneity or to generate subtle changes in the field profile.

All coil windings are wound using insulated niobium-titanium superconductor. The winding data is given in Table 3.1 and the physical properties of the system are given in Table 3.2. Pictures of various parts of the system are shown in Figure 3.1. An electronics rack houses a dedicated computer, temperature monitors and the power supplies for the coils, as shown in Figure 3.2. A CAD model of the magnet is shown in Figure 3.3. It must be noted that ramping up either shim winding will generate an imbalance of the magnet within the passive shield.

(a) Solenoid

(b) Bore tube

(c) Cryocooler

(d) Load cell

(e) Rotating platform

(f) Compressor unit

Figure 3.1: Pictures of the Mu3e magnet system.

Figure 3.2: Electronics rack of the Mu3e magnet. From top to bottom: Dedicated computer, temperature monitor, power supplies for shim 2, shim 1, compensation and main coil.

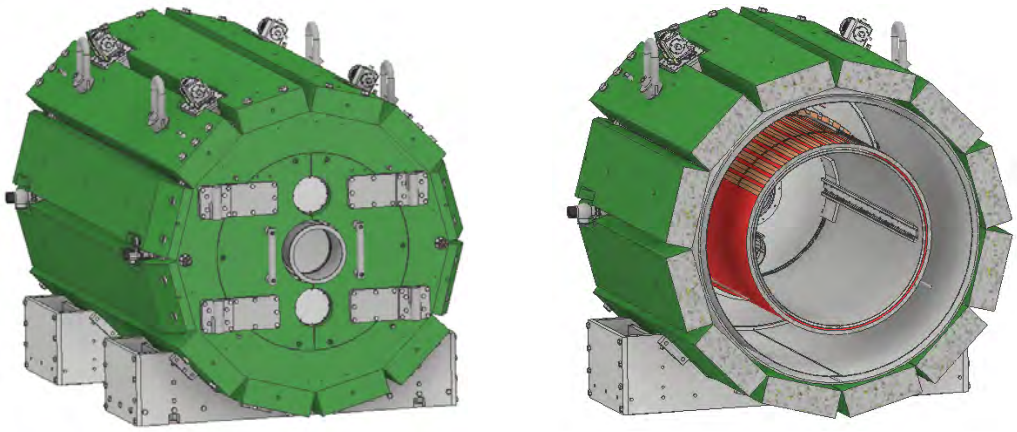

(a) Whole system

(b) Section of the system

Figure 3.3: 3D CAD models of the Mu3e magnet. The iron shield is shown in green and the coils in red [28].

Coil Winding Data							
Coil	Inner Radius [cm]	Outer Radius [cm]	Left Edge [cm]	Right Edge [cm]	Turns [n]	Current for 1T [A]	Current for 2.6 T [A]
Main	53.115	53.865	-127	127	5408	98.9	259.0
Main	53.865	54.2	-127	127	2694	98.9	259.0
Main	54.2	54.68	-127	127	4484	98.9	259.0
Main	54.68	55.225	-127	127	6832	98.9	259.0
Main	55.225	55.39	-127	-97.2	200	98.9	259.0
Main	55.225	55.39	-97.2	97.2	1150	98.9	259.0
Main	55.225	55.39	97.2	127	200	98.9	259.0
Comp	55.392	56.792	-127	-103.2	1750	72.0	187.2
Comp	55.392	56.792	103.2	127	1750	72.0	187.2
Shim1	56.792	57.072	-127	-102.9	345	N/A	N/A
Shim2	56.792	57.072	102.9	127	345	N/A	N/A

Table 3.1: Coil winding data of the Mu3e magnet [37].

Property	Value	Unit
Overall mass	28.5	Tonnes
Overall height	2.18	m
Overall width	2.21	m
Overall length	3.2	m
Bore tube diameter	1.0	m
Bore tube length	2.74	m
Magnet cold mass	1550	kg
Passive shield thickness	16	cm

Table 3.2: Physical properties of the Mu3e magnet [37].

3.1 Gifford-McMahon Cryocooler

GM cryocoolers have found widespread application in many systems where a super low temperature is required. It consists of four main components: A cold

head, a compressor unit, flex lines and a cold head power cable. The working fluid is Helium at pressures in the range 10–30 bar. The compressor unit, which uses water for cooling, supplies the cold head with power and high-pressure Helium gas. Figure 3.4 shows the complete GM cryocooler system. For the Mu3e experiment, the SRDK series cryocooler (F-50 series compressor unit) from Sumitomo Heavy Industries is used. The cold head contains a compression and expansion space, a

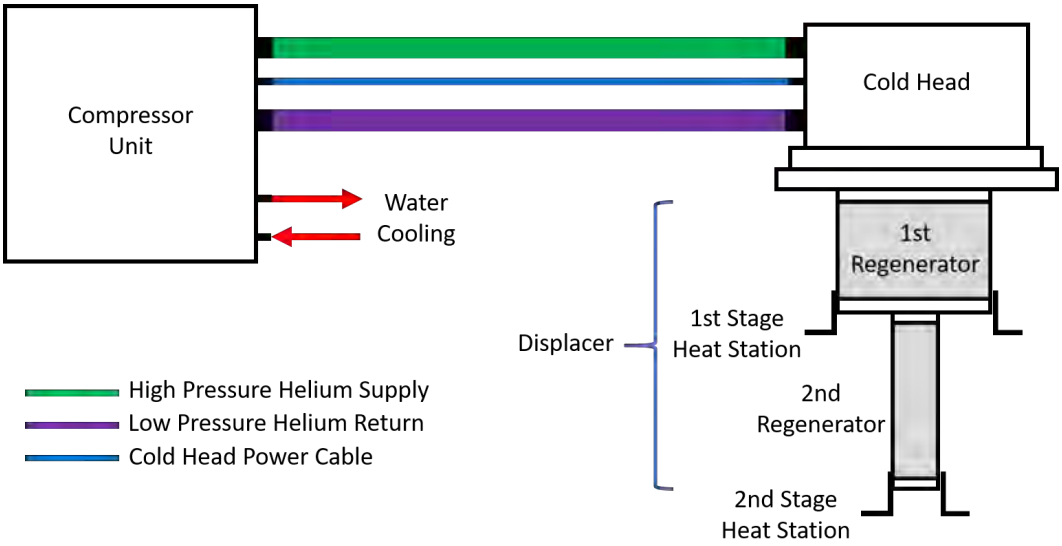

Figure 3.4: The entire system for a two-stage GM cryocooler. Diagram not to scale.

regenerator, and a displacer. In a single-stage GM cryocooler the displacer and the regenerator is a single body. A regenerator consists of a matrix of a solid porous material, such as granular particles or metal sieves, through which gas flows back and forth. Single-stage GM cryocoolers can achieve a base temperature of around 60-80K. For lower temperatures, two-stage GM cryocoolers must be used, which are capable of reaching temperatures of around 2-4K. The pressure variations in the cold head are obtained by connecting it periodically to the high and low pressure sides of a compressor by a rotating valve. Its position is synchronized with the motion of the displacer. The two volumes, one above and the other below the diplacer, can be varied from zero to a maximum value but the total volume remains constant. The complete GM cycle for a simple one-stage GM cryocooler is illustrated in Figure 3.5. The cycle starts with the low-pressure valve closed, the high-pressure valve open, and the displacer all the way to the right, inside the cold region and all the gas at room temperature, From a to b, the displacer moves to the left while the cold

head is connected to the high-pressure side of the compressor. The gas passes the regenerator entering the regenerator at ambient temperature, T_a and leaving it with temperature T_f. Heat is released by the gas to the regenerator material. From b to c, the high-pressure valve is closed and the low-pressure valve opened with fixed position of the displacer. At this stage part of the gas flows through the regenerator to the low-pressure side of the compressor. The gas expands in an isothermal process so heat is taken up from the application. This is where the useful cooling power is produced. From c to d, The displacer moves to the right with the cold head connected to the low-pressure side of the compressor forcing the cold gas to pass the regenerator, while taking up heat from the regenerator. From d to a, the low-pressure valve is closed and the high-pressure valve opened with fixed position of the displacer. The gas now is in the hot end of the cold head and it is compressed. During this process heat is released to the surroundings. In the end of this step we are back in position a. GM cryocoolers have many advantages over other types of cryocoolers. In particular they have been proven to serve as reliable cooling devices, they implement known and tested technology and they produce very low vibrations. The last one is of particular importance for the Mu3e experiment as even relatively low vibrations can cause a misalignment of the detector parts and electronics located inside the solenoid.

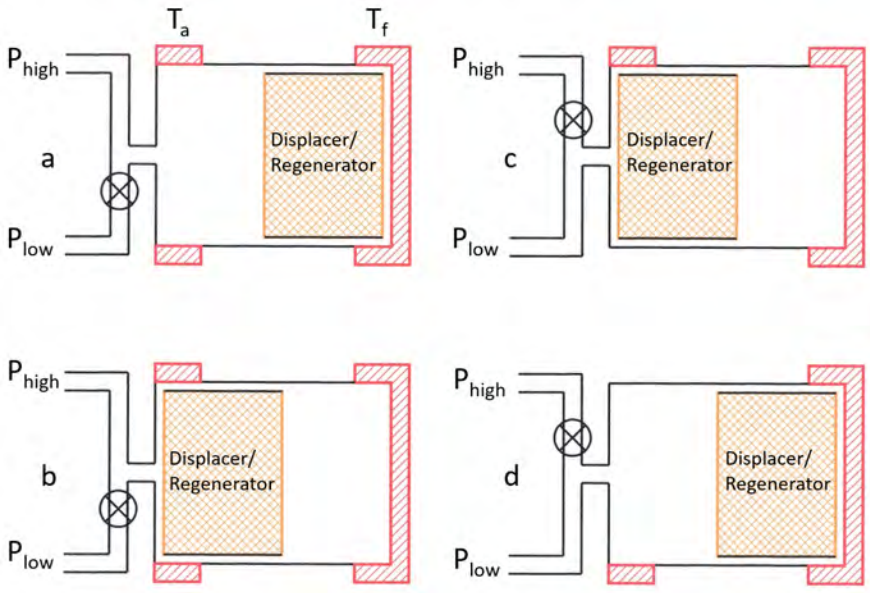

Figure 3.5: The four stages in the cooling cycle of a single-stage cryocooler.

3.2 System Requirements

The magnet has to provide a homogeneous solenoidal magnetic field of 1 T and field inhomogeneities ($\Delta B/B$) along the beam line must stay below 10^{-3} within $\pm$60 cm from the mid-plane of the whole system, which is essentially the length of the detector during Phase I of the experiment. The basic requirements of the superconducting magnet are given in Table 3.3. The long term stability of the magnetic field should be $\Delta B/B \leq 10^{-4}$ over each 100 days data-taking period. Field inhomogeneities will increase the uncertainty on the momentum of the decay positrons and electrons. The goal is to measure and describe the field distribution with a precision better than 10^{-3}. A reasonable cooldown time for the system should be less than 10 days and the ramp-up time to 1 T should be less than 2 hours.

Parameter	Value
Nominal field strength	1.0 T
Maximum field strength	2.6 T
Field inhomogeneity $\Delta B/B$	$\leq 10^{-3}$
Field stability $\Delta B/B$ (100 days)	$\leq 10^{-4}$

Table 3.3: Requirements for the Mu3e magnet [28].

3.3 First Cooldown

The cryostat has a single vacuum space which can be evacuated using a valve fitted to one of the cryostat side turrets. Before cooldown, it is necessary that this space is evacuated at a pressure of $< 10^{-4}$ mbar. The cryostat was pumped down to a pressure of 7×10^{-5} mbar. The cooldown procedure was then initiated without using liquid nitrogen. The system reached base temperature ($<$4 K) after approximately 7.5 days. According to the manufacturer, by using liquid nitrogen the system would have reached base temperature after approximately 6 days. Figure 3.6 shows the cooldown data of all temperature sensors of the magnet system. Two more sets of cooldown data can be found in Appendix A.

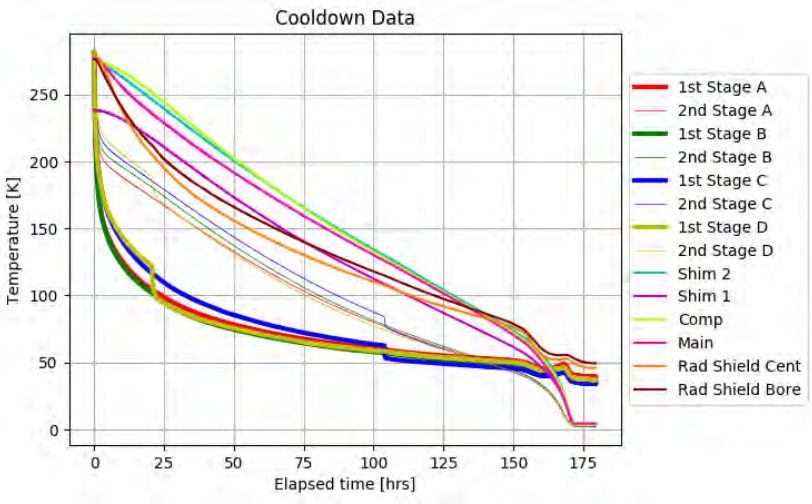

Figure 3.6: First cooldown data of the Mu3e magnet system. Note that Shim 1 starts from a lower temperature reading, due to wrong calibration. Letters A-D represent the four cryocoolers.

3.4 Performance Tests

Three main tests were carried out to assess the performance of the system:

1. Ramp-up to +1T and testing the two shim coils.
2. Ramp-up to +2.6T.
3. Ramp-up to -2.6T.

3.4.1 First ramp-up to +1T

The magnet was ramped up to +1T, with the current and ramp rates as indicated in Table 3.4. It takes around 50 minutes for the field to reach +1T and this was the first real test involving current in the coils. During the first ramp-up it was important to monitor the forces on the load cells and re-centre the cryostat if necessary. The procedure went very smoothly and no re-centering was necessary since the load cells showed a very balanced configuration, as it can be seen from Figure 3.7d, where during the first 50 minutes all four load cells record an increase in the force. The next step was to test the performance of the two shim coils. Shim 1 and Shim 2 were ramped up simultaneously to +60 A and -50 A respectively. According to the

manufacturer, this is the absolute limit of what should be done due to the huge forces that it creates on the cryostat, as shown in Figure 3.7d during the time period from 50 to 85 minutes in the test. Finally only one of the two shim coils was ramped up to +60 A, creating tolerable forces on the cryostat. Whenever there is current change, there is a slight increase in the temperature of the coils and the cryocoolers, as it can be seen in Figure 3.7b and Figure 3.7c. This is expected and the effect is minimal, causing no problems to the system.

Coil	Main	Compensation	Shim 1	Shim 2
Ramp Rate [A/s]	0.03	0.0278	N/A	N/A
Current [A]	98.9	72.0	0	0

Table 3.4: Nominal current and ramp rates for +1T [37].

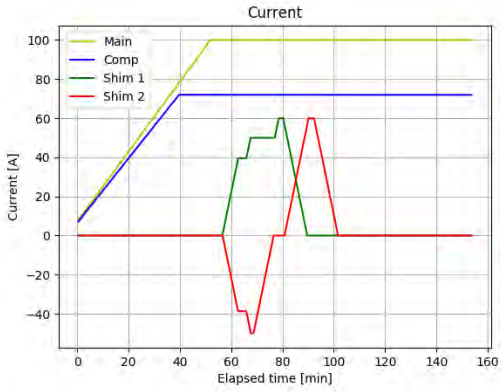

(a) Current in each coil.

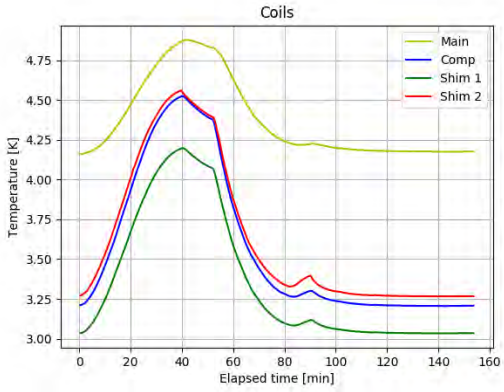

(b) Temperature of each coil.

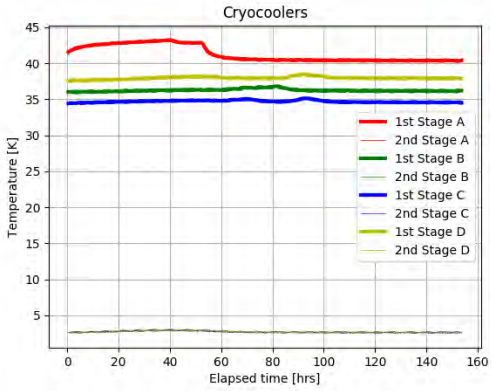

(c) Temperature of cryocoolers.

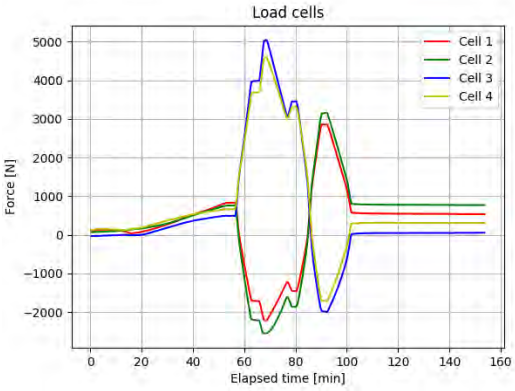

(d) Forces on each load cell.

Figure 3.7: First ramp-up to +1T data.

3.4.2 First ramp-up to ± 2.6T

According to the manufacturer the maximum field the magnet is capable of generating is 2.6 T, using the current and ramp rates shown in Table 3.5. This test was initiated after the magnet had reached a field of +1 T. Overall it takes around 160 minutes for the main coil to reach the specified amount of current. In order to limit heat dissipation in the superconductor the ramp rate is decreased by a factor of 2 once a coil reaches a current of 200 A. This test also went very smoothly and no problems were encountered. Large forces were acting on the cryostat due to the presence of such strong magnetic field, essentially bringing the system close to its limits. This is shown in Figure 3.8d. It is also worth noting that cell 4 behaves differently due to a soldering problem which was fixed at a later time. Same as before, the temperature of the coils and the first stages of the cryocoolers increase slightly and after around 1 hour it drops to base temperature once again. This can be seen in Figure 3.8b and Figure 3.8c. Opposite polarity can be achieved by simply reversing the sign of the current in each coil, as shown in Table 3.6. For the Mu3e experiment a field with an opposite polarity will allow the collaboration to carry out consistency checks as the electrons and positrons reverse their curvature if the direction of the field is reversed. The results are essentially identical to the +2.6 T case, as can be seen in Figure 3.9.

Coil		Main	Compensation	Shim 1	Shim 2
Ramp Rate [A/s]	0A <I <200A	0.03	0.0278	N/A	N/A
	I >200A	0.0146	0.0146	N/A	N/A
Current [A]		259.0	187.2	0	0

Table 3.5: Nominal current and ramp rates for +2.6T [37].

Coil		Main	Compensation	Shim 1	Shim 2
Ramp Rate [A/s]	0A >I >-200A	-0.03	-0.0278	N/A	N/A
	I <200A	-0.0146	-0.0146	N/A	N/A
Current [A]		-259.0	-187.2	0	0

Table 3.6: Nominal current and ramp rates for -2.6T [37].

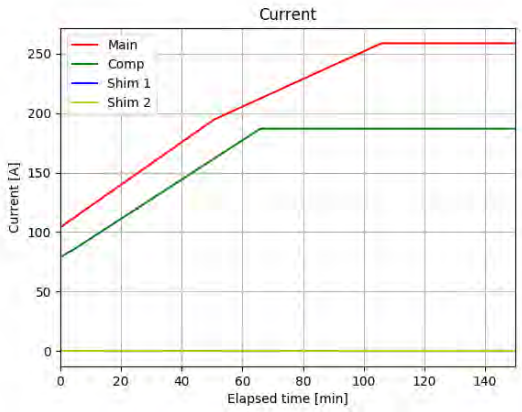

(a) Current in each coil.

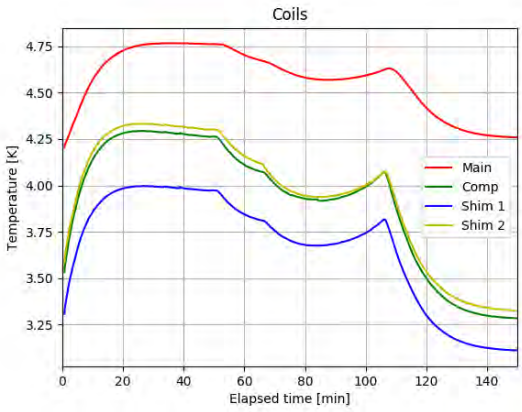

(b) Temperature of each coil.

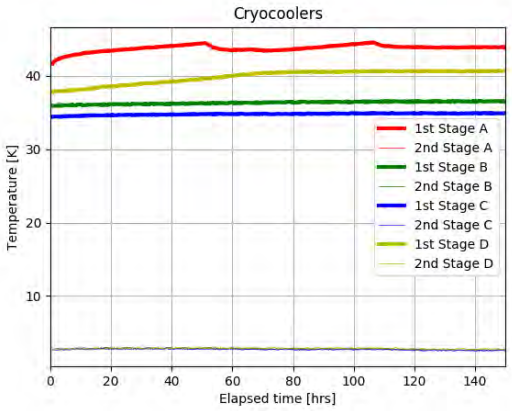

(c) Temperature of cryocoolers.

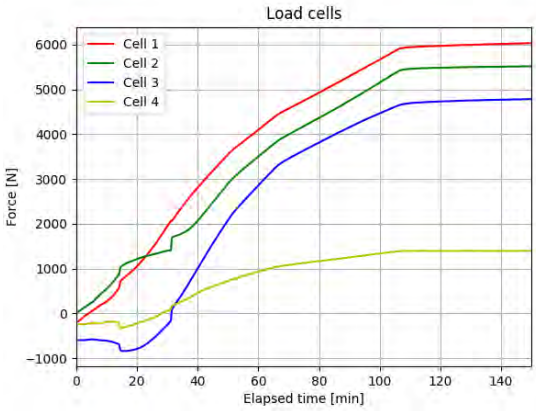

(d) Forces on each load cell.

Figure 3.8: First ramp-up to +2.6T data.

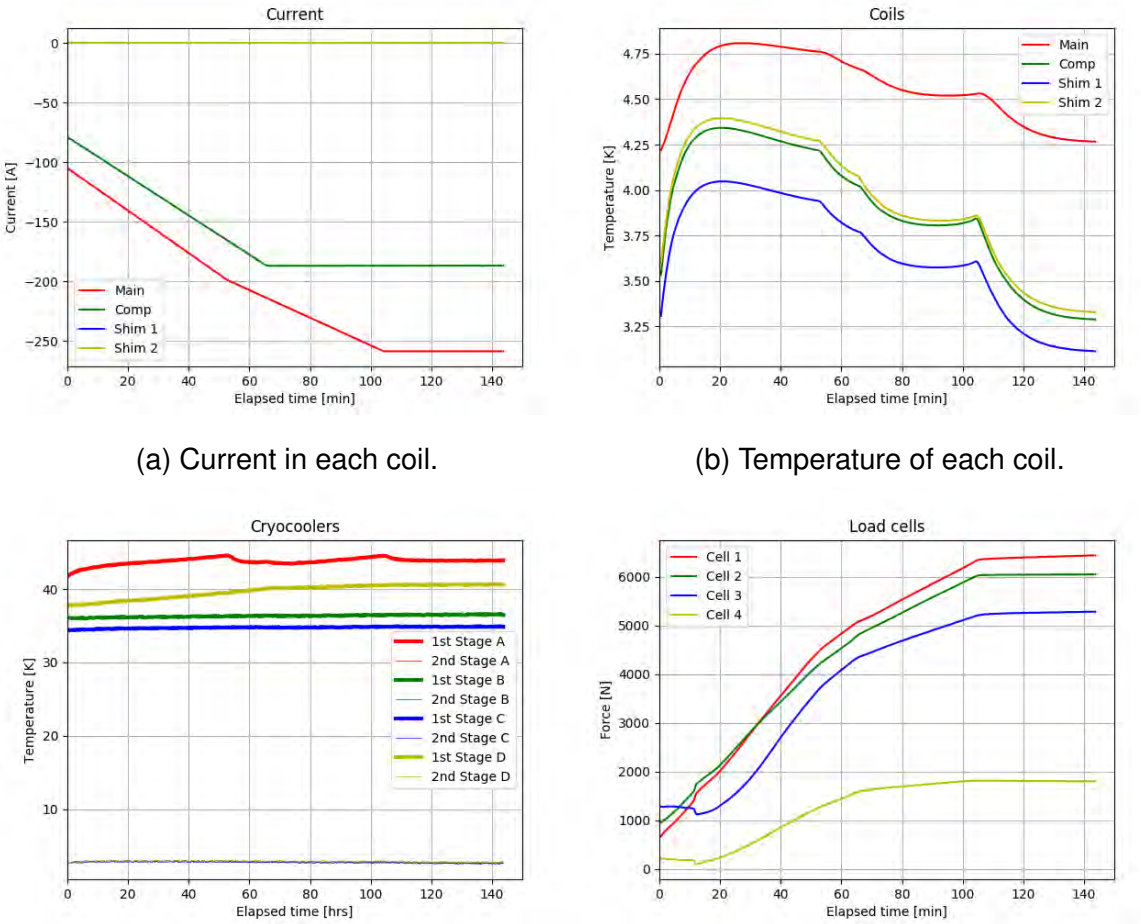

(a) Current in each coil.

(b) Temperature of each coil.

(c) Temperature of cryocoolers.

(d) Forces on each load cell.

Figure 3.9: First ramp-up to -2.6T data.

3.5 Magnetic Field Measurements

A simple Hall probe was used for all the measurements. The probe was connected to a steady current source providing 150 mA of current and it was mounted at the end of a long aluminium rod attached to the central opening of the end flange at one end of the bore tube. This allows the rod to move freely inside the magnet and measurements can be made along the axis of the beam, namely the z-axis. Off-axis measurements can be made using the exact same method but attaching the rod to the one of the two smaller openings located at a radial distance of 35 cm from the axis, as shown in Figure 3.10. Due to space confinements in the experimental hall at PSI, only one side of the magnet was scanned, although in principle the field should be perfectly symmetric on the other side of the magnet.

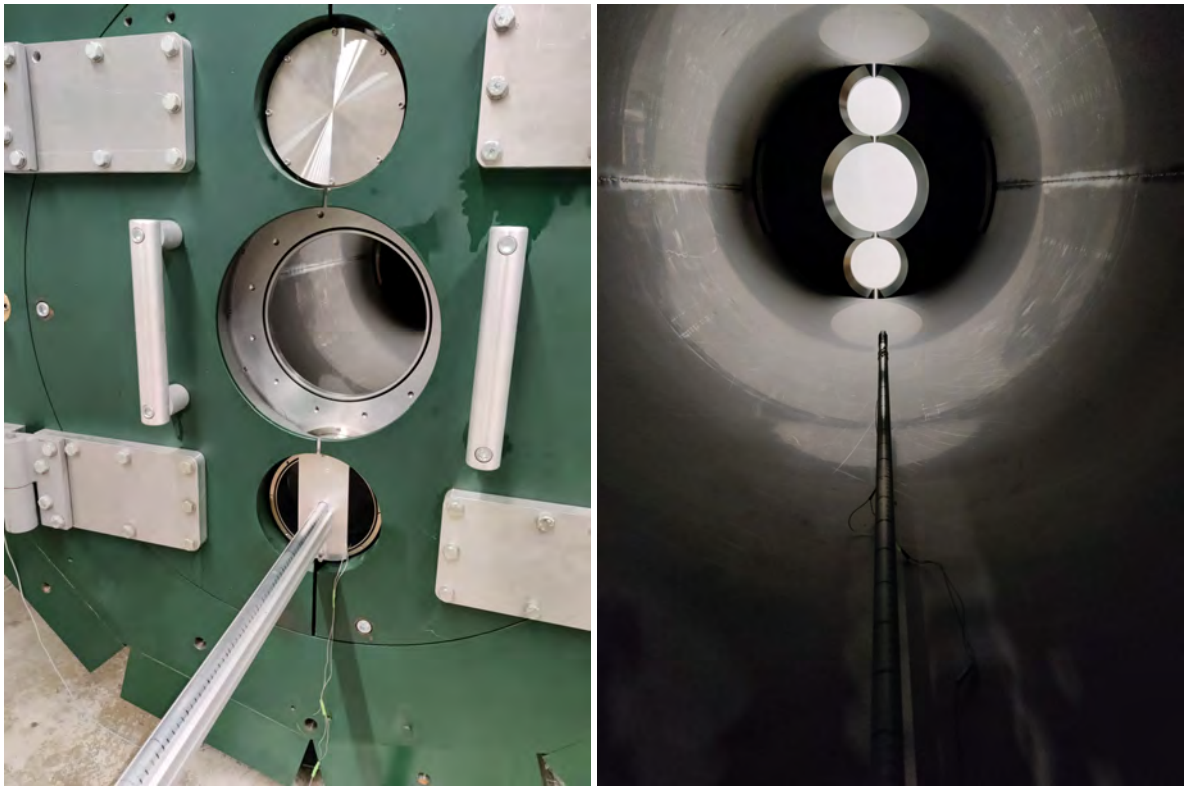

Figure 3.10: Setup used for measurements along a radius of 35cm from the z-axis. From measurements on the z-axis the same setup was used but the rod was attached to the central opening.

3.5.1 On-axis

By injecting into the coils the amount of current specified by the manufacturer, a slightly stronger field than 1 T is generated, as can be seen in Figure 3.11a. Nevertheless the difference between the measurements and the simulation from the manufacturing company is consistent along the z-axis with a value of approximately 2 mT. A slight positive gradient is also generated which can be removed or increased by changing the current in the compensation coil. A flat field of exactly +1 T can be achieved by scaling down the current in the main coil and compensation coil, as can be seen in Figure 3.11b. The field on the z-axis is 1T$\pm$1mT within $\pm$60 cm from the central plane of the system. A positive or a negative field gradient of any size can be achieved by adjusting the current in the compensation coil, as shown in Figure 3.12a. For the Mu3e experiment a field gradient can be used to help remove perpendicular tracks that recurl several times inside the central station of the pixel tracker. For more subtle changes one can also use the two shim coils, as shown in Figure 3.12b.

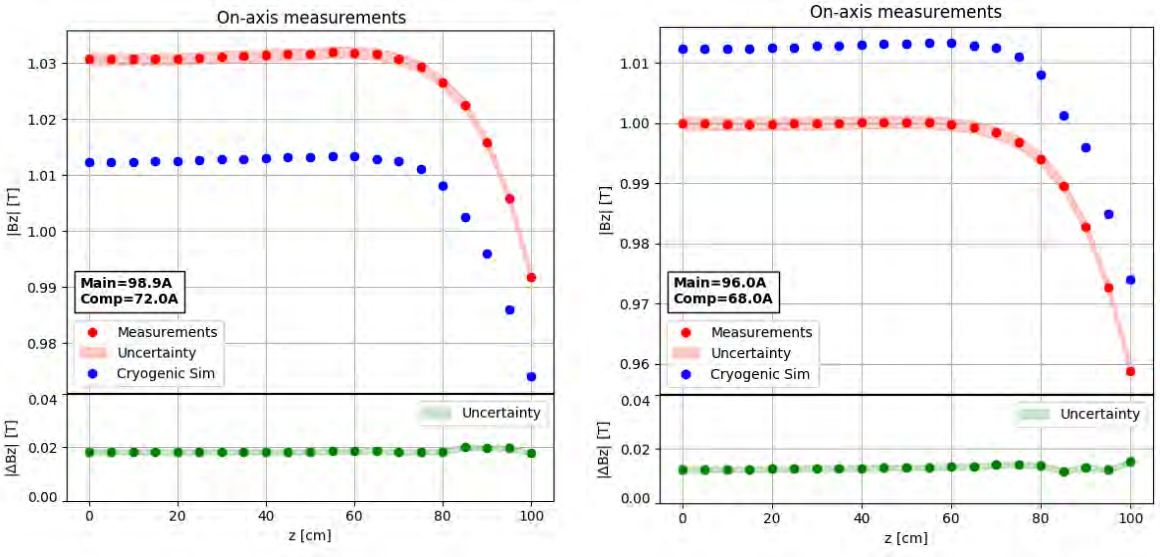

(a) Field profile using information from Cryogenic Ltd.

(b) Field profile by adjusting current for +1T field.

Figure 3.11: Measurements along the z-axis.

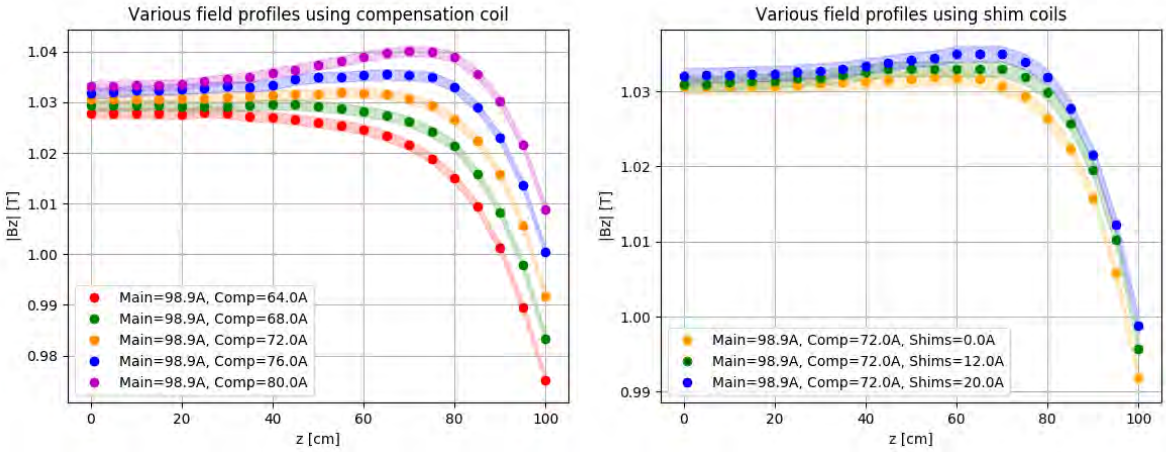

(a) Field gradient using compensation coil.

(b) Field gradient using shim coils.

Figure 3.12: Various field profiles along the z-axis.

3.5.2 Stability

The stability of the field is an important factor when it comes to the performance of the system, as the reconstructed momentum of the decay particles depend directly on the value of the magnetic field. Any fluctuations in the magnetic field over time will increase the uncertainty in these measurements, it is therefore important to assess the stability of the field. In order to do this, the Hall probe was positioned at the centre of the magnet (x=y=z=0) and a reading of the voltage was recorded every 1 s for a period of 1 hour. A field of +1 T was generated using the current and ramp rates indicated in Table 3.4. The field stability is shown in Figure 3.13.

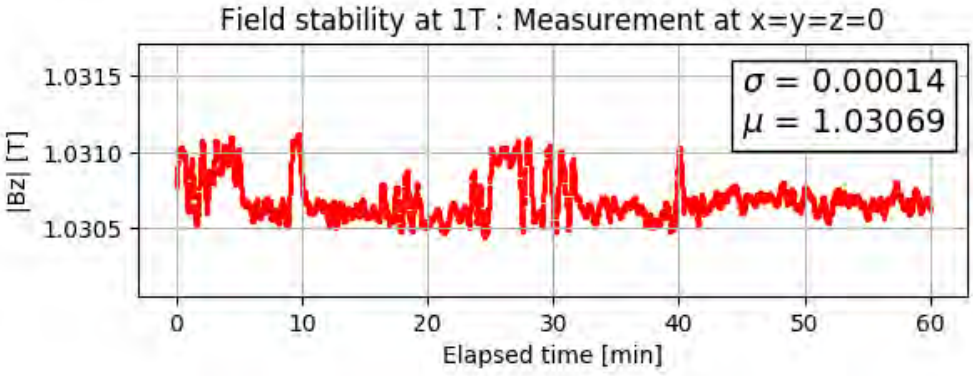

Figure 3.13: Field stability at 1 T over a time period of 1 hour.

For this kind of measurement, a very steady current source is required, due to the fact that the Hall probe is very sensitive to slight deviations in the amount of current. During these measurements, the amount of current in the Hall probe was fluctuating between 149.9 – 150.1 mA, so it is not clear to what extend the magnetic field itself fluctuates. In reality, the observed fluctuations are most likely present due to the unstable current source. Nevertheless, the measured fluctuations are at a level of $<$1 mT.

3.5.3 Off-axis

In this section the measurements were made along a radius of 35 cm, scanning only one side of the magnet. The difference between the hall probe measurements and the simulation from Cryogenic Ltd is consistent with the measurements made along the z-axis. For Figure 3.14a the amount of current used was the one indicated in Table 3.4 where as for Figure 3.14b the amount of current used was the same as in Figure 3.11b, i.e. 96.0 A for the main coil and 68.0 A for the compensation coil. Same as before, different field profiles can also be generated simply by changing the current in the compensation coil, as shown in Figure 3.15.

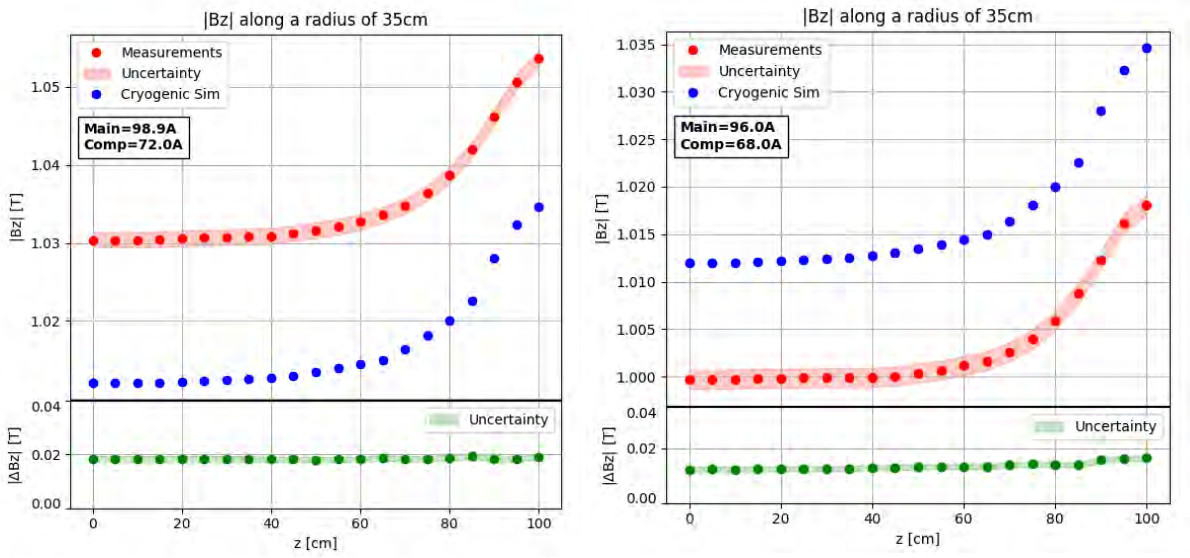

(a) 1T field using information from manual.

(b) Current adjusted for 1T.

Figure 3.14: Measurements along a radius of 35cm.

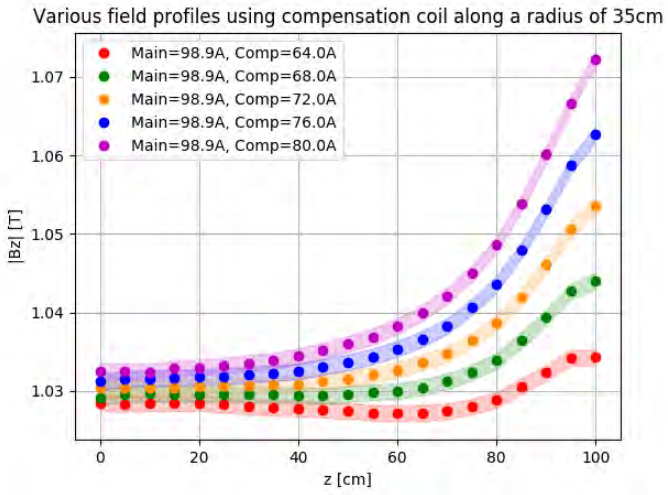

Figure 3.15: Various field profiles along a radius of 35cm

3.5.4 Uniformity

The field generated depends solely on the amount of current flowing through the coils. There is an infinite number of current configurations by which the field at the centre of the magnet is kept fixed at 1 T, as shown in Figure 3.16. In this section 10 such configurations, labelled from 1 to 10, are further examined. Depending on the required field gradient, different uniformities can be achieved. The field gradient depends only on the amount of current in the compensation coil.

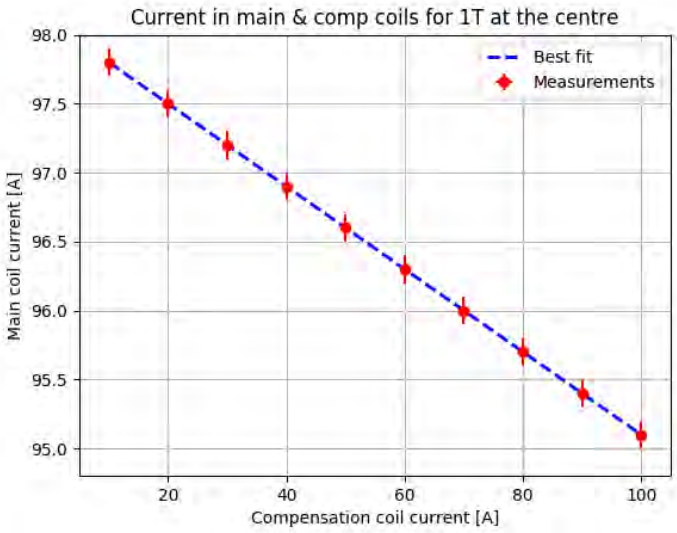

Figure 3.16: Amount of current in main and compensation coils for a field of 1T at the centre of the magnet. Numbers indicate the configuration number.

Figure 3.17a and Figure 3.17b show the field gradient at various positions on the z-axis and on R=35 cm respectively as a function of the configuration number. For field gradients on the z-axis, configurations 1 – 6 generate a negative field gradient where as configurations 8 – 10 generate a positive field gradient, as shown in Figure 3.17a. Using configuration 7 there is no gradient, i.e. a flat field is generated. For field gradients on R=35 cm, configurations 1 – 5 generate a negative field gradient where as configurations 7 – 10 generate a positive field gradient, as shown in Figure 3.17b. Configuration 6 seems to be the closest one for a flat field on a radius of 35 cm. By choosing configuration 7 we can conclude that the field is 1T$\pm$1mT in the central cylindrical region with a length of 60 cm and a radius of 35 cm.

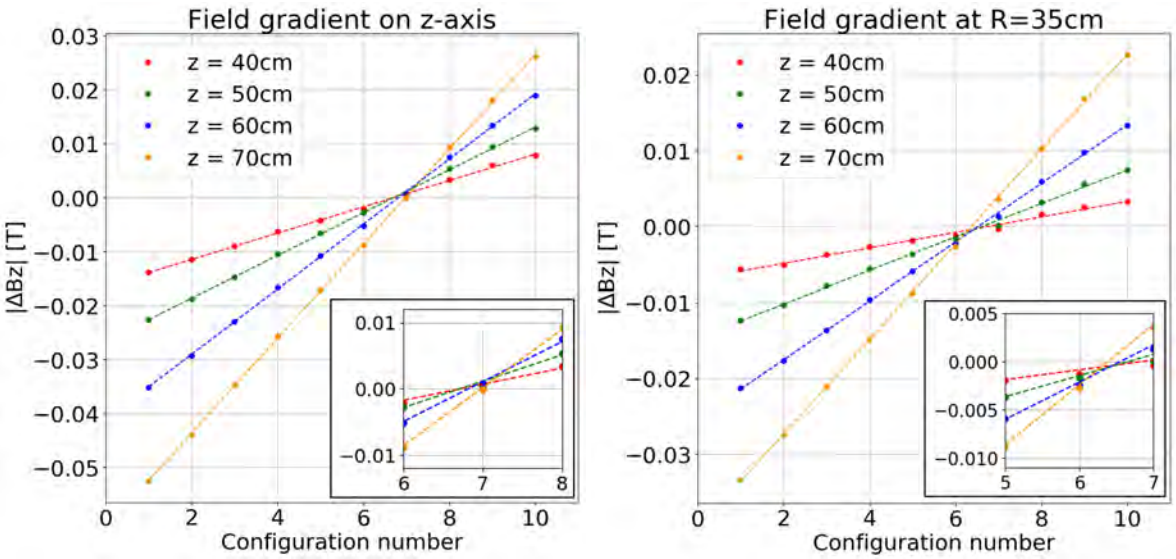

(a) On z-axis.

(b) R=35cm.

Figure 3.17: Field gradient at different positions on the z-axis and along a radius of 35cm.

3.6 First Warmup

The system can be allowed to warm up by switching off all four compressors which supply the cryocoolers with Helium gas. It takes around 7.5 days for all parts of the system to reach room temperature which is essentially the same time it takes for the system to reach base temperature. Figure 3.18 shows the warm-up data of all temperature sensors of the magnet system.

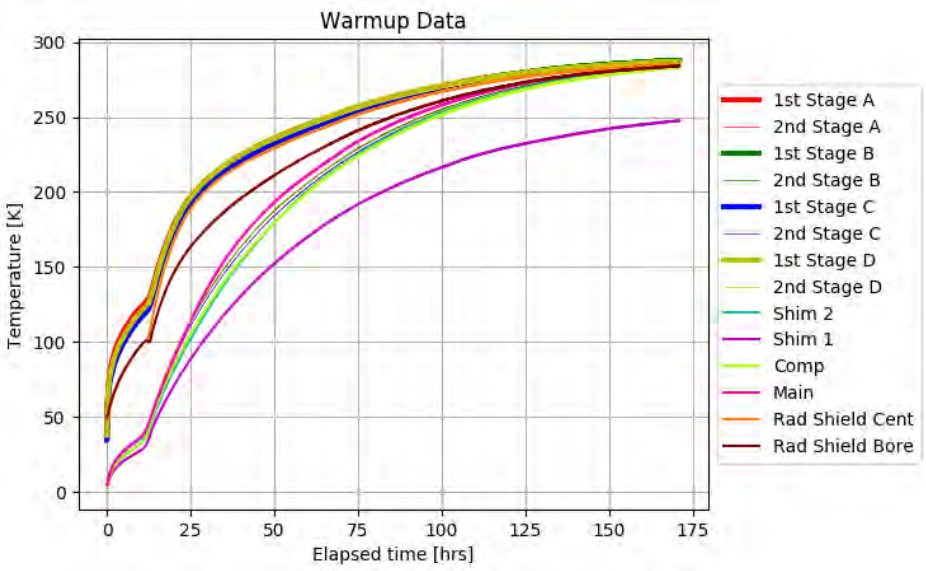

Figure 3.18: First warmup data of the magnet system. Note that for Shim 1 there is an offset of 40K as this was also the case during cooldowns.

3.7 Summary

The Mu3e magnet system performs very well in all the tests and meets all the requirements. Depending on the demands of the Mu3e experiment, it was shown that different field profiles can easily be generated. It takes around 7.5 days for the system to reach base temperature which is less than the 10 days that was put as a requirement. The stability of the field at the centre of the magnet was found to be less than 1 mT over a period of 1 hour. In the future, longer time periods will be necessary before the first phase of the experiment and also at different positions along the z-axis. This can be further improved by using a more stable current source for the Hall probe (precision <0.1 mA) or even a suitable NMR probe. The system was found to be capable of generating a field of various profiles in the range of 1–2.6 T. Due to the available equipment and also the fact that the Hall probe is not calibrated for a field over 2 T, no measurements were made at 2.6 T. At this range the use of an NMR probe is inevitable for the precise measurement of the field. A field of 1 T $\pm$ 1 mT in the central cylindrical region with a length of 60 cm and a radius of 35 cm can be generated.

4 Magnet Simulation

In physics and science in general, simulations play a very important role and many useful conclusions can be drawn from them. In experimental high energy physics magnets are everywhere and it is crucial that they generate the required field because all measurements, such as track radius and track momentum depend on it. Since it is practically very difficult to make field measurements in the entire volume of the magnet, a magnet simulation can give information on the uniformity of the magnetic field generated but it can also serve as an input to the G4Beamline simulation, which will be discussed in Part III of the thesis. In the context of this thesis, a simulation of the Mu3e magnet was developed using the Radia software [38]. Radia is a fast multi-platform software dedicated to the computation of 3-D magnetostatics and it is optimized for the design of undulators and wigglers made with permanent magnets, coils and linear/nonlinear soft magnetic materials. It can solve a variety of problems with isotropic and anisotropic magnetic materials and with current-carrying elements of different shapes. The user can define volume objects and certain material properties can be applied to them. Each magnetic object is subdivided into a number of smaller pieces for which one tries to solve for the general problem in terms of the magnetization. The solution is performed by building a large matrix in memory which represents mutual interactions between the objects. This is known as the Interaction Matrix. The final magnetization in each small object is obtained iteratively, by a sequence of multiplications of the Interaction Matrix by the instant magnetization vector, taking also into account the material properties. Once this computation is done, the magnetic field can then be computed anywhere in 3-D space whatever the distance to the field-producing objects is. The performance of the software is essentially limited only by the available RAM in the computer. Figure 4.1 shows the work flow of the Mu3e magnet simulation. In this

simulation, the coils and the passive iron shield were simulated according to the data provided by the manufacturer and as described in chapter 3. This is depicted in Figure 4.2. Since we are only interested in the resultant field profile, all non-magnetic parts such as the cryostat, the bore tube and the end-flanges are not included in the simulation. The vectorial field generated by the coils is shown in Figure 4.3. The passive shield is simulated using steel material which is the same as the real one. For simulating the coil windings, no material is specified but in this case the material does not play any role due to the fact that the amount of current in the coils can be simulated at any value. For technical reasons the openings on both sides of the magnet are simulated as squares but in reality they are round. In principle, this could slightly alter the magnetic field at the two edges of the magnet. Two configurations were simulated, one using the nominal amount of current in the coils (Configuration 1) as specified by the manufacturer which generates a field slightly higher than 1T at the centre of the magnet and one using an adjusted amount of current in the coils (Configuration 2) which generates a field of exactly 1T at the centre. These configurations are summarized in Table 4.1.

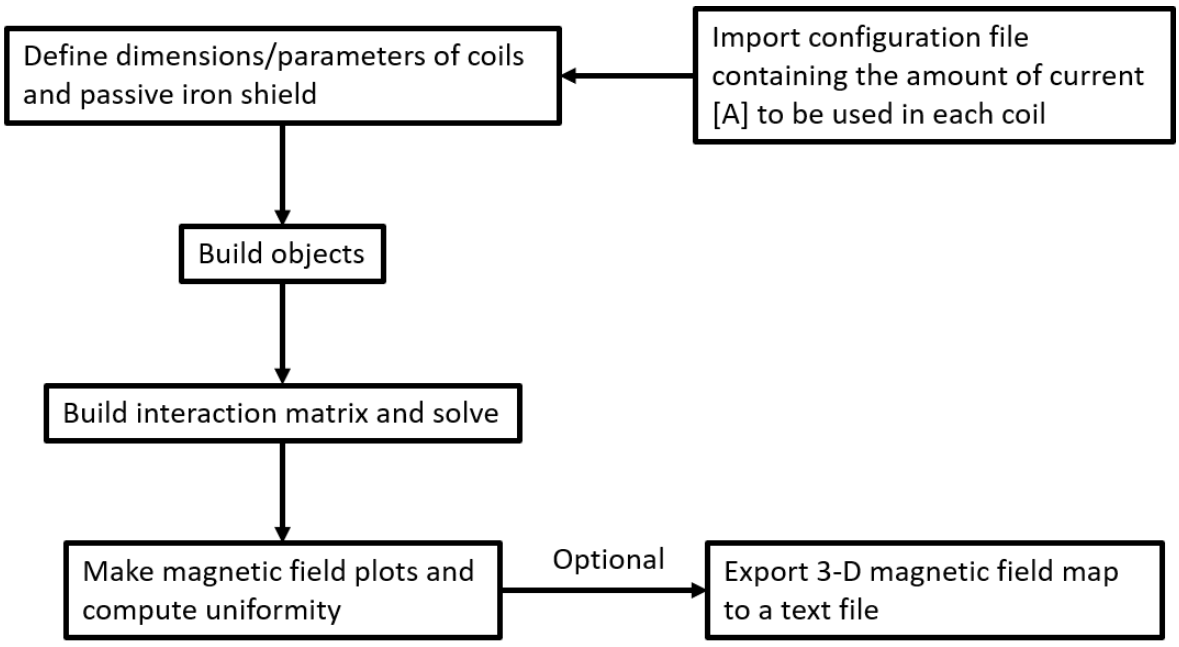

Figure 4.1: Work flow of the Mu3e magnet simulation.

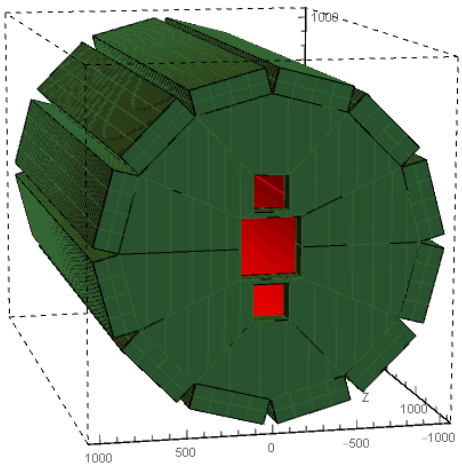

Figure 4.2: Picture of the Mu3e magnet as simulated using the Radia software. The passive iron shield is shown in green and the coils in red.

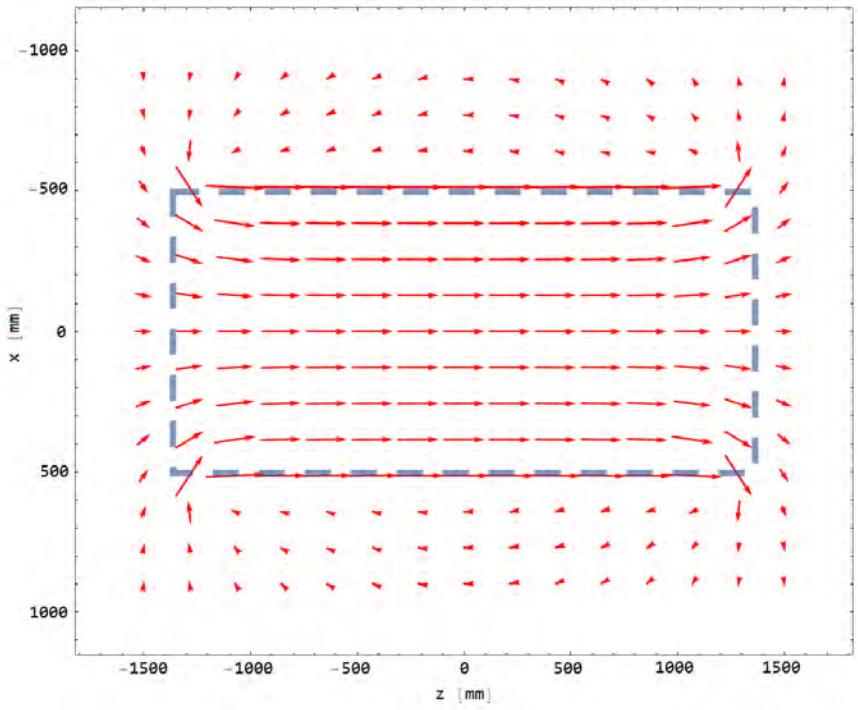

Figure 4.3: Vectorial 2-D plot in the x-z plane of the magnetic field generated by the magnet in the Radia simulation. The position of the bore tube is shown in dashed blue line.

	Current [A]		
Configuration	Main Coil	Compensation Coil	Shim Coils
1 (Nominal)	98.9	72.0	N/A
2 (Adjusted)	96.0	68.0	N/A

Table 4.1: Configurations simulated using the Radia software.

4.1 Magnetic Field Maps

The goal of this study is to have a magnet simulation that generates a magnetic field as close to the real field as possible. By using configuration 1 (nominal) a magnetic field can be generated which is very close to the real one that was measured using the Hall probe. This is shown in Figure 4.4a and Figure 4.4b where the field is computed on the z-axis and along a radius of 35cm respectively. The field is symmetric in both the x-y and y-z planes as it can be seen in Figure 4.4c and Figure 4.4d respectively. By using configuration 2 (adjusted) the field generated still agrees with the Hall probe measurements on both the z-axis and on a radius of 35cm as it can be seen in Figure 4.5a and Figure 4.5b respectively. In comparison with the nominal configuration, a similar trend can be seen in the x-y and y-z planes where the field becomes weaker as you move away from the centre in the x-y plane and stronger as you move longitudinally away from the centre in the y-z plane. This is shown in Figure 4.5c and Figure 4.5d. For both configurations, the agreement between the simulation and the measurements seems to be around 1mT or less, although the uncertainty comes directly from the precision of the Hall probe used.

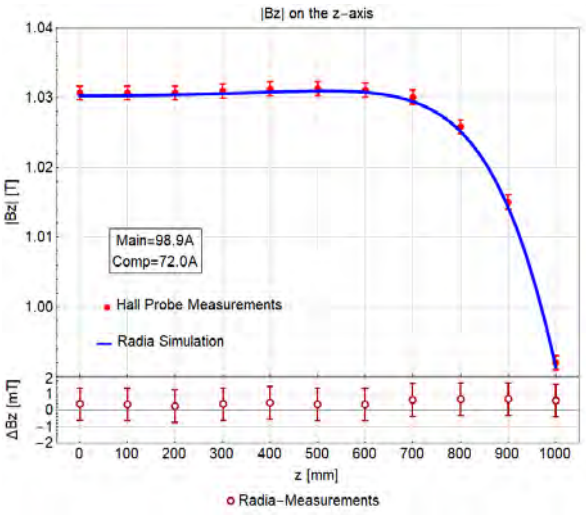

(a) |Bz| on z-axis.

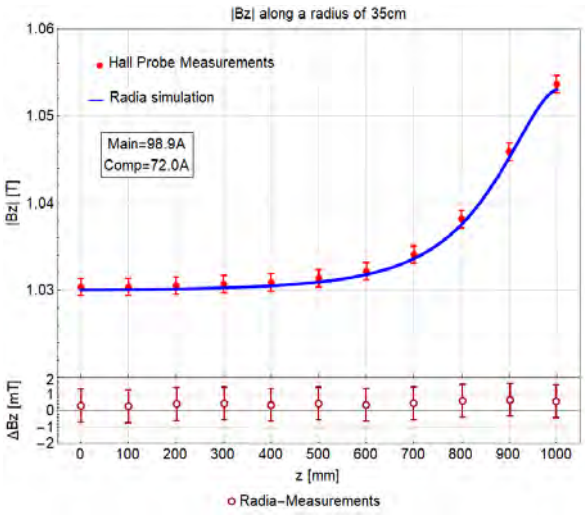

(b) |Bz| on R=35cm.

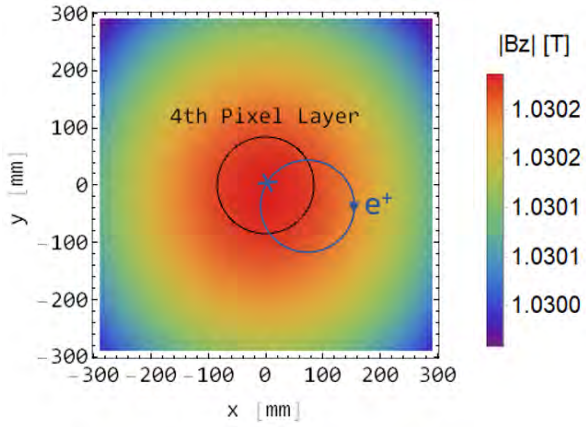

(c) |Bz| in x-y plane at z=0.

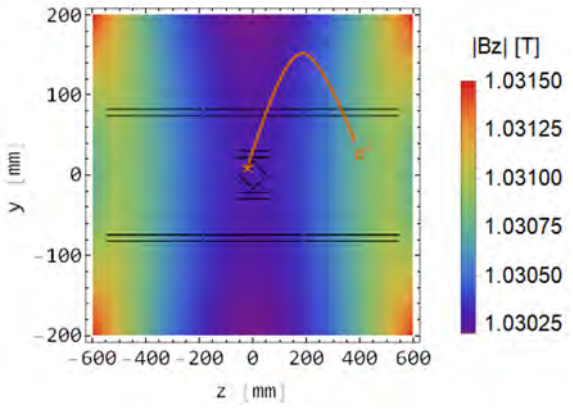

(d) |Bz| in y-z plane at z=0.

Figure 4.4: Simulation field maps using nominal configuration.

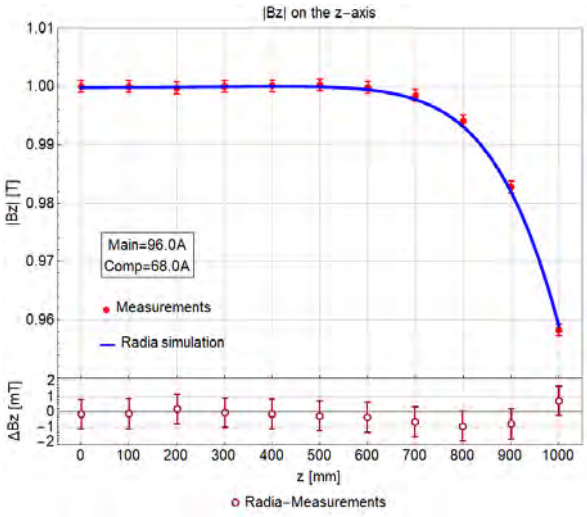

(a) |Bz| on z-axis.

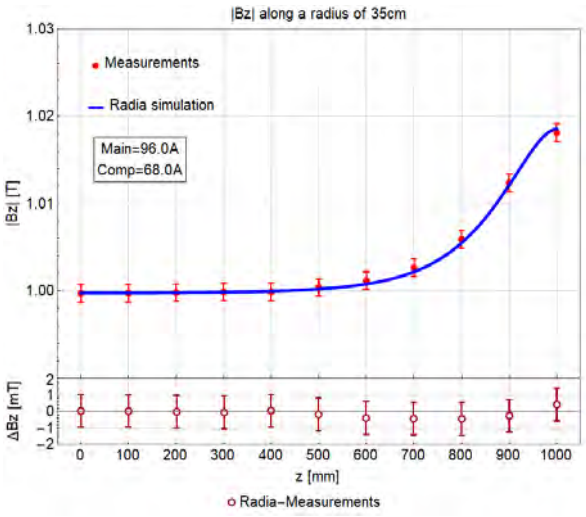

(b) |Bz| on R=35cm.

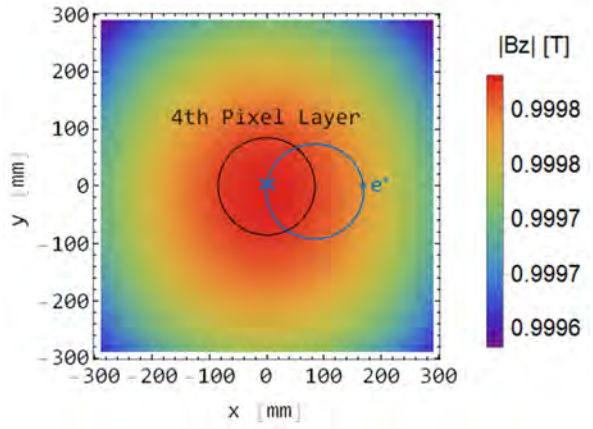

(c) |Bz| in x-y plane at z=0.

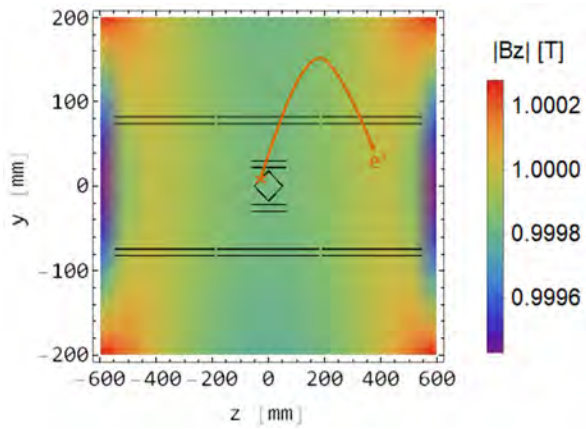

(d) |Bz| in y-z plane at z=0.

Figure 4.5: Simulation field maps using adjusted configuration.

4.2 Uniformity

The magnetic field uniformity is an important factor when analysing experimental data. Inside a certain region of space, the uniformity of any magnetic field can be computed using the following equation:

$$Uniformity = \frac{|\Delta B_z|}{|B_{z,mean}|} \tag{4.1}$$

where, $|\Delta B_z| = |B_{z,max} - B_{z,min}|$.

Mu3e experiment will run in three phases. Moving from one phase to the next one, the detector volume will become larger. Assuming muons decay on the surface of the target, the decay electrons travel in helical paths inside the detector volume and they will occupy a cylindrical volume formed by their longitudinal distance travelled and their radius. At their furthest point from the centre of the target they will be approximately at a distance of two times the track radius in the x-y plane. The radii of the tracks from a background sample of events are shown in Figure 4.6. Track radii vary from 35mm to 200mm, with the mean value close to 125mm. In Mu3e smaller radii are not possible because such electrons do not have enough momentum to reach the outer pixel tracker and as a result no track is created. Thus in order to calculate the field uniformity for each experiment phase, the following cylindrical volumes may be defined:

- **Phase Ia:** Length = 400mm, Radius = 300mm
- **Phase Ib:** Length = 1100mm, Radius = 300mm
- **Phase II:** Length = 1800mm, Radius = 300mm

For all the above volumes, their centres coincide with the centre of the magnet (and consequently with the target too) and they represent the region where most of the decay electrons will fly through. Slight deviations in the field strength can affect the electron tracks due to changes in the Lorentz force acting on them. This in turn will have an effect on the measured transverse momentum of the electrons as this is calculated directly from their radius projected in the x-y plane. Table 4.2 summarizes the simulated field uniformity for each configuration and phase. According to the current plan for Phase Ia of Mu3e, a uniformity of less than 10^{-3} is required. This can

be achieved by using both the nominal and the adjusted configurations. However for phase Ib, configuration 2 generates a more uniform field compared to configuration 1. This does not seem to be the case for phase II, as both configurations generate more or less the same field in terms of uniformity.

	Configuration	
Experiment Phase	1 (Nominal)	2 (Adjusted)
Ia	1.7×10^{-4}	1.3×10^{-4}
Ib	1.1×10^{-3}	8.0×10^{-4}
II	1.4×10^{-2}	1.3×10^{-2}

Table 4.2: Simulated field uniformity for each configuration.

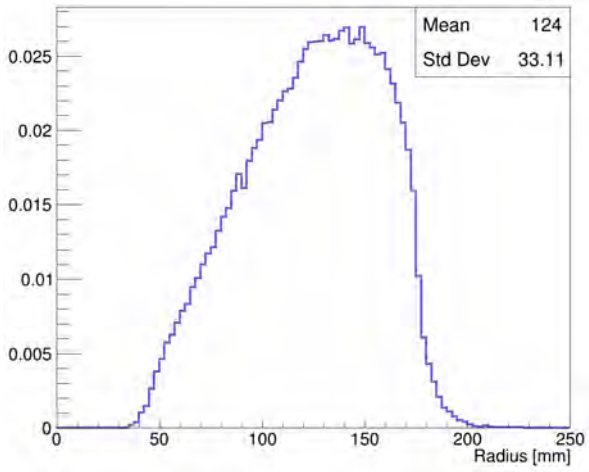

Figure 4.6: Track radii from a simulated background sample of events.

4.3 Force on quadrupole magnet

The last element of the beamline is a quadrupole magnet (see Figure 2.10) positioned at a distance of around 30 cm from the iron doors of the Mu3e solenoid. The quadrupole magnet is around 1 m tall with a very small base and has a weight of 1 tonne. A very large force can tilt the magnet or even pull it violently towards the iron shield. This can potentially cause severe damage to some parts of the experiment. For safety reasons it was therefore crucial to calculate the force generated on it. If the force is found to be large, then a support has to be built to hold the magnet in

place. Figure 4.7 shows the extended magnetic field along the z-axis inside and outside the solenoid for configuration 2. At the position of the quadrupole magnet the strength of the z component of the magnetic field is less than 20mT. This indicates that almost the whole field is essentially contained inside the solenoid. For simplicity only the outer iron of the quadrupole magnet was simulated. The force exerted on the quadrupole magnet was computed by utilising a Radia built-in function which calculates the force exerted on a magnetic object when placed inside a magnetic field created by a source object. In this case the quadrupole experiences a force which is generated by the total magnetic field produced by the coils (main comp) and the iron shield. The resulting force for the two simulated configurations is summarized in Table 4.3.

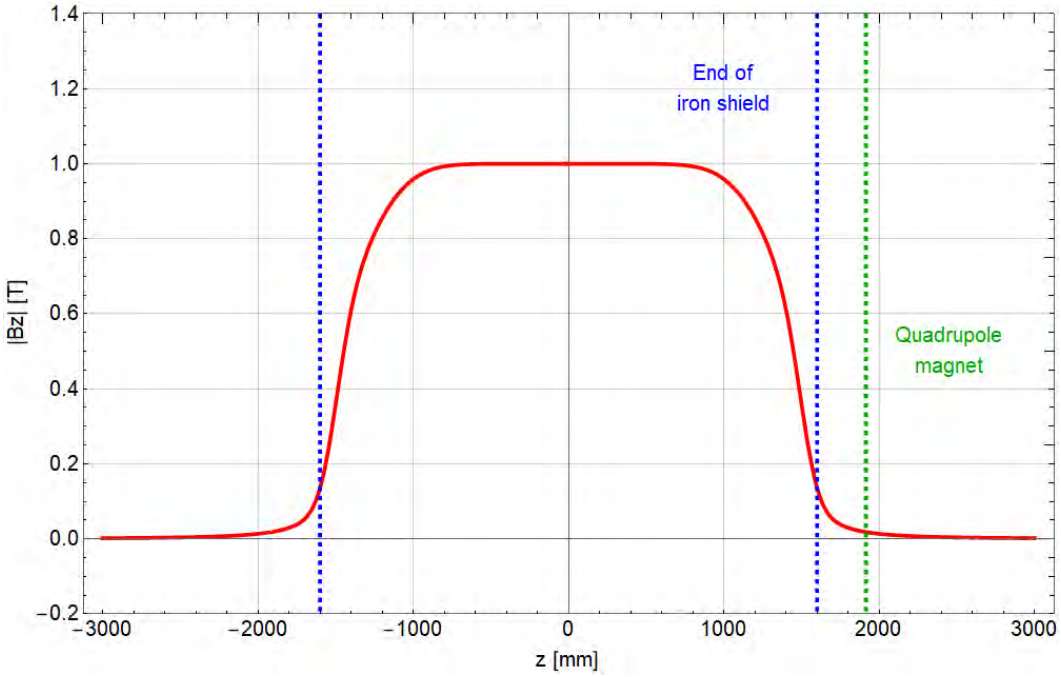

Figure 4.7: Magnetic field along the z-axis inside and outside the solenoid for configuration 2. The position of the quadrupole magnet is indicated using the dashed green line. Configuration 1 yields an almost identical field profile.

The results for both configuration show that the total force generated on the last quadrupole magnet is around 150-160 N and it is pointing almost solely along the z-axis towards the Mu3e solenoid, as expected. The force is relatively small given also the fact that the weight of the quadrupole is around 1 tonne. In practice, any force less than 500 N can be considered as safe. It can be therefore concluded that

no support is required to hold the quadrupole in place and no extra precautions are needed for the safe operation of the experiment.

	Configuration	
	1 (Nominal)	2 (Adjusted)
|Fx| [N]	9	8
|Fy| [N]	10	12
|Fz| [N]	158	153
|F| [N]	159	154

Table 4.3: Force generated by the Mu3e solenoid on the last quadrupole magnet of the beamline.

4.4 Summary

Despite the fact that the magnet simulation is not a exact copy of the real magnet, the simulated magnetic field is very similar to the actual magnetic field generated by the Mu3e magnet. According to the simulation, for Phase Ia of the experiment, field uniformities of $< 10^{-4}$ can be achieved by using both the nominal and the adjusted configurations. For Phase Ib, a similar field uniformity can be achieved by using the adjusted configuration. However for Phase II of the experiment the calculated magnetic field uniformity is above 10^{-2} for both configurations and more studies will need to be conducted in the future. No extra supports are required to hold the last quadrupole magnet of the beamline in place as the force acting on it is less than 500 N when the magnet operates at a field of 1 T.

Part III

Beamline Studies

5 The πE5 Beamline

The Mu3e Phase-I experiment will require muon intensities $O(10^8)$ muons per second and therefore the πE5 channel at PSI is the only facility in existence delivering these rates as a continuous source. Until now, the πE5 beam channel had been dedicated almost exclusively to the MEG experiment, but in the future the same channel will also host the Mu3e experiment. In order to minimize downtime during operational switch-over between the MEG II and Mu3e experiments, a new Compact Muon Beamline (CMBL), shown in Figure 5.1, has been developed to allow for the coexistence of the two experiments in the same area.

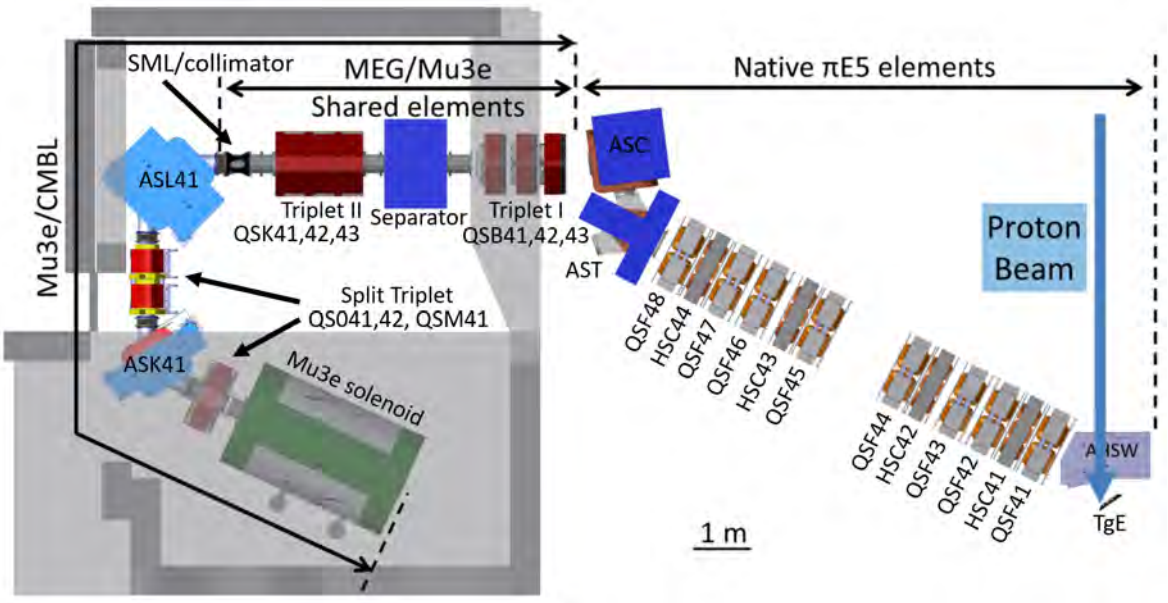

Figure 5.1: Top view of the CMBL and part of the πE5 area with all the beamline elements annotated.

The CMBL solution shares the elements that both experiments require, while it requires only the replacement of the superconducting beam transport solenoid of MEG II by a dipole magnet for Mu3e. It is an extension to the existing πE5 and MEG

beamline elements, including the two quadrupole triplets TI and TII, the separator Wien filter SEP41, and 120 mm collimator system, which blocks the unwanted part of the beam, such as positrons. This compact beamline allows the Mu3e solenoid to be placed in the front part of the πE5 area. After the collimator system, a 90° dipole bending magnet ASL41 is used and the next four beamline elements together form a "split triplet" solution via a quadrupole doublet QSO41 and QSO42, a 65° dipole ASK41, and the final quadrupole singlet QSK41 leading to the injection of the Mu3e solenoid. Surface muons are produced from stopped pion decays at the surface of the primary production target and the beam intensity peaks at around 28 MeV$/$c, close to the kinematic edge of the two-body momentum spectrum of pion decay. πE5 is a high-rate secondary beam channel that is mainly used for experiments with surface muons but can also provide muons, pions and electrons of either charge-sign at a momentum range between 10-120 MeV$/$c. The high rate makes it a perfect choice for the intensity frontier experiments such as MEG and Mu3e. Figure 5.2 shows a CAD model overview of the entire beam line from production (TgE) to the Mu3e spectrometer solenoid. The beam line for Mu3e mainly comprises of three parts: the πE5 channel ending with the ASC dipole, the shared MEG section of the beam line ending at the intermediate focus collimator system and a dedicated Mu3e part ending with the Mu3e solenoid. The Mu3e experiment requires the following beam properties:

- A continuous surface muon beam with a central momentum of 28 MeV/c.
- Minimization of beam related background, such as e^+, π^+ from the production target with equal momentum as the muons.
- A high transmission optics in order to minimize the beam losses.
- A small beam size at the position of the target, allowing for a relatively small target.

In more detail, the πE5 channel consists of the following parts:

- The part starting with the extraction dipole AHSW up to the ASC dipole was set up in the 90's [39]. This part consists of 3 dipole magnets and 12 quadrupole

magnets. All the elements are covered by concrete shielding for radiation safety reasons and are mounted on wagons in the shielding.

- The second part comprises of the MEG beam line elements from Triplet I up to the collimator system and were set up in 2005. Mu3e makes use of this well-proven setup, especially the Wien filter, which is necessary to eliminate unwanted beam background.

- The dedicated Mu3e components follow the MEG collimator system. Due to spatial limitations a 90° bending dipole is attached as close as possible to the MEG SML/collimator system, which is partially covered by a concrete shielding overhang and leaves only a very small gap to the rear shielding wall of the πE5 area. It is followed by the so-called "split triplet", that comprises of a split combination around the last dipole magnet ASK, of a QSO doublet with small lateral extent and a large aperture QSM singlet. Finally, the Mu3e spectrometer is placed at the end part of the beamline which will host the Mu3e experiment. As can be seen the limited space leaves very little freedom for the individual alignment of the elements and therefore also puts severe constraints on the beam optics.

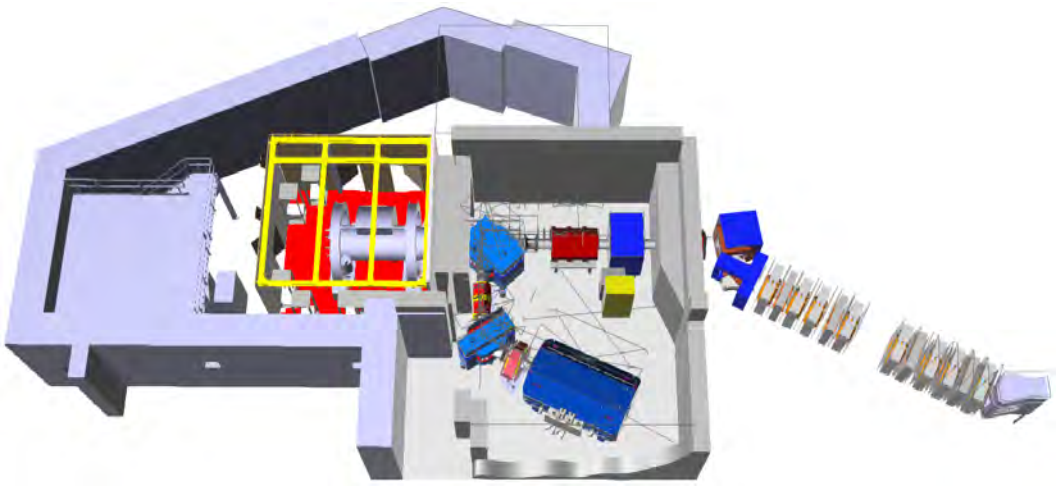

Figure 5.2: CAD model of the πE5 area. The MEG and Mu3e experiments can be seen at the top left and right corners respectively.

5.1 Beam production

5.1.1 High Intensity Proton Accelerator

The PSI High Intensity Proton Accelerator (HIPA) chain consists of a Cockcroft-Walton pre-accelerator that delivers 870 keV/c protons to two cyclotrons which further accelerate to a maximum energy of 590 MeV/c [40]. The Cockcroft-Walton pre-accelerator provides the first stage of acceleration where hydrogen gas is ionized to create negative ions, each consisting of two electrons and one proton. The ions are then accelerated by a positive voltage and reach an energy of 750 keV before both electrons are stripped off leaving a proton. The Injector II cyclotron first accelerates the protons to 72 MeV/c and then the protons are transferred to the Ring cyclotron where they are accelerated to their final energy. An image of the Ring Cyclotron is shown in Figure 5.3. The proton beam with maximum 2.4 mA current and 1.4 MW beam power, is directed through two rotating graphite target stations to produce pions and muons by nuclear interactions with a carbon target [41]. The layout of the PSI accelerator complex is shown in Figure 5.4.

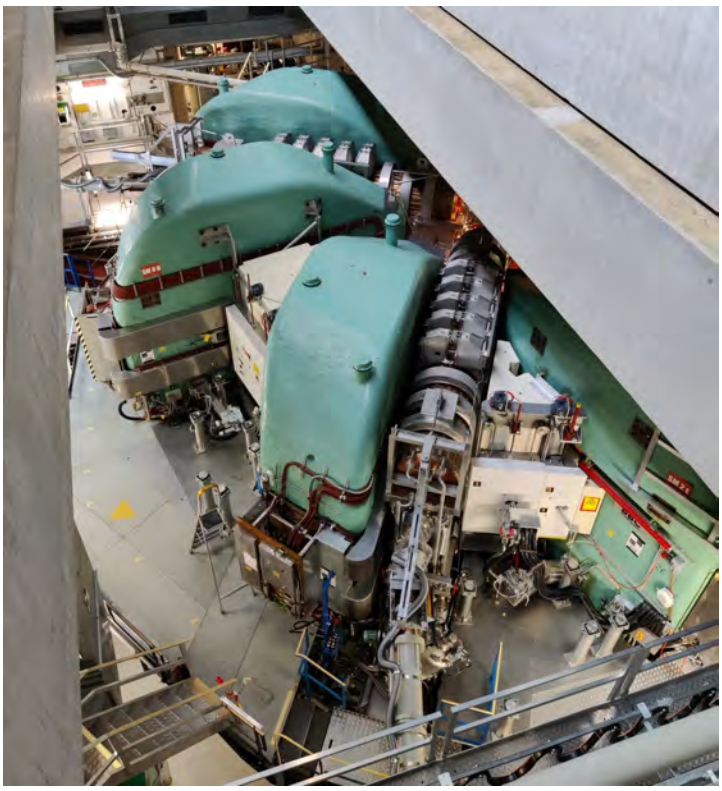

Figure 5.3: Part of the Ring Cyclotron at PSI.

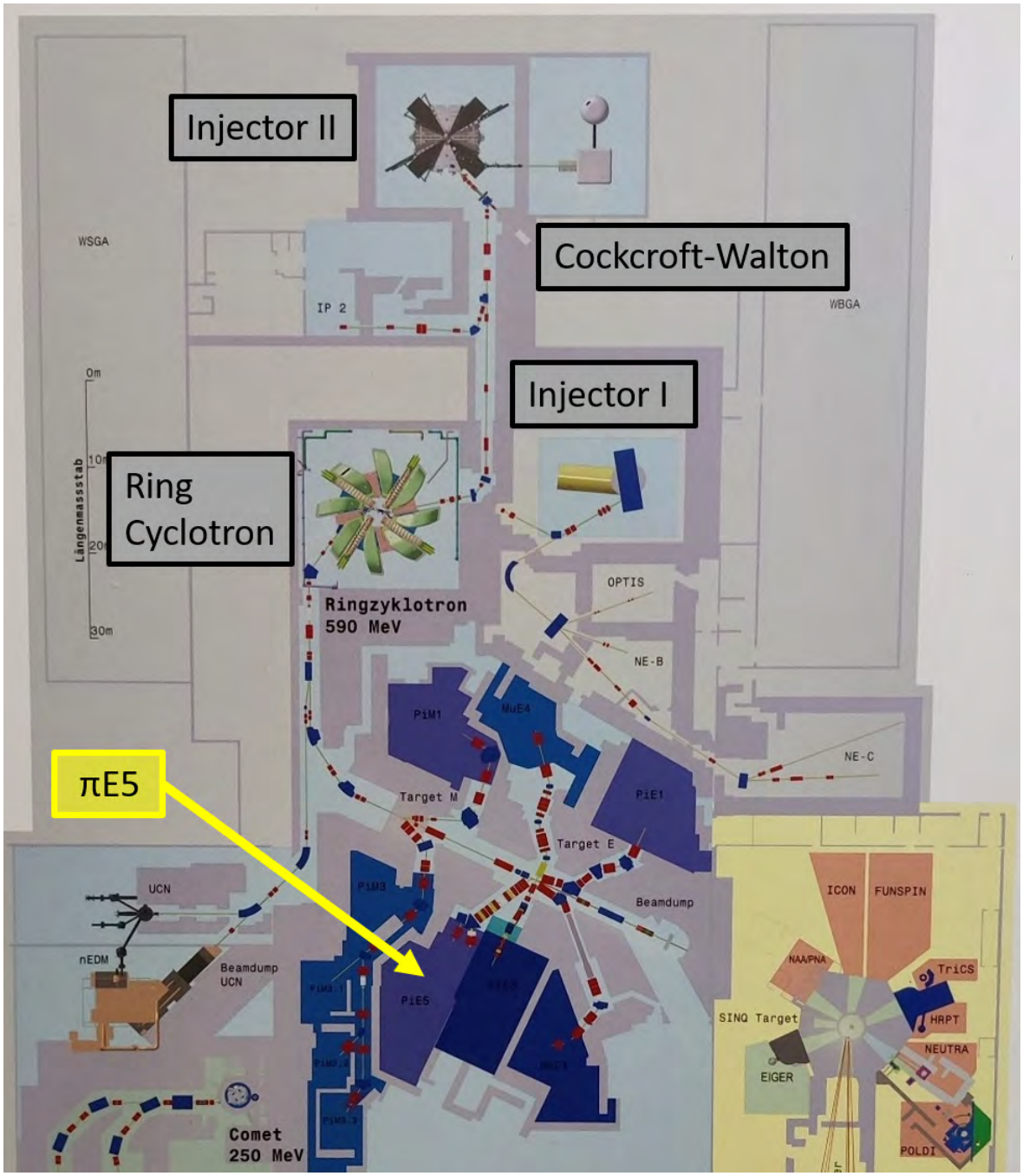

Figure 5.4: Part of the PSI accelerator complex.

5.1.2 Pion Production

The 590 MeV/c proton beam delivered by the ring cyclotron is directed on to the thick Target E (TgE) to produce pions through one of several nucleon-nucleon interaction in the target material. Protons hitting the target with energies above 290 MeV/c can produce Delta baryons which then quickly decay via the strong interaction to other nucleons and pions. Pions produced inside the target will either be stopped inside the target or they can leave the target if they have sufficient energy. The pions that exit the target volume can be captured by surrounding beamlines for use as pion beams or directed through a decay solenoid to produce a secondary muon beam. Those pions with sufficiently low momentum will be stopped inside the target and depending on the charge state, have very different kinematics inside the target leading to different final states for stopped pions. The various paths pions can take through the target volume is shown in Figure 5.5. Negative charged pions will lose energy while traversing the target and inevitably be captured in an atomic orbit around a nucleus. In contrast, positive charged pions will not form pionic atoms but may stop near the atomic region and decay. Depending on their momentum and where they originate, the decay of pions can result in three distinct classes of positive muons [42]:

1. Cloud muons.

2. Sub-surface muons (p < 26 MeV/c)

3. Surface muons (26 < p < 30 MeV/c)

Cloud muons originate from pion decay in flight, typically inside the target volume or in the region surrounding the target. These cloud muons will have momenta across the full momentum range with a maximum momentum near 90 MeV/c. Surface muons originate from the surface layer of the production target from stopped pions in the target and carry a unique kinetic energy due to the pion decay kinematics. Sub-surface muons are also created in the decay of stopped pions inside the target volume, but from deeper within the target than surface muons. These muons have a lower momentum ($<$26 MeV/c) which is a result of the increased material

these muons must pass through before exiting the target. The Mu3e experiment will use only surface muons.

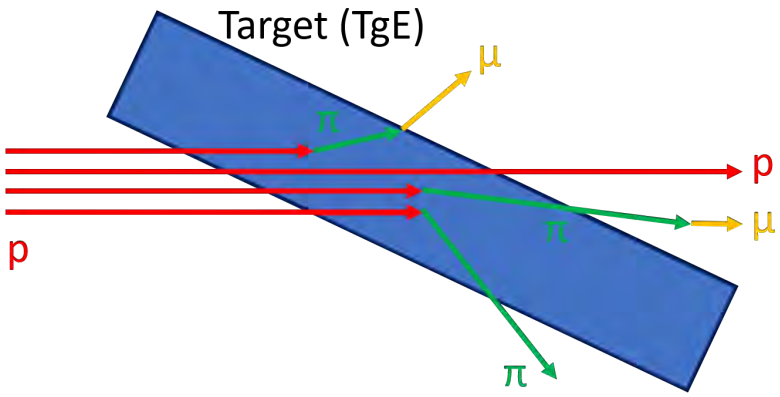

Figure 5.5: Pion and muon production inside or outside the target volume. Pions either decay outside the target volume or on the surface of the target producing surface muons.

5.1.3 Surface Muon Production

The phenomenon of surface muons arises from the decay of these stopped positive pions, through the process $\pi^+ \rightarrow \mu^+\nu_\mu$ near the surface of the target. This is a simple two body decay that results in isotropic production of mono-energetic, spin-polarized positive muons. The mono-energetic surface muon momentum is calculated from the two-body decay in the rest frame of the pion assuming zero neutrino mass, using the following equation:

$$E_\mu = \frac{m_\pi^2 + m_\mu^2}{2m_\pi} \tag{5.1}$$

where m_μ is the mass of the muon and m_π is the mass of the pion. The charged pion has zero spin, and in the rest frame of the decaying pion, the charged lepton and the neutrino are emitted in opposite directions to conserve linear momentum and with their spins equal and opposite to satisfy angular momentum conservation. This results in the neutrino having a left-handed helicity and chirality state and as a consequence the charged lepton must also have left-handed helicity, as shown in Figure 5.6. The reason for this lies in the electroweak interaction which is a chiral theory where parity is not conserved and as a consequence the weak gauge bosons

couple only to the left chirality states of particles and the right chirality states of antiparticles. This can be demonstrated by comparing the two dominant pion decay modes, $\pi^+ \rightarrow \mu^+\nu_\mu$ and $\pi^+ \rightarrow e^+\nu_e$. For the case of a relativistic positron being emitted, it will have only a small right handed chiral component, whereas in the case of a positive muon which is non-relativistic, it will carry a larger right-handed chiral component. The right-handed chiral component for a left-handed helicity state is proportional to $(m/E)^2$ and since the muon is more than 200 times heavier than the positron, the positron decay mode is strongly suppressed leading to a relative enhancement of muons to positrons from pion decay. The relative branching ratio for positrons compared to muons from pion decay is 1.23×10^{-5} [4].

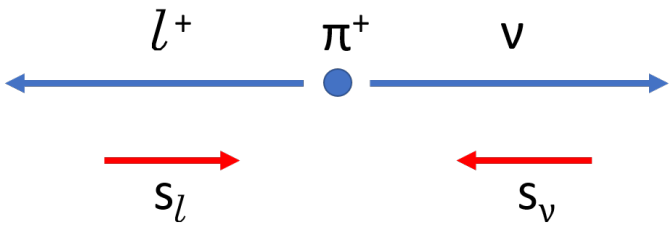

Figure 5.6: The helicity states of the neutrino and lepton emitted in charged pion decay. The pion has no spin and therefore to conserve angular momentum the neutrino and charged lepton spins must be equal and opposite. s_l and s_ν are the spin vectors for the emitted lepton and neutrino respectively.

6 Beamline Simulation

6.1 G4beamline

The G4beamline software [43] is a single-particle simulation program optimized for the design and evaluation of beam lines. It is based on the Geant4 toolkit, and can implement accurate and realistic simulations of particle transport in both EM fields and matter. This makes it particularly well suited for studies of design concepts for experiments involving muons, such as Mu3e. G4beamline includes a rich database of beamline elements and the program has been enhanced to handle a large class of beamline and detector systems. The G4Beamline software was used to implement all the elements of the beamline, starting from the Triplet II system. This was based on work done previously by members of the Mu3e collaboration [31]. This is shown in Figure 6.1. The beam in the simulation starts just before the first quadrupole magnet of TII. In the following sections the results were obtained using 10,000 muons. The first pixel layer and the target were simulated as part of this simulation. The stopping target in the simulation is a thin double cone made of 75μm Mylar in the front part and 85μm in the back part with a total length of 100 mm and a radius of 19 mm. The first pixel layer is simulated as a thin cylindrical layer of Silicon material detecting all particles passing through it. A Mylar vacuum window of 35μm thickness is placed at the end of the pipes inside the Mu3e solenoid just before the target and the first pixel layer. The x and y components of the beam momentum follow a Gaussian distribution whereas the z component is fixed at 28 MeV/c as shown in Figure 6.2 and dipole/quadrupole magnets are simulated according to the 2018 CMBL setup [44]. The exact current in each dipole & quadrupole magnet can be found in Appendix B.

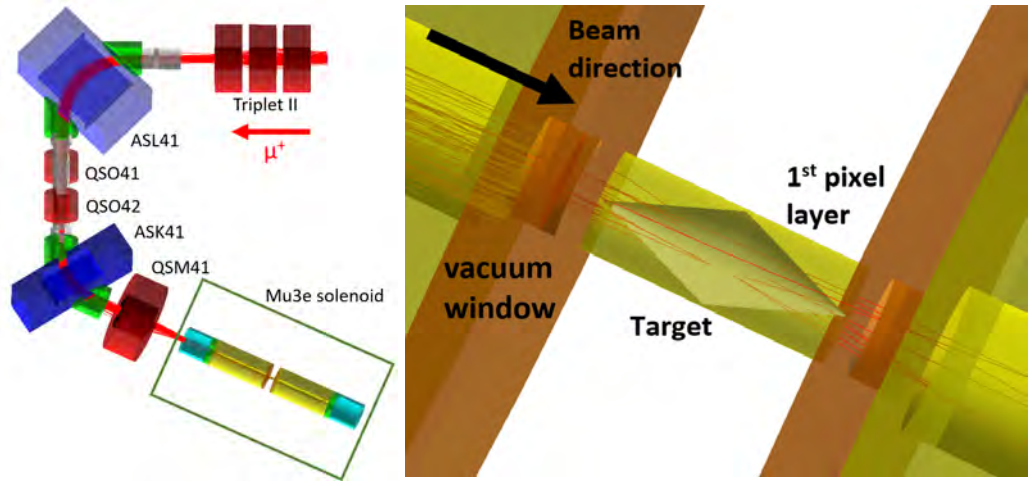

(a) All elements from Triplet II.

(b) The target and the first pixel layer.

Figure 6.1: Pictures from the G4Beamline simulation. The simulation starts from the Triplet II quadrupole system. The red lines indicate individual muons. The green box indicates the position of the Mu3e solenoid.

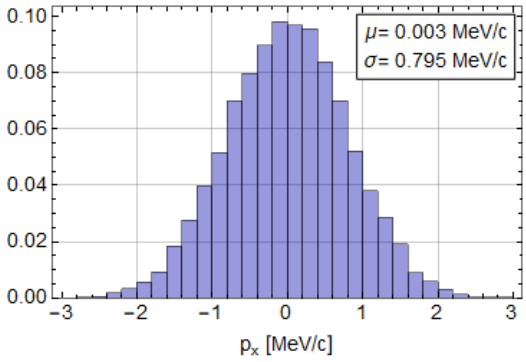

(a) x component.

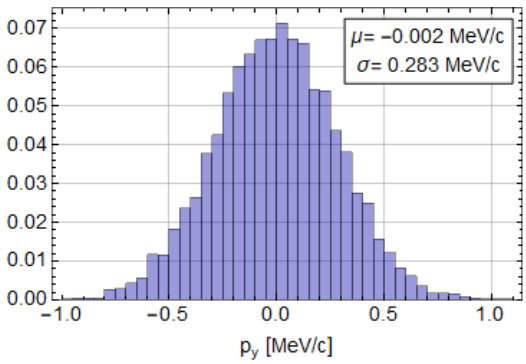

(b) y component.

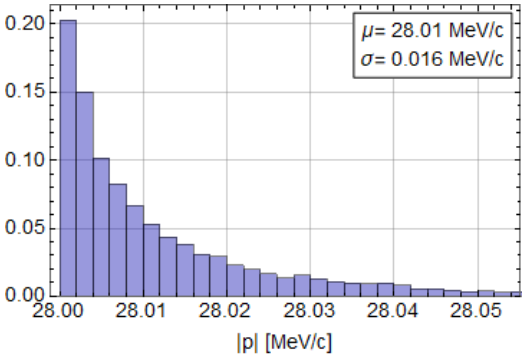

(c) total momentum.

Figure 6.2: Beam momentum profile at the beginning of the simulation. All y-axes are unit-normalised.

6.2 Moderator

There are four pipes inside the Mu3e solenoid positioned before the target. These are numbered from 1 to 4, as shown in Figure 6.3 and their exact dimensions are summarised in Table 6.1. A moderator is required to decrease the total beam momentum. This is a thin piece of Mylar sheet necessary for the muons to have low enough momentum so they can stop on the surface of the double-cone target. Without a moderator more than 99% of the muons would simply fly through the target. Mylar sheets of various thicknesses, ranged from 100μm to 800μm were simulated and studied. A very thin moderator will cause minimum scattering to the beam but at the same time most of the muons will fly through the target. A very thick moderator on the other hand will cause a great amount of scattering to the beam and also many muons will be absorbed. It is therefore necessary to find the optimal thickness of the moderator, which will maximise the number of muons stopping on the target, as shown in Figure 6.4. The optimal thickness of the moderator is around 600μm, where more than 95% of the muons that pass through all pipes stop on the target. The beam momentum is reduced almost by a factor of 2, going from 28 Mev/c down to 15 MeV/c. The vast majority of the remaining 5% of muons stop on the first pixel layer, and a tiny amount of them ($\ll$1%) goes through the target.

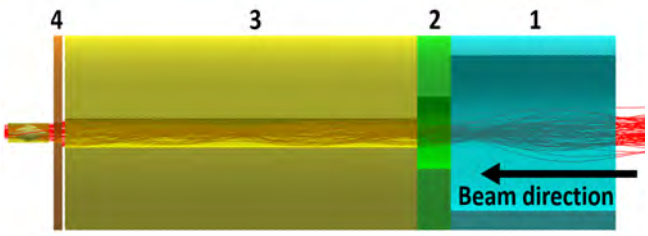

Figure 6.3: Picture of the simulation showing the pipes inside the Mu3e solenoid.

Pipe	1	2	3	4
Radius [mm]	160	74	30	20
Thickness [mm]	40	126	170	180
Length [mm]	397	81	848	21

Table 6.1: Dimensions of the pipes inside the Mu3e solenoid.

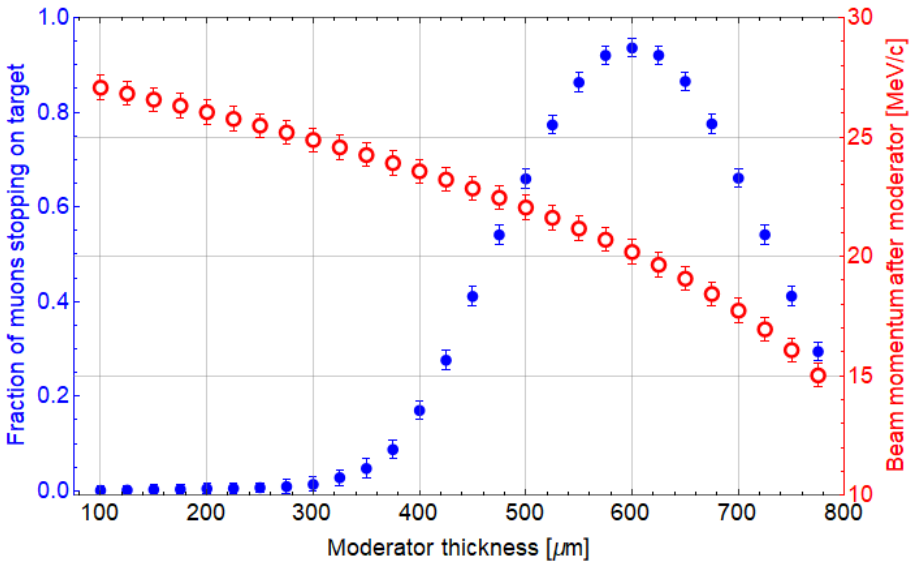

Figure 6.4: In blue, the number of muons stopped on target and in red, the mean momentum of the beam as a function of the thickness of the moderator.

For the rest of the simulation a moderator of thickness 600μm was used. The optimal position of the moderator is at a position where the mean radius of the beam is at minimum. This implies that any scattering due to the moderator will have a minimal effect in terms of the number of muons reaching the target. Figure 6.6a and Figure 6.6b show the mean radius and the spread of the beam along the x and y axes. The beam radius is minimum at a distance of around 50 cm before the centre of the target and this is the optimal position for the moderator. A picture from the simulation showing the moderator placed inside the pipes is shown in Figure 6.5.

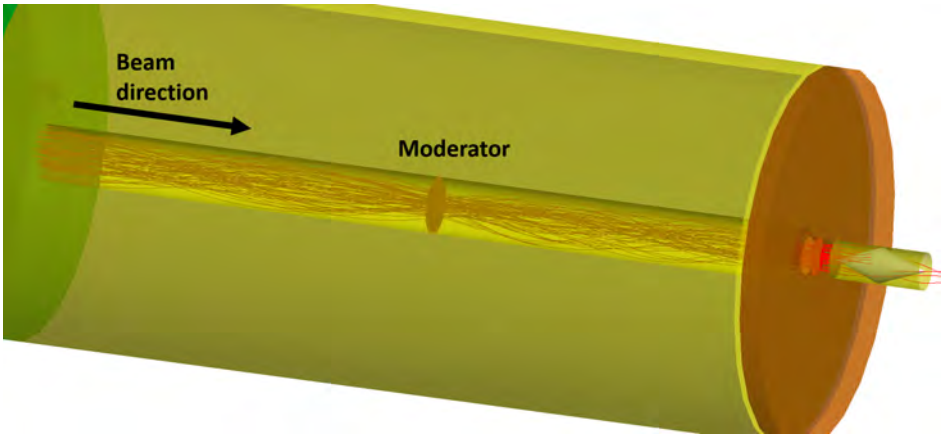

Figure 6.5: The moderator inside the 3rd pipe of the Mu3e solenoid.

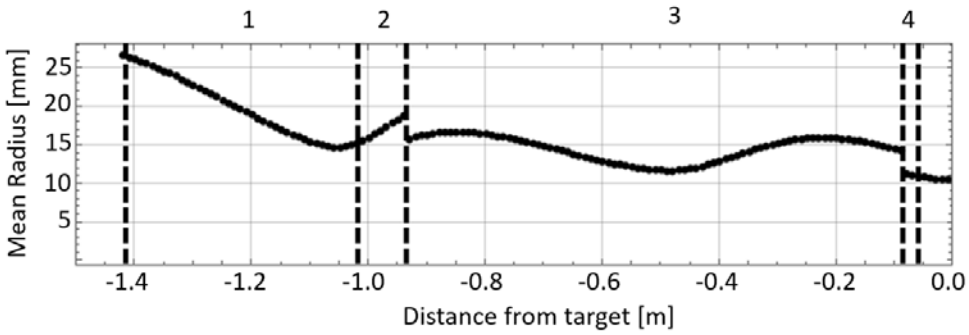

(a) mean radius of the beam.

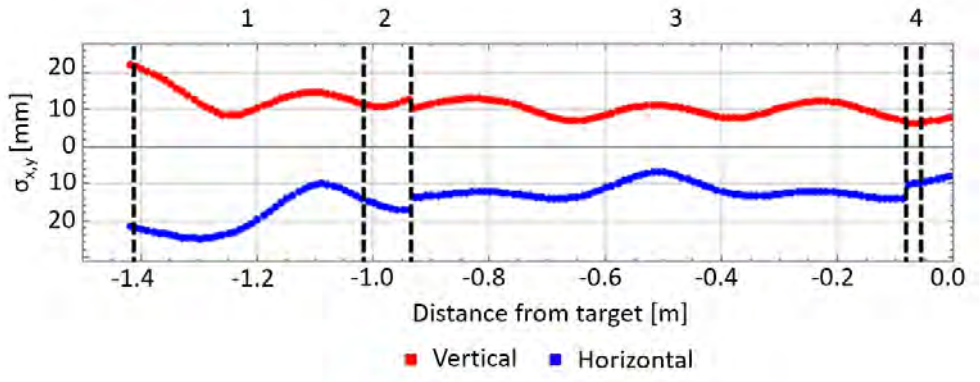

(b) horizontal and vertical beam profile.

Figure 6.6: Beam profile inside the Mu3e solenoid. The numbers above the plots indicate the number of the pipe. Beam direction is from left to right. All positions are relative to the centre of the target.

6.3 Collimator

A collimator is an object stopping a certain amount of the beam. In this case, the part of the beam that is of particular interest is the fraction of muons stopping on the first layer of the pixel tracker. The pixel tracker will be occupied by tens of decay electrons in each time frame (50 ns). In order to protect the pixels but also for better frame reconstruction it is important to minimise the number of muons stopping or going through the pixel detector. For this reason a collimator (or a system of multiple collimators) must be placed somewhere inside the pipes of the Mu3e solenoid at an optimal position where most of the muons stopping on the pixels are removed but at the same time most of the muons stopping on the target are kept. This of course makes the task very challenging. G4beamline allows us to separate the muons that

stop on the pixels from the ones that stop on the target, and their beam profile is shown in Figure 6.7. This can be useful when trying to find the optimal position for a collimator.

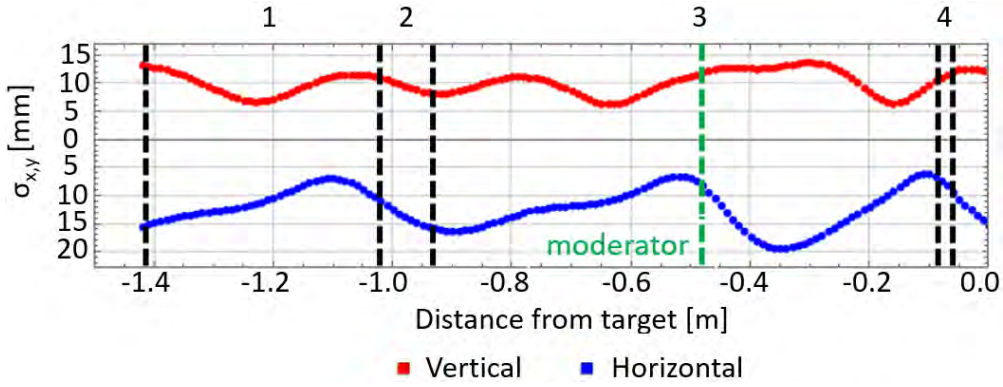

(a) Muons stopping on pixels.

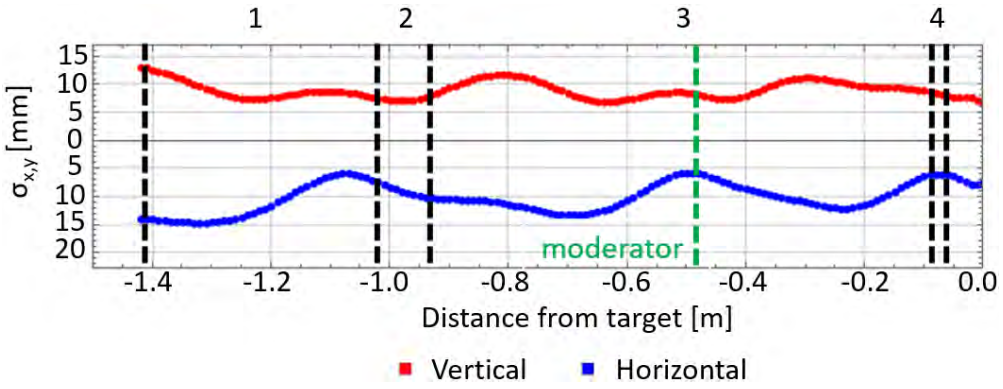

(b) Muons stopping on target.

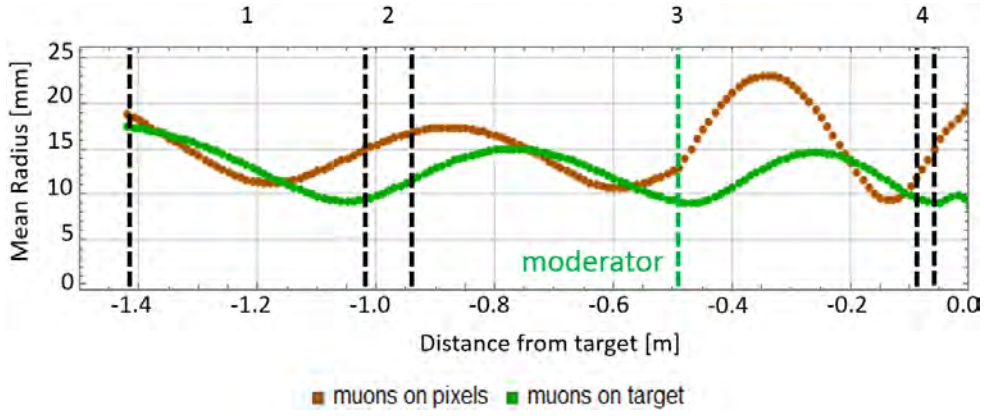

(c) Mean radius of the beam for muons stopping on target and on pixels.

Figure 6.7: Beam profile for muons stopping on target and on pixels. The numbers above the plots indicate the number of the pipe. Beam direction is from left to right. All positions are relative to the centre of the target.

In this simulation, all collimators studied have a ring shape of lead material. Previous studies within the Mu3e collaboration have shown that the thickness of a collimator should be at least 10 mm in order to also stop the electrons produced from the muon decay. An ideal position for one or more collimators would be the one where all muons stopping on the pixels are removed and at the same time all muons stopping on the target are kept. In reality of course this is not possible. In this simulation an one- and a two-collimator system were studied. In general it is better to remove unwanted muons as early as possible in the pipes before they approach the target. From Figure 6.7c, two potential positions for collimators can be identified, one collimator before the moderator at a distance of around 90 cm from the centre of the target and a second collimator just after the moderator at a distance of around 35 cm from the centre of the target. These are the positions where the mean radius of the beam consisting of muons stopping on the pixels is at a maximum value. A picture from the simulation showing the two collimators placed inside the pipes is shown in Figure 6.8. By increasing the radii of the two collimators, more muons will stop on the target but also more muons will stop on the first pixel layer too. The fraction of muons removed from the target and the pixels as a function of the radius of each collimator is shown in Figure 6.9. There are currently no upper limits set by the collaboration on the maximum amount of muons allowed to stop on the first pixel layer of the tracker. It must be noted that the second layer of the pixel tracker was also simulated, but no muons stop on it.

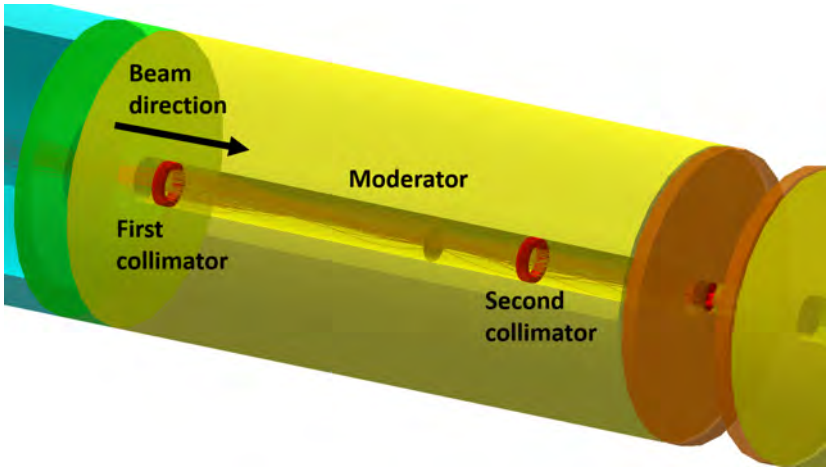

Figure 6.8: Picture from the simulation showing the positions and shapes of the two collimators.

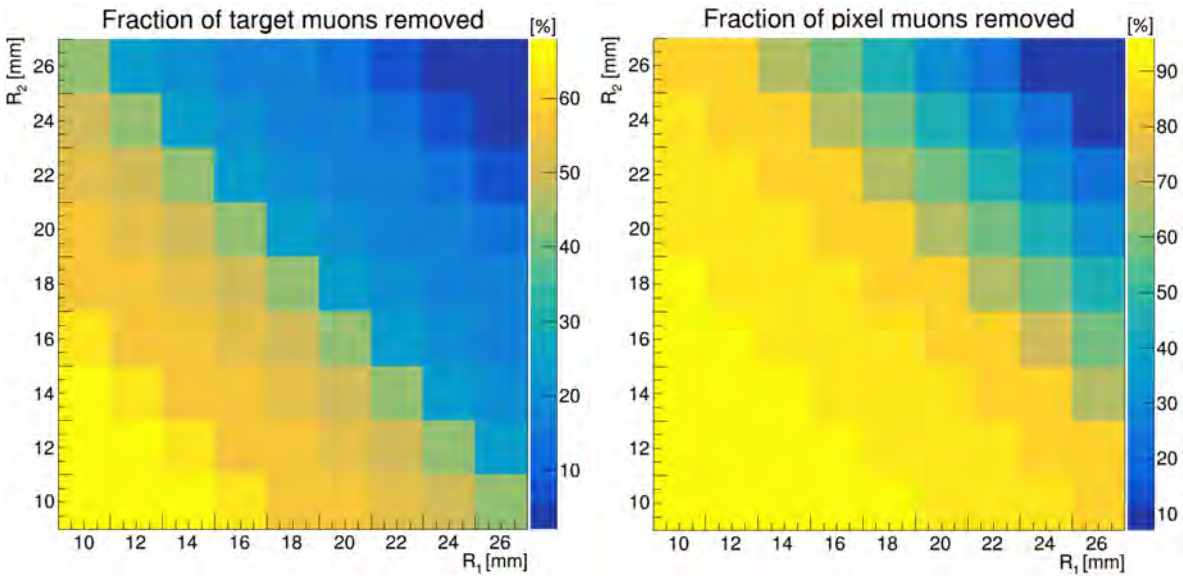

(a) (b)

Figure 6.9: Fraction of (a) muons stopping on target and (b) muons stopping on pixels removed by the two collimators as a function of their radii.

6.4 Momentum spread

The beam used in the previous sections has the z component of the momentum fixed at 28 MeV/c, making the beam somewhat unrealistic. One could apply a momentum spread directly at the beginning of the simulation, however the simulated beamline is not optimised for this kind of beam. A different approach was thus needed to address this problem. A more reasonable solution is to apply a Gaussian spread to the momentum of the beam at the beginning of the third pipe inside the Mu3e solenoid and compare some of the results with the old beam, where there is no momentum spread. The moderator is very sensitive to the beam momentum, meaning that its optimal thickness may vary when a beam with a momentum spread is used. This is the main problem with the old beam used in the simulation. A momentum spread was applied to the z component of the beam momentum with a mean of 27.8 MeV$/$c and a standard deviation of 0.86 MeV/c [31]. The momentum spread was generated using a simple python script, with the steps as shown in Figure 6.10. In order to achieve this, the beam parameters were read at the beginning of the third pipe and the unit momentum vector of each muon was calculated. Then a new p_z component from a random Gaussian distribution was assigned to each

muon. The p_x and p_y components were scaled accordingly, in order to keep the direction of each muon unchanged. The new beam was written to a text file and the simulation was then rerun starting from the beginning of the third pipe.

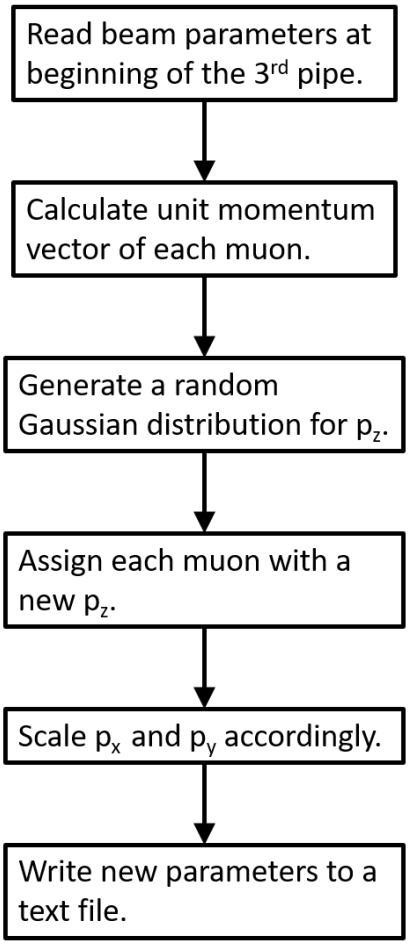

Figure 6.10: The logic behind the script that was used to generate the momentum spread.

The z component and the total momentum of the new beam form a Gaussian distribution, as shown in Figure 6.11, making the beam much more realistic. The moderator was kept at the same position at a distance of 0.49 m from the centre of the target. By varying its thickness, the results of the new beam were compared with the results of the old beam. This is shown in Figure 6.12. By using the new beam, the optimal thickness of the moderator, although shifted slightly to a larger value (650 μm), it is still very close to the result of the old beam (600 μm). In addition less muons stop on the target but this is expected due to the presence of muons with a higher total momentum, making it more difficult for them to stop on the target. This can be seen in Figure 6.12a. Having a moderator of thickness in the range between

100 μm to 500 μm, the amount of muons reaching the target is essentially identical for both kinds of beams, but they seem to diverge after that point. This is shown in Figure 6.12c.

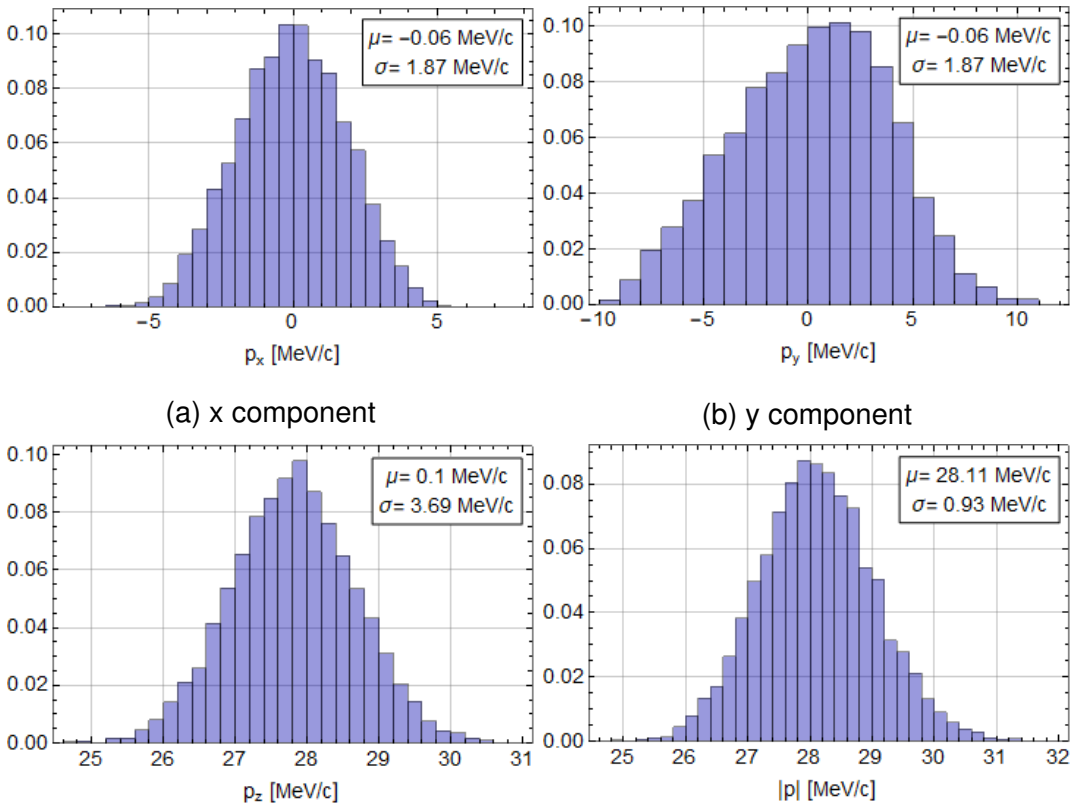

(a) x component

(b) y component

(c) z component

(d) Total momentum

Figure 6.11: Beam profile of the new beam which includes a spread on the z component of the beam momentum. All y-axes are unit-normalised.

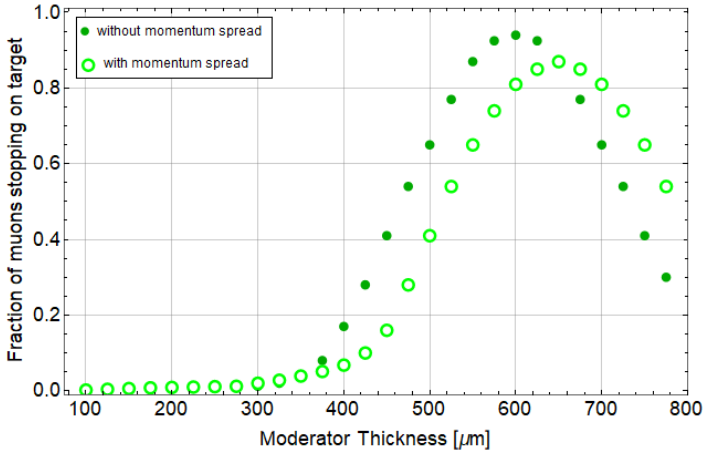

(a) Muons stopping on target.

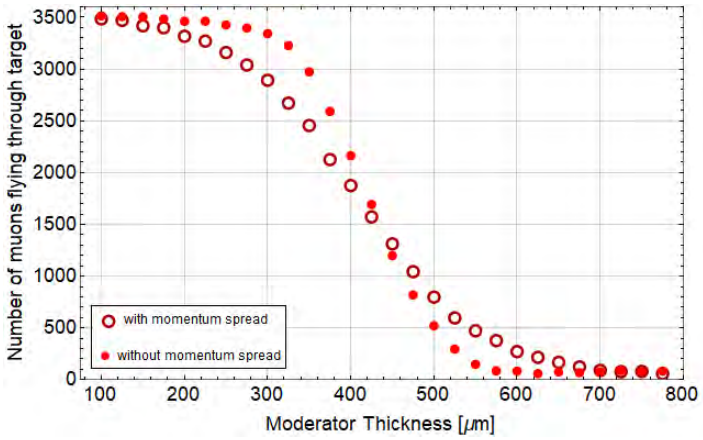

(b) Muons flying through the target.

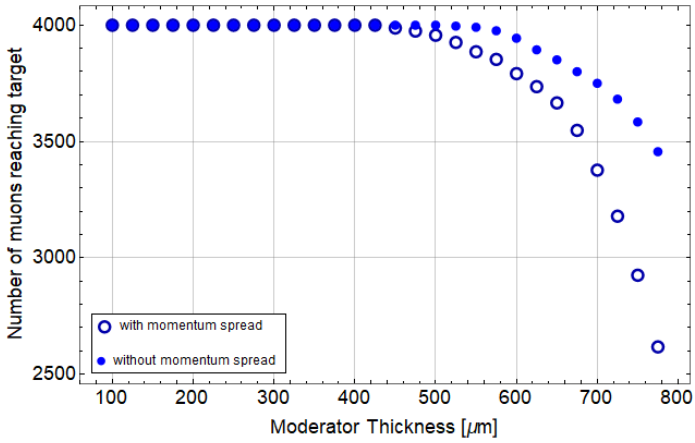

(c) Muons reaching the target.

Figure 6.12: Comparison between the results of the old and new beam as a function of the thickness of the moderator.

6.5 Summary

The thickness and the position of the moderator is crucial and must be such that the number of muons stopping on the target is at a maximum. The optimal thickness for the moderator is 600μm as at this thickness almost 95% of the muons that reach the target area actually stop on the target. At this thickness the beam momentum is reduced to 20 MeV$/$c. The optimal position for the moderator is at a distance of 50 cm before the centre of the target, as at this position the mean radius of the muon beam is at a minimum. A two system collimator can be used to remove part of the muons that land on the first pixel layer of the tracker and ring collimators of different sizes were studied. A large amount of the unwanted part of the muon beam can be removed but at the same time a certain amount of the muons that land on the target is also discarded. In chapter 7 an analysis of the beam measurements at three different positions of the full CMBL beamline is presented. This was also the very first time that the beam was measured at the centre of the Mu3e magnet.

7 | Beam Measurements

Beam measurements were carried out at three different positions inside the πE5 experimental area during May and June of 2021. This was the first time that the full beamline was used, which includes the Mu3e magnet. The goal was to fully characterize the beam and to estimate the available beam rate at different positions along the beamline. The positions are the following, as shown in Figure 7.1:

1. **Measurement 1:** At collimator position.
2. **Measurement 2:** At the injection point to the Mu3e experiment.
3. **Measurement 3:** At the centre of the Mu3e magnet (Mu3e target position).

Measurements 1&2 were performed using a detector that is used for the MEG experiment, known as the Pill. The Pill is simply a phototube coupled to a scintillator with a diameter of 2mm and it is covered with Tedlar and mounted in acrylic glass for stability, as shown in Figure 7.2a. It can be mounted on a scanner platform as shown in Figure 7.2b. Step motors in the horizontal and the vertical axis together with the rigid and robust construction allow for a positioning precision of <0.1 mm with the limiting accuracy determined by the alignment during the scanner setup procedure. The system is connected to a dedicated computer with a LabVIEW interface [45], allowing the scanner to be controlled remotely from the beamline control room. Oscilloscope screenshots in Figure 7.3 show the different signal signatures for beam positrons and surface muons obtained by adjusting the magnetic field of the separator (SEP41). This chapter focuses only on the muon beam. For measurement 3 (inside the magnet), the Pill scanner could not be used as it doesn't fit inside the magnet and also the Pill detector itself consists of magnetic materials. For these reasons, a brand new scanner was developed using two non-magnetic piezoelectric motors with optical encoders and an Avalanche Photodiode (APD) detector,

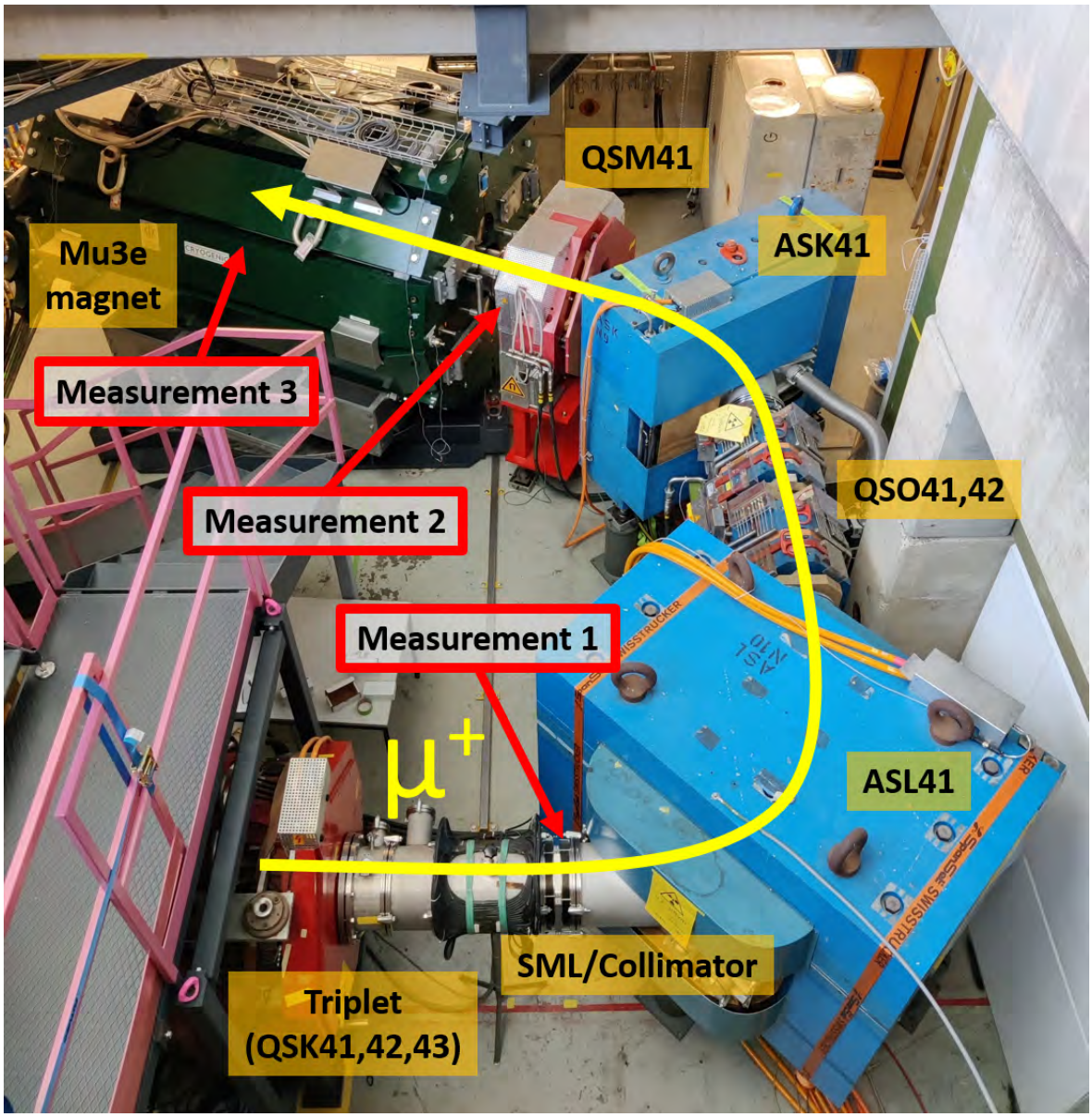

Figure 7.1: Full CMBL setup for the May/June 2021 test beam. The measurements were carried out at 3 different positions as shown in picture. All magnets beginning with a letter Q are quadrupoles and magnets beginning with a letter A are dipoles. The separator (SEP41) is located beneath the stairs, thus it is not shown here.

as shown in Figure 7.4a. The APD scanner is attached onto an aluminum beam mounted on the two side rails at the inner side of the Mu3e magnet, as shown in Figure 7.4b. The APD detector is a semiconductor photodiode detector which converts light into electricity using the photoelectric effect and it was calibrated against the Pill. It is mounted at the top of the y-axis motor and it can move freely in the x-y plane. The optical encoders provide information on the position of the motor

by emitting light through a plastic marked strip with a precision less than 1mm. A Graphical User Interface (GUI) was also developed that allows the user to control the APD in a similar manner as with the Pill scanner. A screenshot of the GUI is shown in Figure 7.5.

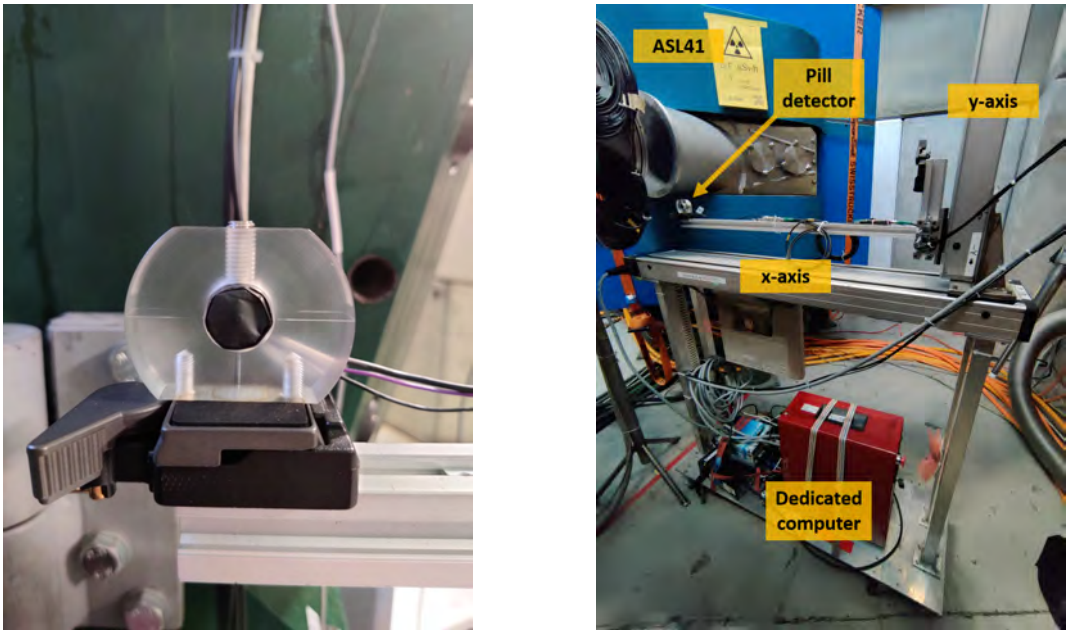

(a) Pill detector.

(b) Pill scanner.

Figure 7.2: The Pill detector and the complete scanner system that was used for measurements 1&2.

The πE5 channel has to be optimised for maximizing the muon rate delivered to the centre of the Mu3e magnet system. For a good background suppression, a Wien-filter separator is used in conjunction with a lead collimator. SEP41 is a beamline element generating perpendicular electric and magnetic fields that deflect particles based on their velocity. For typical beamline elements consisting solely of a magnetic field, the charged particles will take a circular path within the uniform field region with a radius of curvature proportional to the momentum and inversely proportional to the magnetic field, given by the following equation:

$$r = \frac{mv}{Bq} \tag{7.1}$$

where r is the radius of curvature, m is the mass of the particle, v is the velocity of the particle, q is the electric charge of the particle and B is the magnetic field. The separator generates electric and magnetic fields such that the total force acting

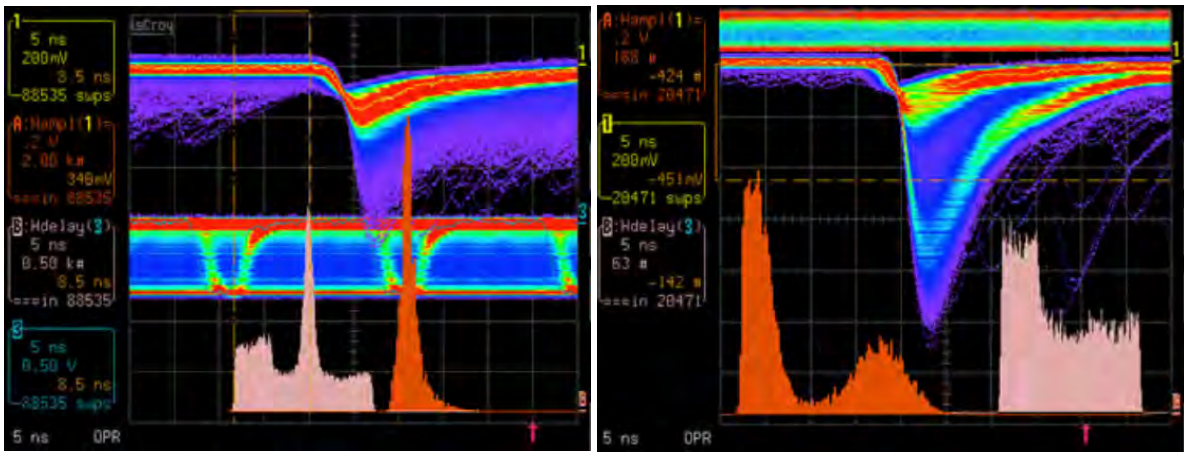

(a) Separator set to e^+

(b) Separator set to μ^+.

Figure 7.3: Oscilloscope signals of muons and positrons. In the muon case two distributions are present, the higher Gaussian distribution corresponds to the muons whereas the lower distribution is mainly due to Michel positrons.

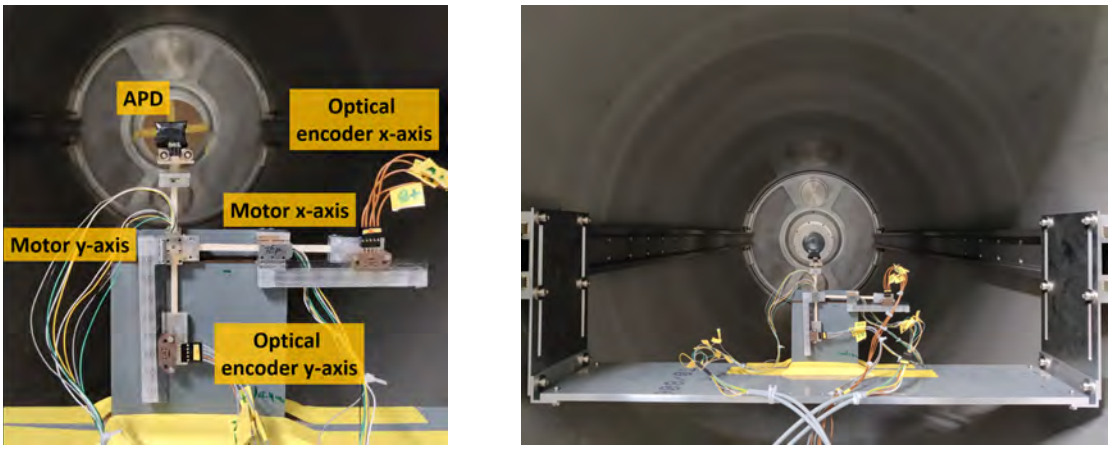

(a) APD scanner.

(b) APD scanner on the aluminum beam.

Figure 7.4: The APD scanner, that was used for measurement 3.

on the particle is zero for a given velocity. The Lorentz force acting on a particle travelling through a magnetic and electric field is given by:

$$\vec{F} = q(\vec{E} + \vec{v} \times \vec{B}) \tag{7.2}$$

The total force on the particle is zero when the force from the electric field is equal and opposite to the force due to the magnetic field. A diagram with the proper field configuration for a positively charged particle and the various paths it will take based on velocity is shown in Figure 7.6.

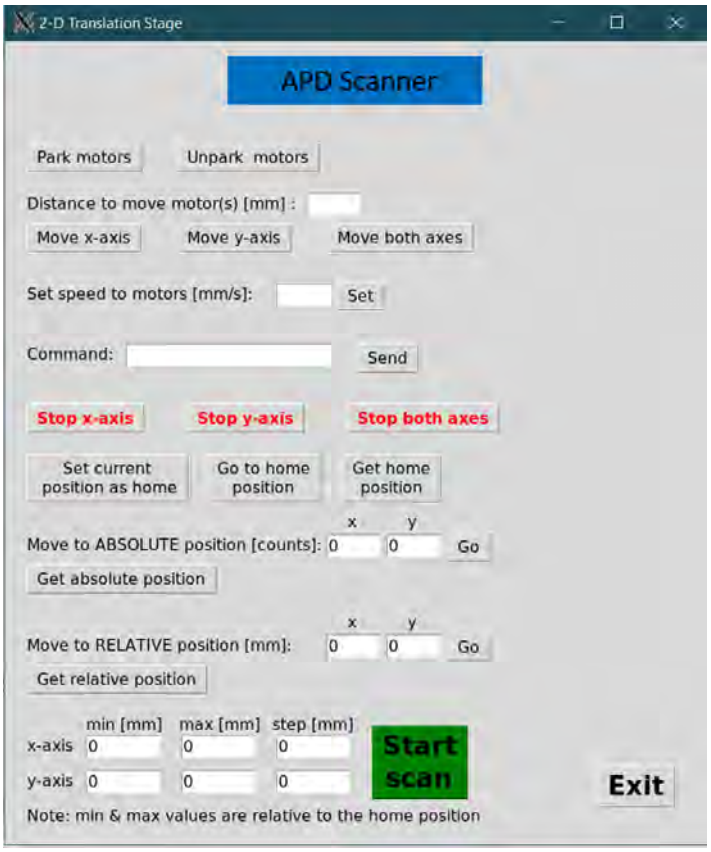

Figure 7.5: Graphical User Interface of the APD scanner.

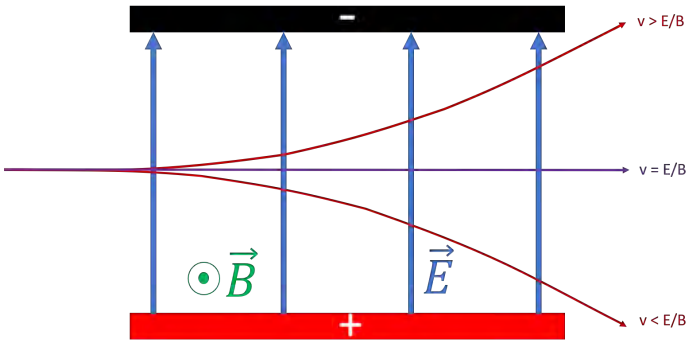

Figure 7.6: Working principle of the separator.

Therefore the particle velocity for which the total force acting on it is zero is given by the following equation:

$$v_z = \frac{E_y}{B_y} \tag{7.3}$$

The standard SEP41 is operated with the top plate on 180 kV negative potential and the bottom plate on ground, although different potentials can be explored. The

actual particle separation happens at the downstream 120mm collimator system, following the triplet of quadrupole magnets (QSK41,42,43), where the unwanted beam component is stopped. Before the beam measurements, the first step is to optimise the beam and to do this we use the OPTIMA program [31]. This is a software package where beamline elements can be tuned automatically to maximise the beam rate. During this step, the Pill detector is placed at the required position along the beam line and the elements can be automatically tuned by choosing the best current configuration for each beamline element that results in the maximum beam rate. For all three measurements, the absolute muon rate can be determined by doing a cross scan. This is a 2D scan of the beam spot using the Pill or APD detector. This method scans in the form of a cross and the muon rate is estimated using one dimensional scans of the horizontal and vertical axes of the beam profile. A Gaussian distribution is then fitted to the data to obtain the horizontal and vertical beam widths independently. The beam optimization is an iterative procedure technique and special care must be taken when changing the current of dipole magnets due to hysteresis, in order to ensure reproducible results.

7.1 Results from measurements

For all three measurements the Mu3e magnet was switched on, generating a field of 1T at the centre. High precision measurements are not necessary due to the fact that only the order of magnitude of each measurement is relevant. The first measurement was carried out in the air gap between the beam pipe vacuum window after the collimator and the ASL41 dipole magnet entrance. For each measurement the beam pipe is kept under vacuum using a Mylar window of 100μm thickness. The Pill detector was aligned with the centre of the beamline using a laser scanner, as shown in Figure 7.7. For measurements 1 & 2 the Pill scanner took measurements on both axes in the range between -60 mm to +60 mm from the central position with a step-size of 5 mm and a rest time of 1 s at each point. The muon beam cross scans at the beam center are shown in Figure 7.8. The muon beam as measured at the collimator has an Gaussian shape with a relatively large spread. From Figure 7.8a and Figure 7.8b, the muon rate at the collimator position was calculated to be $R_{\mu^+} = (1.99 \pm 0.20) \times 10^8 \mu^+/s$.

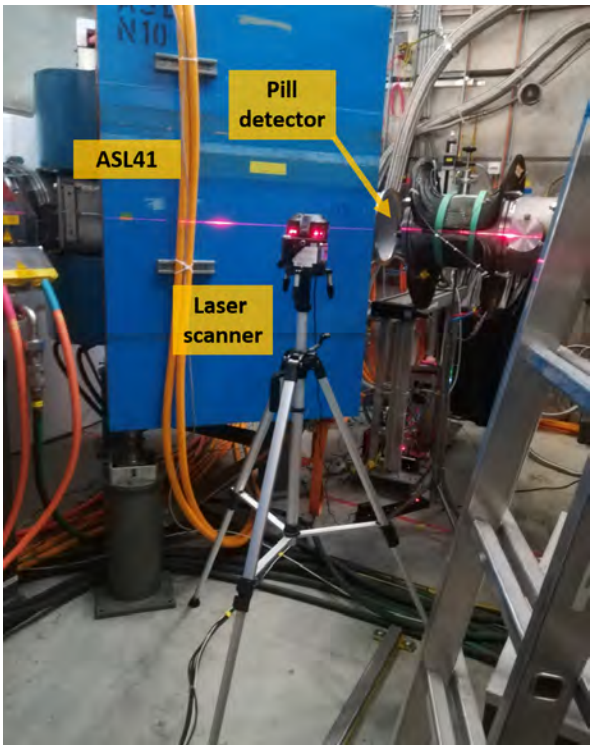

Figure 7.7: Alignment of the Pill detector for beam measurement at the collimator.

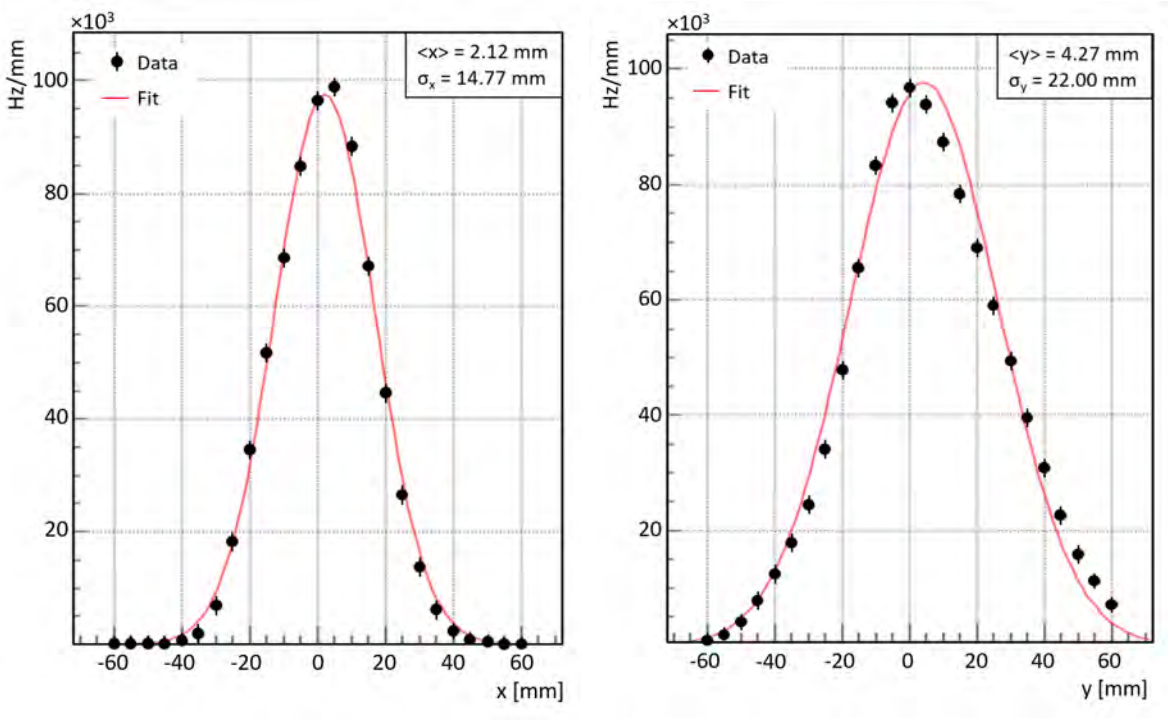

(a) Horizontal beam profile.

(b) Vertical beam profile.

Figure 7.8: Muon beam measured at the collimator system showing the horizontal and vertical beam profile measured with the Pill scanner.

For the second measurement, the Pill scanner was placed in the air gap between the beam pipe vacuum window after QSM41 quadrupole magnet and the entrance to the Mu3e magnet system. This measurement is of great importance as this is essentially the maximum muon rate available for the Mu3e experiment. As with measurement 1, the Pill was aligned with the centre of the beamline using a laser scanner, as shown in Figure 7.9. The muon beam measured at the Mu3e injection has an Gaussian shape, as shown in Figure 7.10, with a similar spread to measurement 1. The muon rate at the entrance to the Mu3e magnet system was calculated to be $R_{\mu+} = (1.10 \pm 0.11) \times 10^8 \mu^+/s$. This means that the muon transmission efficiency from the collimator to the injection point to Mu3e experiment is $\approx 57\%$. The rest of the muon beam is lost inside the pipes.

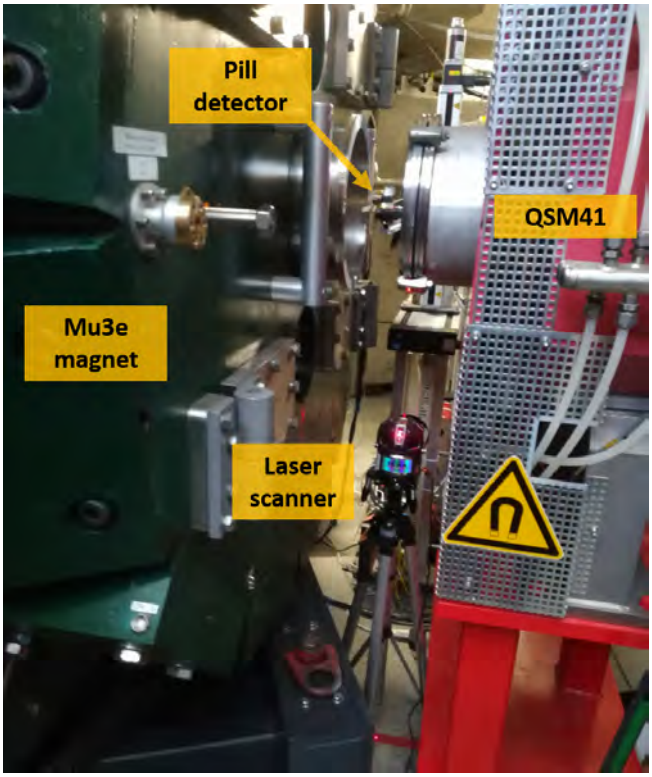

Figure 7.9: Alignment of the Pill detector for beam measurement at the entrance of Mu3e magnet.

For the measurement at the centre of the Mu3e magnet, an aluminum dummy beam pipe was inserted on the inside of the Mu3e magnet. The dummy pipe consists of two aluminum collimators of thickness 22 mm and 40 mm, and a Mylar sheet of 300 μm thickness which acts as the moderator in order to reduce the beam momentum. Although previous simulation studies showed that the optimal thickness

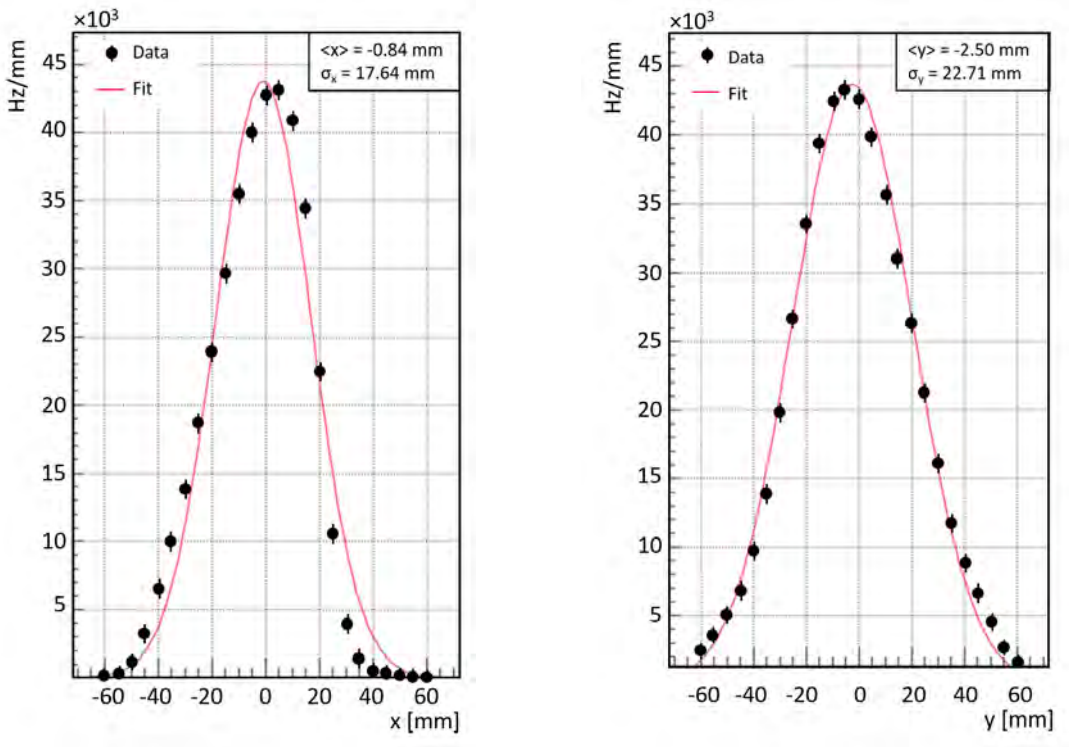

(a) Horizontal beam profile.

(b) Vertical beam profile.

Figure 7.10: Muon beam measured at injection to Mu3e magnet system showing the horizontal and vertical beam profile measured with the Pill scanner.

for the moderator is 600 μm (see section 6.2), for technical reasons and to also save time, an existing 300 μm Mylar sheet was used. The dimensions of the pipe and the components inside it are shown in Figure 7.11. For the alignment of the APD detector inside the magnet, the same technique with the laser scanner was used as before. This is shown in Figure 7.12. It must be noted that due to technical difficulties with the APD scanner, different axes ranges were used for the x- and y-axis. On the x-axis, measurements were taken in the range between -27.5 mm to 15 mm from the central position with a step-size of 2.5 mm. On the other hand on the y-axis, measurements were taken in the range between -22.5 mm to 20 mm from the central position with a step-size of 2.5 mm. The muon beam measured at the centre of the Mu3e magnet is shown in Figure 7.13, with a significant smaller spread than the previous measurements. The muon rate at the centre of the magnet was calculated to be $R_{\mu^+} = (1.55 \pm 0.16) \times 10^7 \mu^+/s$, which means that the muon transmission efficiency from the injection point to the centre of the magnet is $\approx 14\%$. This is expected due to the size of the dummy pipe and also the size

of the two aluminum collimators. At the same time, it is important to note that the moderator introduces some scattering to the beam, resulting in the loss of a small amount of the beam. The first collimator is fixed in position but the second one can be removed easily. As a final measurement the second collimator was removed and another cross scan was performed to determine the change in the beam rate. This is shown in Figure 7.14. By simply removing the second collimator the beam rate increases almost by a factor of 3, to $R_{\mu^+} = (4.36 \pm 0.44) \times 10^7 \mu^+/s$. In the future both collimators and the moderator can be studied independently to determine their effect on the beam rate.

The πE5 channel contains two slit systems FSH41 and FS42 that restrict the beam in horizontal and the vertical axis respectively. These are located before the beam enters the experimental area shown in Figure 5.1 so these are not visible in the figure. Usually the FSH41 horizontal slit system is used for regulating the beam intensity and momentum-byte selection. By adjusting the slit aperture the beam rate and the momentum spread of the beam can be regulated according to the requirements. During typical operations both slits are at maximum opening to allow for maximum rate transmission. A measure of the influence of the horizontal slit opening at FSH41 on the beam rate, a so-called slit curve was measured by opening the FSH41 slit apertures symmetrically while measuring the muon beam rate at the centre of the magnet (on centreline). The corresponding slit curve is shown in Figure 7.15. The beam rate remains essentially at the maximum available value until the slit opening becomes less than 80 mm wide.

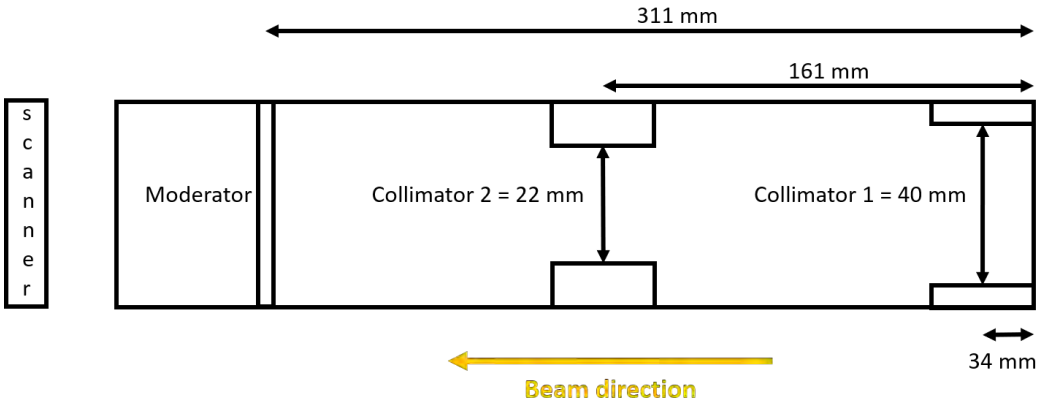

Figure 7.11: Dummy beam pipe used for the beam measurement at the centre of the Mu3e magnet system. Figure Not to scale.

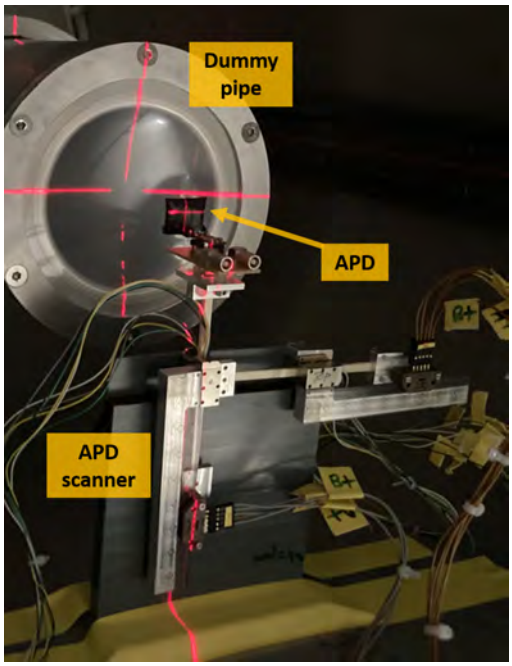

Figure 7.12: Alignment of the APD detector for the beam measurement at the centre of the Mu3e magnet system.

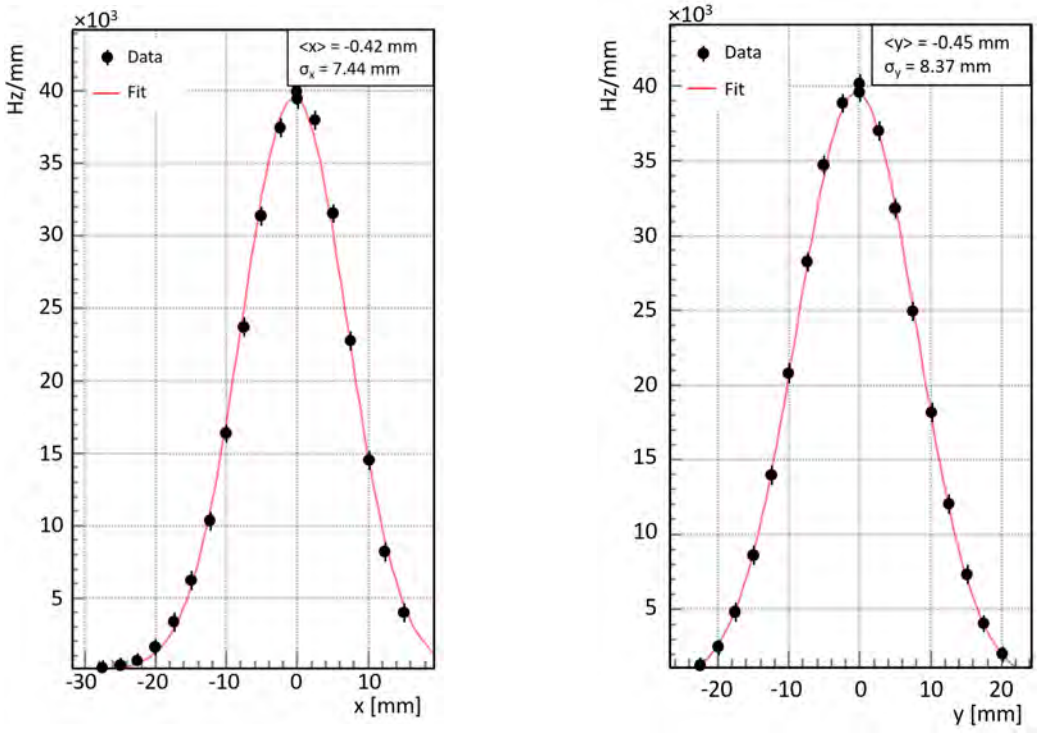

(a) Horizontal beam profile.

(b) Vertical beam profile.

Figure 7.13: Muon beam measured at the centre of the Mu3e magnet system using the new APD scanner.

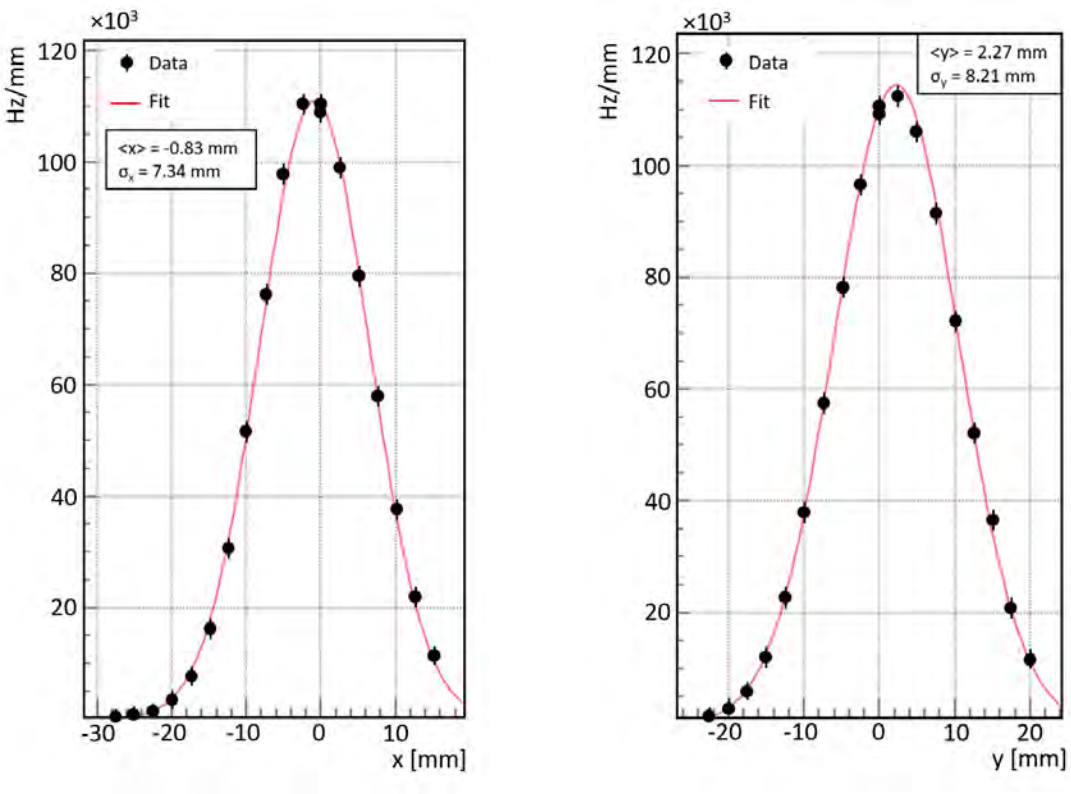

(a) Horizontal beam profile.

(b) Vertical beam profile.

Figure 7.14: Muon beam measured at the centre of the Mu3e magnet system using the new APD scanner without the 22mm aluminum collimator inside the dummy pipe.

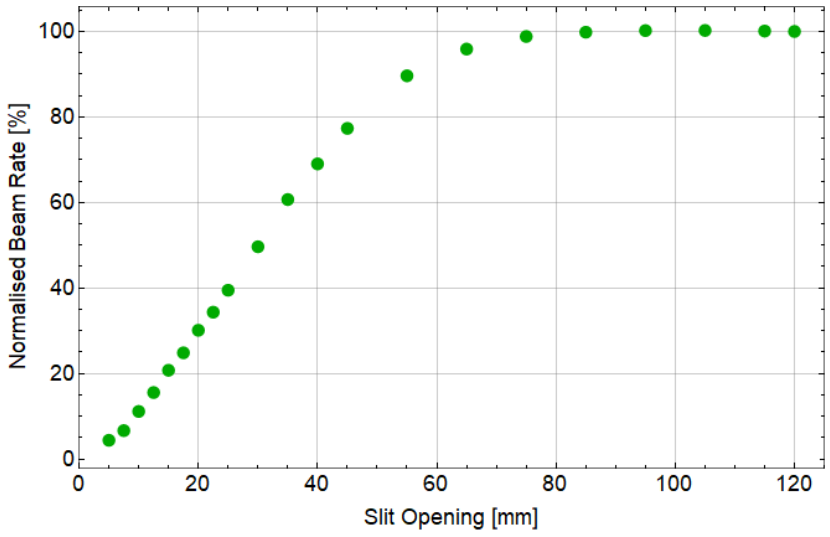

Figure 7.15: FSH41 slit scan. The beam rate is measured at the centre of the Mu3e magnet.

7.2 Summary

Baring in mind the fact that this was the first ever attempt to measure the beam using the full beamline that also includes the Mu3e magnet, this is considered as a very successful campaign. This is the first time that the beam goes inside the Mu3e magnet and more than $10^7 \mu^+/s$ was shown to be delivered at the centre of the magnet. This number can be improved in the near future by optimising the position of the collimators and the moderator inside the dummy pipe. From previous beamline simulations [31] the expected rate was calculated to be around $6 \times 10^7 \mu^+/s$ and the expected spread of the beam at the centre of the magnet was 7.5 mm and 8.7 mm for the x and y axis respectively. All these values are very close to the measured ones. The new APD scanner performed really well but there is always room for improvement especially with the mechanics, as it can be used again in the near future. Results are summarised in Table 7.1. The results essentially bring the Mu3e experiment one step closer to becoming a reality. For consistency checks, the beamline simulation was re-run using a moderator of 300μm thickness. The resulting simulated beam spread at the centre of the magnet is 7.42 mm and 8.31 mm for the x and y-axis respectively, which are comparable to the measured values.

Measurement	Rate [μ^+/s]
Position 1	(1.99 $\pm$ 0.20) $\times$ 10^8
Position 2	(1.10 $\pm$ 0.11) $\times$ 10^8
Position 3	(1.55 $\pm$ 0.16) $\times$ 10^7
Position 3 (2nd collimator removed)	(4.36 $\pm$ 0.44) $\times$ 10^7

Table 7.1: Summary of the muon beam rates achieved at the three locations inside the πE5 experimental area.

Part IV

Mu3e Software

8 | Multiple Scattering Tracking

Tracks in Mu3e are reconstructed from hit positions in the pixel detector and matched with additional timing information from the two timing detector systems. Due to the fact that decay particles are of low energy (<$m_\mu/2$ MeV/c), they undergo multiple scattering (MS) as they pass through the pixel layers of the tracker. With a fine-grained pixel detector, we are in a regime where scattering effects dominate over the sensor resolution, as shown in Figure 8.1, which means that MS is the main uncertainty for the track fitting. To account for this, a three-dimensional triplet fit is implemented for the track reconstruction [46].

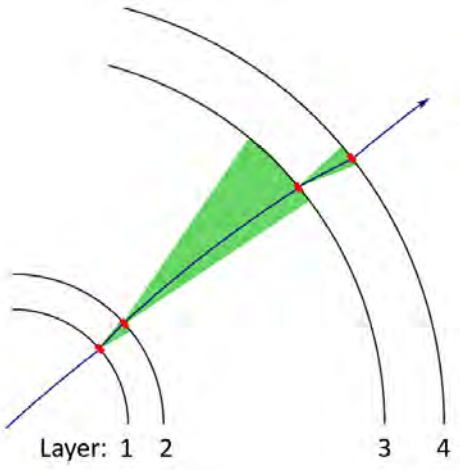

Figure 8.1: Tracking in a MS dominated regime. The particle trajectory is shown in blue and the pixel size in red. Due to MS the particle can travel anywhere in the green region. Diagram not to scale [28].

A **triplet** is simply a collection of three pixel hits, each being on a different pixel layer. The triplet fit method uses three hits x_0, x_1, x_2 and assumes multiple scattering at the middle hit, as shown in Figure 8.2. The scattering angles are denoted by Φ_{MS} and Θ_{MS}, the transverse track radii before and after the scattering process

are given by r_1 and r_2 and the respective arc lengths are denoted by s_1 and s_2. The helical trajectories through points x_0, x_1 and x_1, x_2, respectively, are described by the bending angles Φ_i, with distances d_i and azimuthal angles ϕ_i between points in the transverse plane. In the longitudinal plane, z_i are the distances between points along the field axis and θ_i are the elevation angles.

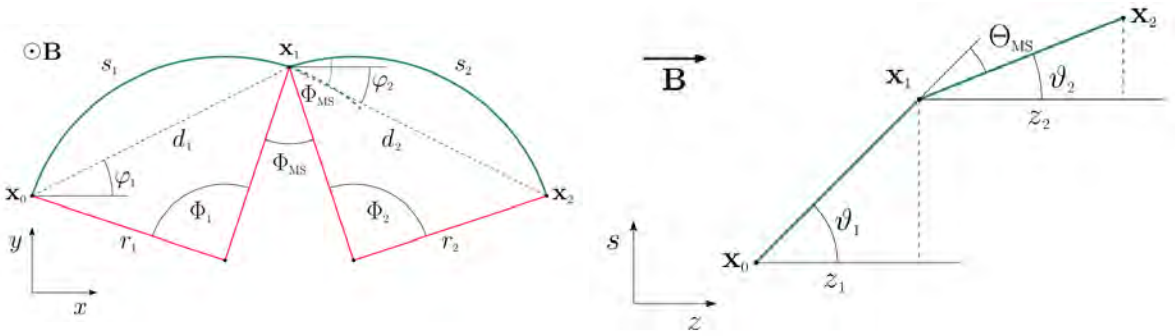

(a) Transverse view.

(b) Longitudinal view.

Figure 8.2: Triplet of hits x_0, x_1, x_2 [28].

In order to describe the helical trajectory of a charged particle inside a homogeneous magnetic field through three points, the following are required:

1. A starting point.
2. An initial direction.
3. The curvature.
4. The distance between the points.

Considering multiple scattering theory, the scattering angle is also needed as an additional parameter to include scattering at the middle hit x_1. In total, the three points provide enough parameters to describe the triplet. Using the hit positions of an initial triplet of hits, a helical trajectory with multiple Coulomb scattering at the middle detector layer is reconstructed. The variances of the two scattering angles Φ_{MS} and Θ_{MS} are then given by $\sigma^2_\phi = \sigma^2_{MS}/\sin^2\theta$ and $\sigma^2_\theta = \sigma^2_{MS}$, where θ is the polar angle of the track direction. The fit is then carried out by finding a 3D bending radius R_{3D} that minimises the following χ^2 function:

$$\chi^2(R_{3D}) = \frac{\Phi^2_{MS}(R_{3D})}{\sigma^2_\Phi} + \frac{\Theta^2_{MS}(R_{3D})}{\sigma^2_\Theta} \tag{8.1}$$

Assuming small scattering angles, which is justified for weak multiple scattering effects, the dependence of the scattering uncertainty σ_{MS} on the particle momentum can be neglected. The equation $d\sigma/dR = 0$ has to be solved to find the radius R that minimizes the scattering angles for a triplet. The solution does not depend on the scattering uncertainty anymore, so uncertainties for the track parameters can be calculated and easily propagated after fitting.

$$\Phi_{MS}(R_{3D})\sin^2\theta\frac{d\Phi_{MS}(R_{3D})}{dR} + \Theta_{MS}(R_{3D})\frac{d\Theta_{MS}(R_{3D})}{dR} = 0 \tag{8.2}$$

To use the hit information of an additional layer to the track, another triplet is constructed using the two outer hits from the first triplet and a hit from the next layer, as shown in Figure 8.3. Scattering in different layers is independent, therefore a global χ^2 function can be expressed as a sum:

$$\chi^2_{global} = \sum \chi^2_{triplet} \tag{8.3}$$

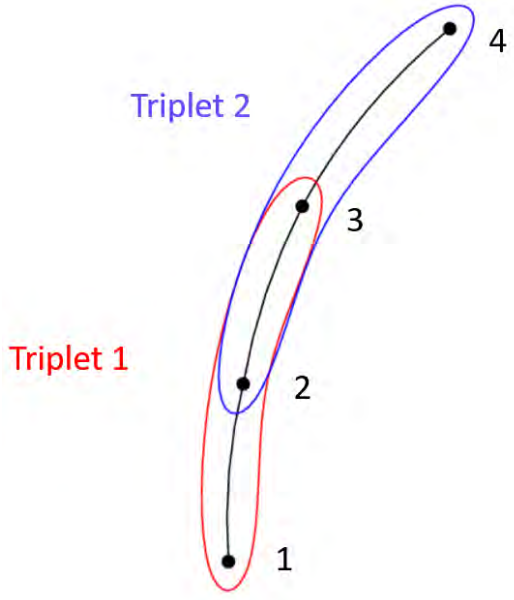

Figure 8.3: Two triplets combined to make a track.

Out of all reconstructed tracks within a reconstruction time frame (50 ns), signal candidates are chosen and tested for a common vertex. Signal candidates consist of three tracks, two positively charged and one with negative electrical charge. The curvature in the magnetic field determines the electric charge of the particle. A potential common vertex position $\vec{v}$ is estimated by the minimization of the scattering angles at the first tracking layer given the reconstructed track momentum from the track finding algorithm described above. The scattering angle minimization utilises the following χ^2function:

$$\chi^2(\vec{v})_{vertex} = \sum_{i=1}^{tracks} \frac{\Phi^2_{MS,i}(\vec{v})}{\sigma^2_{\phi,i}} + \frac{\Theta^2_{MS,i}(\vec{v})}{\sigma^2_{\theta,i}} \tag{8.4}$$

Table 8.1 lists the default cuts that a signal candidate must fulfil. Depending on the track candidate type, potentially one or two fibre detector clusters are assigned. The track candidates are grouped in three classes depending on the number of pixel tracking layers containing hits, as illustrated in Figure 8.4.

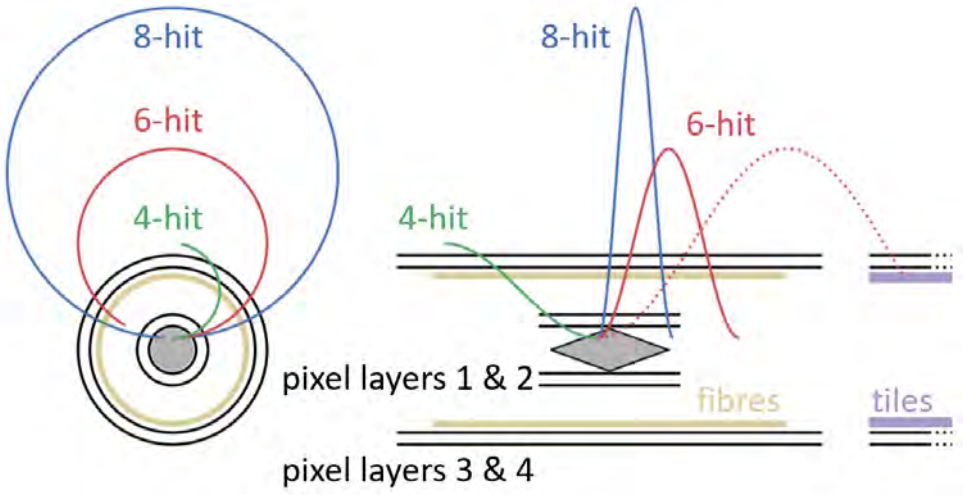

Figure 8.4: Track candidate classification depending on the number of pixel tracking layers containing hits.

1. **Short 4-hit (S4) tracks:** All track candidates need to pass at least all four tracking layers once. Track candidates which are neither linked to another re-curling 4-hit track candidate nor to recurling hit candidates in the outer detector barrels are in this category.

2. **Long 6-hit (L6) tracks:** This category consists of 4-hit track candidates which are linked to two hits in the outer pixel layers. They are predominantly linked to hits in the outer detector barrels where the particles are stopped in the scintillating tile detector or the support structure, for example the beam pipe.

3. **Outer Long 8-hit (L8o) tracks:** This category consists of two linked 4-hit tracks corresponding to recurling track candidates in the central detector barrel.

Variable	Value
χ^2_{vertex}	< 35
$\lvert\sum \vec{p}_i\rvert$	< 10 MeV/c
Distance to target	< 1 mm
Number of crossed layers	≥ 6

Table 8.1: Cuts applied to signal candidates. There is currently no default timing cut.

The reconstruction algorithm has to efficiently identify the tracks of particles from muon decays, while dealing effectively with the combinatorial background to keep the rate of incorrectly reconstructed tracks to an acceptable level. The main challenges of reconstruction are the high event rate and resulting occupancy, and the curvature of trajectories of low momentum particles in the magnetic field. Decay particles can make several turns inside the central station of the pixel tracker and hit combinations can span distances of more than half a meter with hits on opposite sides of the detector. The detector readout is triggerless, so all muon decays have to be fully reconstructed in the filter farm. This inevitably sets high demands on the speed of the online track reconstruction algorithm. Due to the acceptance geometry of the detector, only triplets with a transverse radius between 30 mm and 250 mm are formed. Then a cut on the track χ^2 value is applied for the first triplet at $\chi^2 = 100$. This step reduces the number of falsely reconstructed triplets by about a factor of 3. An example of an S4 track using simulation data from a background sample of events is shown in Figure 8.5. For the case of L6 and L8o tracks, only those with $\chi^2 < 48$ are saved. These type of tracks can greatly improve the

momentum resolution due to the large bending in the magnetic field. The Mu3e detector is particularly designed for measuring L6 and L8o tracks, as only these yield the excellent momentum resolution required in the experiment (<0.5 MeV/c). Tracks with more than 4 hits have a much larger lever arm for momentum measurement and thus provide a much enhanced momentum precision, as shown in Figure 8.6 for the case of S4 and L6 tracks. An example of an L6 and L8o track is shown in Figure 8.7 and Figure 8.8 respectively.

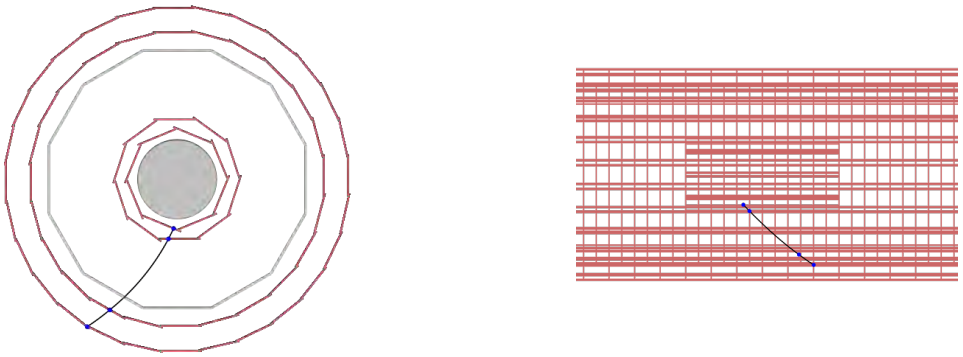

(a) Transverse view.

(b) Longitudinal view.

Figure 8.5: An example of an S4 track.

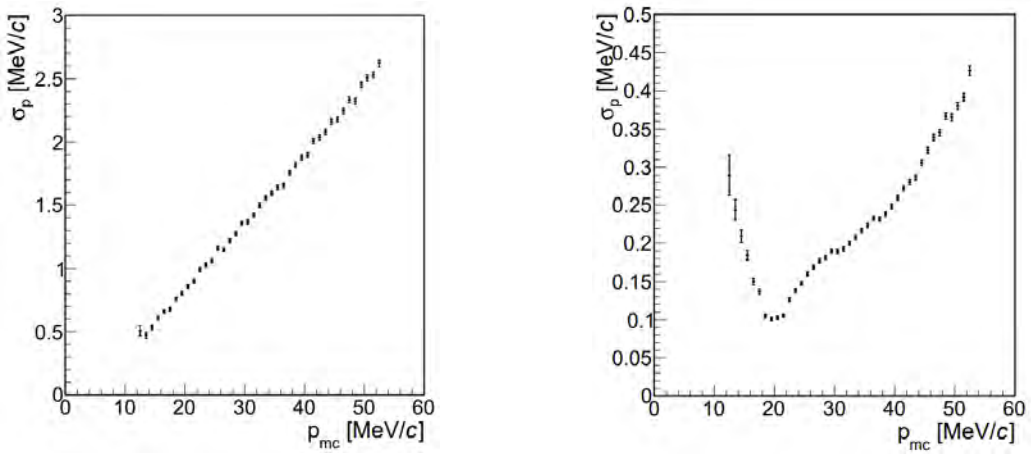

(a) S4 tracks.

(b) L6 tracks.

Figure 8.6: Momentum resolution as a function of the simulated track momentum for S4 and L6 tracks. For L6 tracks the momentum resolution has a minimum for tracks that traverse exactly half a circle outside the outermost pixel layer [28].

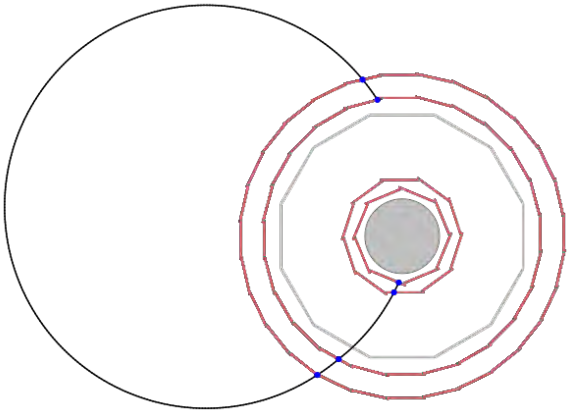

(a) Transverse view.

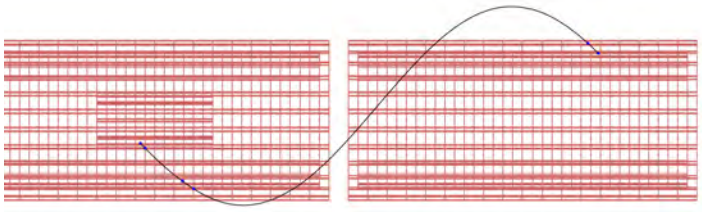

(b) Longitudinal view.

Figure 8.7: An example of an L6 track.

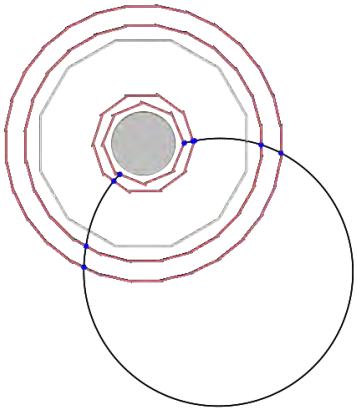

(a) Transverse view.

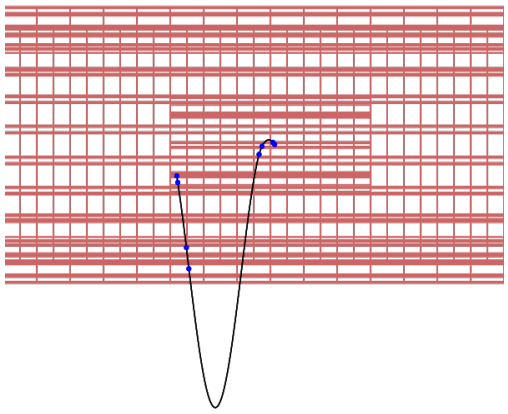

(b) Longitudinal view.

Figure 8.8: An example of an L8o track.

Figure 8.9 shows the χ^2 distributions of all reconstructed S4, L6 and L8o tracks. The more hits a track consists of, the higher the χ^2 value is. This is due to the fact that the scattering effect becomes more dominant as the particle traverses more pixel layers.

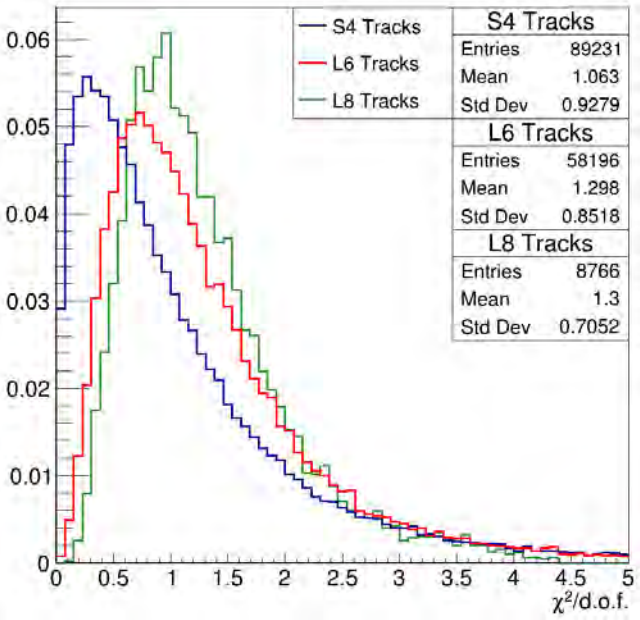

Figure 8.9: χ^2 distributions of reconstructed tracks.

9 | Fake Tracks in Mu3e

Broadly speaking, a ***fake track*** is any track that should not exist. In other words it is any track that should not be used in the vertex fit algorithm. This kind of tracks can be subdivided into two main categories:

1. Fake tracks due to **wrong hit combination** or **noise**.
2. Fake tracks due to **wrong direction of flight**.

Both categories can significantly alter the sensitivity of the experiment as these fake tracks can contribute toward an increase in the background events. The first category, where a fake track is formed due to a wrong hit combination can be very much suppressed by using longer tracks such as L6 & L8o tracks. In fact, by using L6 and L8o tracks the fake rate of this category decreases to less than 1% [46]. An example of a fake triplet due to wrong hit combination is shown in Figure 9.1.

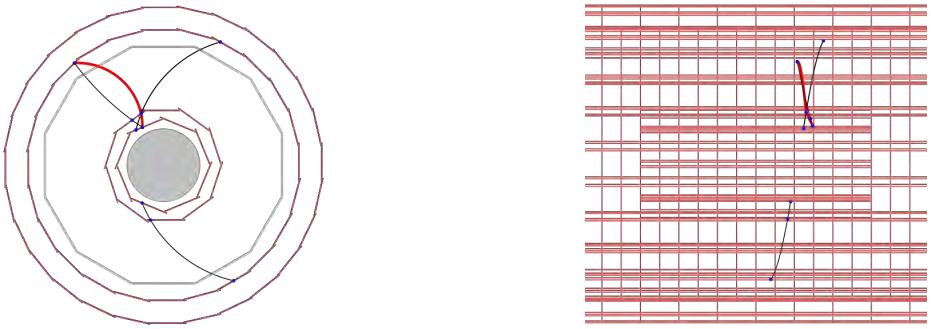

(a) Transverse view. (b) Longitudinal view.

Figure 9.1: An example of a fake triplet (shown in red) due to wrong hit combination.

This chapter focuses only on the second category, where a fake track is formed because there is ambiguity in the direction of flight of the particle. In Mu3e, a right-handed Cartesian coordinate system is chosen with the z-axis pointing in the direc-

tion of the homogeneous magnetic field and the beam. The x and y-axes are defined as horizontal and vertical, respectively. Angles ϕ and λ are shown in Figure 9.2.

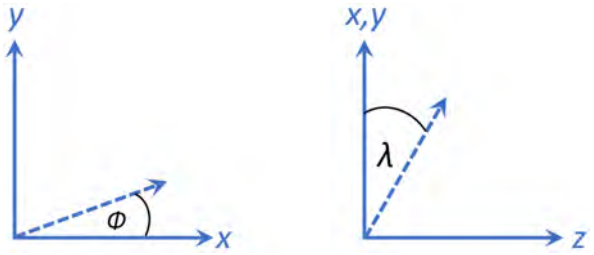

Figure 9.2: Sketch of the ϕ and λ angles.

Charged decay particles, such as positrons and electrons, can make several turns inside the central station of the pixel tracker. This can create ambiguity concerning the direction that the particle travels. In Mu3e reconstruction software, the charge of each particle is assigned solely based the sign of its curvature in the x-y plane. Clockwise travelling particles are assigned a positive curvature/charge and anti-clockwise travelling particles are assigned a negative curvature/charge. Thus particles with opposite curvatures will also have an opposite electric charge, resulting in positrons incorrectly reconstructed as electrons and vice versa. By choice, positrons in Mu3e software are reconstructed as particles with a negative momentum and electrons as particles with a positive momentum. This is shown in Figure 9.3a, and from this one can come to the conclusion that there are quite a lot of electrons in this background sample of events. This of course is not true, as we can see in Figure 9.3b where by looking at the MC particle ID it is apparent that in reality there are hardly any electrons in this sample of events. This simply implies that most of the particles that are reconstructed as electrons in Figure 9.3a in reality are positrons that are incorrectly reconstructed as electrons, i.e. they are fake tracks. In Mu3e, a signal consists of two positrons and one electron, it is therefore extremely important to identify and understand all electrons and all fake electrons must be rejected. By construction, all S4 and L6 tracks are assumed to be outgoing. However for the case of L8o tracks, both directions are saved to the root file for further analysis. Fake S4 tracks simply exist because sometimes the track reconstruction algorithm fails to create an L8o track, so we end up having two outgoing S4 tracks, one of which is fake. For this study a simulated background sample of 20,000 events is used. Figure 9.4 shows the ϕ and λ angle distributions for both real

and fake tracks. The ϕ angle distribution is flat for both types of tracks as one would expect because all directions in the x-y plane are equally probable. However from Figure 9.4b we can see that fake tracks are highly perpendicular to the direction of the magnetic field (z-axis), whereas for the case of real tracks the spread is much larger and covers the whole range of angles. This is also expected because fake tracks are recurling tracks, so in other words they must have small lambda angle in order for the particle to have enough space to recurl back towards the target inside the central station of the pixel tracker. Figure 9.5 shows the λ angle distributions of real and fake S4, L6 and L8 tracks separately.

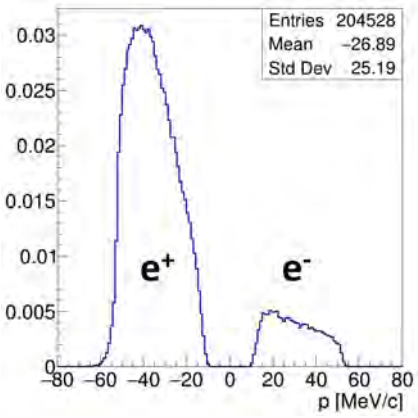

(a) Reconstructed momentum.

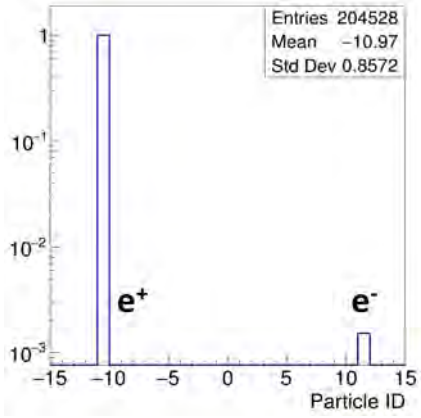

(b) MC particle IDs.

Figure 9.3: Reconstructed momentum and MC ID of all tracks.

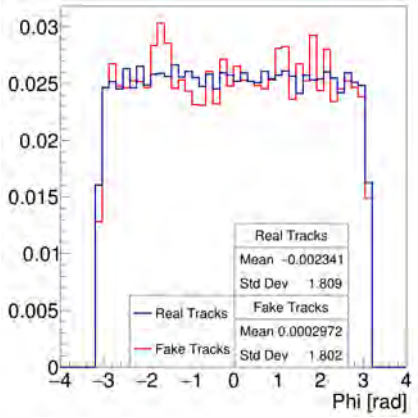

(a) Phi angle distribution.

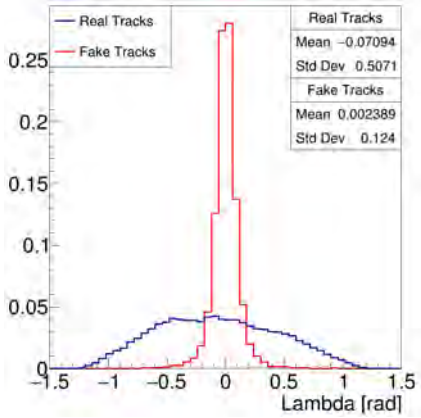

(b) Lambda angle distribution.

Figure 9.4: Phi and lambda angle distributions of all fake and real tracks. Both y-axes are unit-normalised.

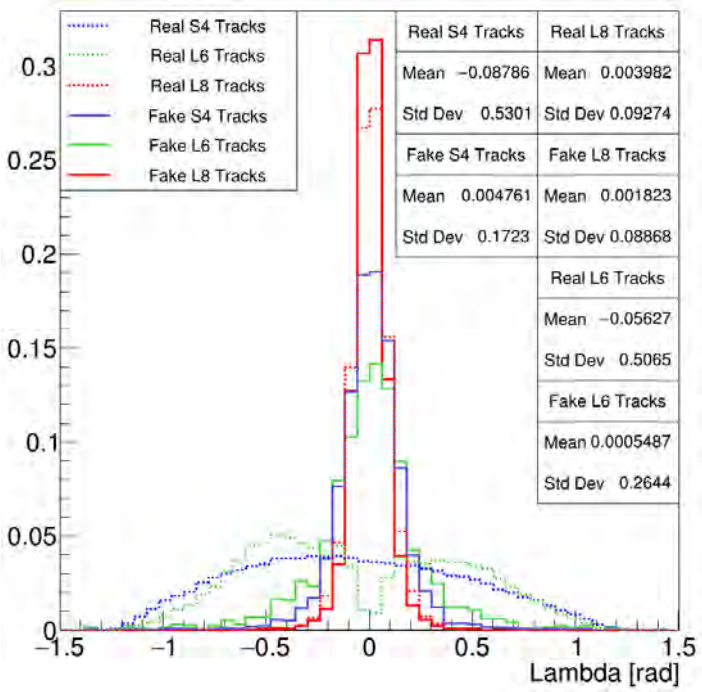

Figure 9.5: Lambda angle distributions of fake and real S4, L6 and L8 tracks.

In the context of this thesis, two algorithms were developed for the detection of fake tracks:

1. Using timing information from the fibre detector.

2. Using a backward helix extrapolation to look for hits and other tracks behind each track.

9.1 Timing Information

The first obvious variable that one can try to use in order to develop a method for the detection of fake tracks, is the timing information from the fibre detector. A fibre hit is assigned to each track, using the following equation:

$$d_{max} = 0.5 \times n \times h + \frac{fb_d}{4} \tag{9.1}$$

where d_{max} is the maximum acceptable distance between a fibre cluster and a track, n is the number of SiPMs that light up, h is the pitch of each SiPM and fb_d is the diameter of a fibre (0.25mm). A fibre hit is matched to the track if the following

criterion is met:

$$|d| < d_{max} \tag{9.2}$$

where $|d|$ corresponds to the distance between the fibre cluster and the track. If $|d| > d_{max}$ then the fibre hit is not being associated to the track. The value of $|d|$ is being calculated using the following equation:

$$|d| = \Delta\phi \times r \tag{9.3}$$

where $\Delta\phi$ is the difference between the azimuthal angle of the cluster and the track and r is the radius at which the fibre cluster lies. We can then use this information to try to identify the direction of flight of each particle. However this method can only be used for L8o tracks which have two fibre hits associated with them, as shown in Figure 9.6. Figure 9.7 shows the time difference versus the helical path distance between the two fibre hits of all L8o track with two fibre hits in the background sample of events. The time difference between the two fibre hits also correlates with the track's total and transverse momentum, as shown in Figure 9.8a and Figure 9.8b respectively. This is due to the fact that tracks with higher momentum have a larger radius in the x-y plane resulting in a larger time difference.

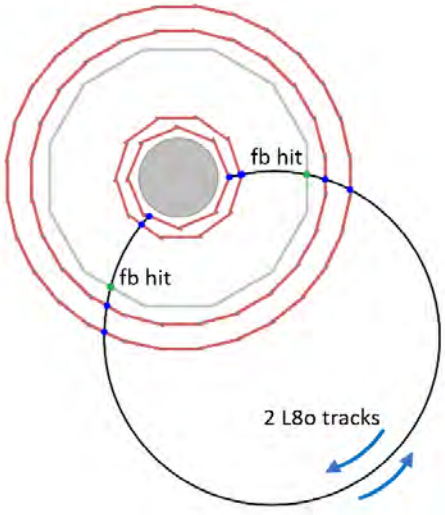

Figure 9.6: An example of an L8o track with two fibre hits (shown in green) associated with it. Due to ambiguity in the direction of flight both directions are saved, one of which is fake. The timing algorithm can be used in this case.

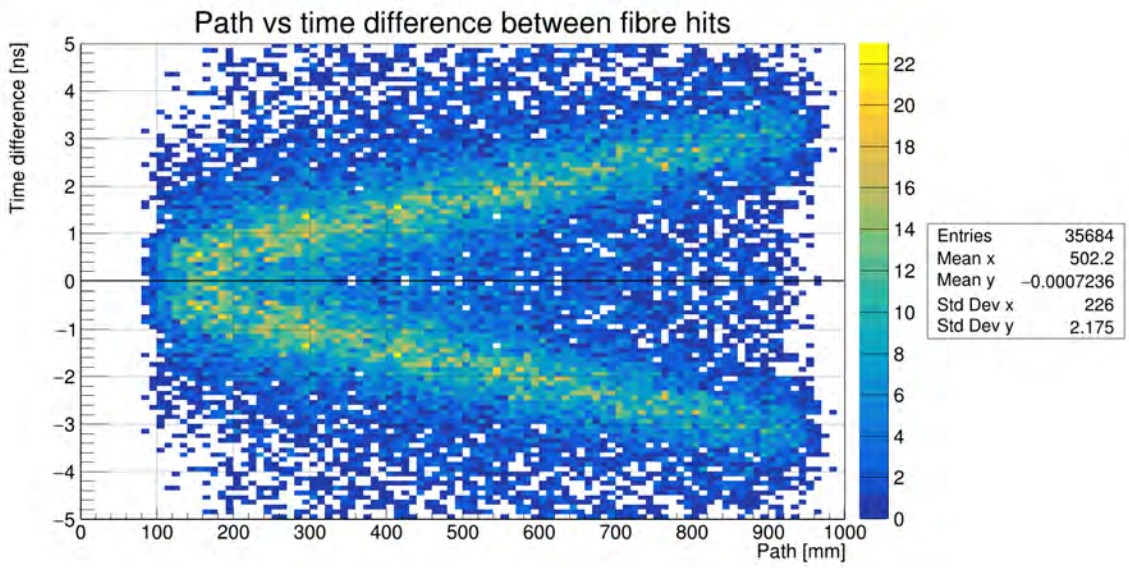

Figure 9.7: Time difference between fibre clusters assigned to 8-hit long tracks as a function of the distance between them along the trajectory of the particle.

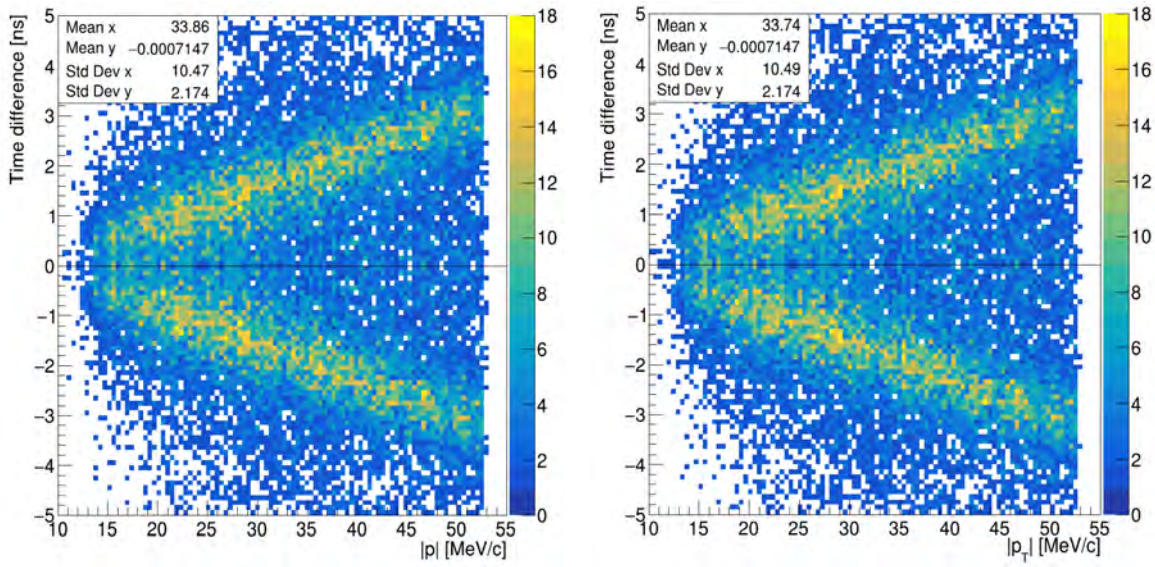

(a) (b)

Figure 9.8: Time difference between the two fibre hits as a function of (a) the total momentum and (b) the transverse momentum of each track.

In a perfect world, all fake tracks should have a time difference between the two fibre hits less than 0 and all real tracks greater than 0. In other words all fake tracks should be below the 0 line on the vertical axis and all real tracks above the 0 line. However this is not always the case and there are two main reasons that account for this. The first reason is that the fibre detector has a certain resolution, meaning

that not all fibre hits are distinguishable in time. The second reason is that highly perpendicular tracks can make several turns and as a result the order of the fibre hits can get mixed up. In the context of this thesis the algorithm shown in Figure 9.9 was developed as a first attempt to detect fake tracks.

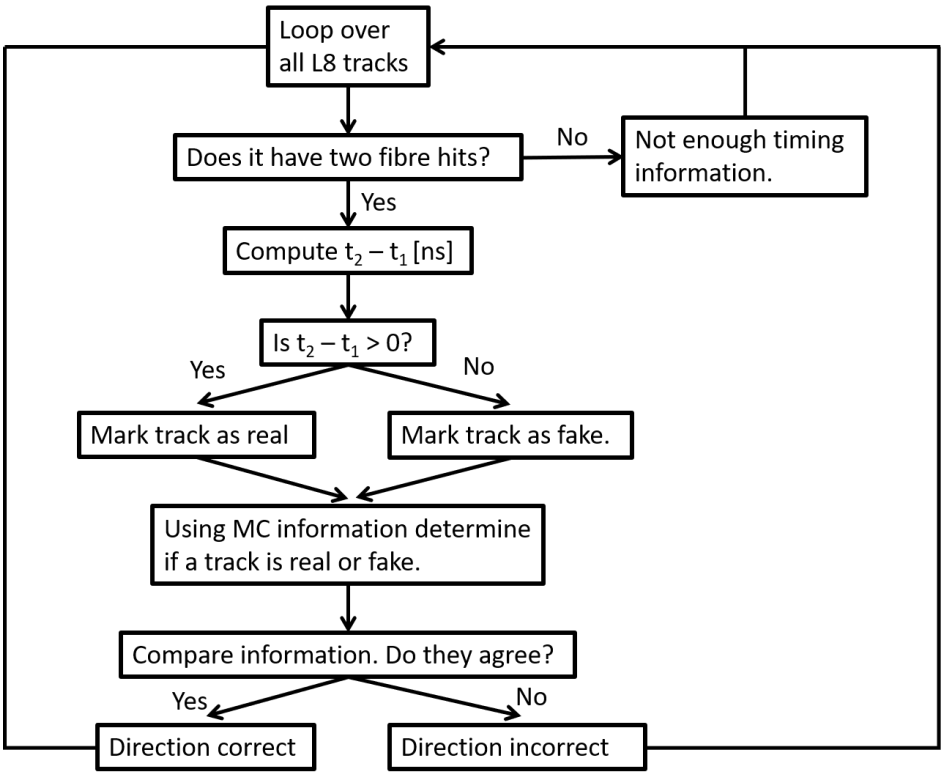

Figure 9.9: Algorithm to detect fake tracks using timing information from the fibre detector.

Using this algorithm we can correctly assign the direction to 83% of all L8o tracks. Incorrect assignment of direction accounts for the rest 17% of the tracks. In other words, if an L8o track has a time difference between its two fibre hits greater than 0, there is 83% chance being a real track and 17% chance being a fake track. The opposite is true if the time difference between the two fibre hits is less than 0. Most of the tracks with an incorrect direction of travel are highly perpendicular tracks with a very small time difference between the two fibre hits. The opposite is true for real tracks, i.e. most of them are not perpendicular tracks and the fibre timing information can provide us with reliable information that can be used to deduce the direction of the track. It is very clear that tracks which are highly perpendicular to the z-axis (small lambda angle) are the hardest to deal with as they can make tens of turns

inside the central pixel tracker and as a result the timing information from the fibre detector is not always very reliable. The efficiency of this method depends on the path length between the two fibre hits, as shown in Figure 9.10. The greater the path length is, the greater the efficiency. This is due to the fact that the timing information from the fibre detector becomes much more reliable as the path length increases. Due to limiting factors in this algorithm, one can try utilising the second algorithm developed for the detection of fake tracks, which is based on a backward helix extrapolation.

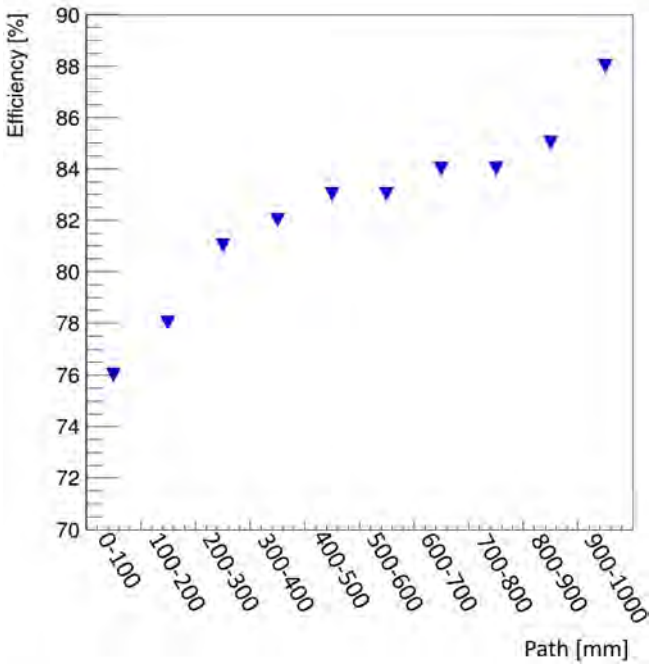

Figure 9.10: Efficiency of assigning the correct charge to each track as a function of the path length between the two fibre hits.

9.2 Helix Extrapolation

The second algorithm is more sophisticated and it is based on extrapolating the helix backwards from each track and look for other tracks or hits. The great advantage of this method over the first one is that it can be used for all kinds of tracks (S4,L6,L8o) and it does not require any timing information from the fibre detector. Each track is extrapolated backwards using the track parameters at the first pixel layer (first hit). Due to the fact that fake tracks are actually ingoing tracks, this implies that all fake tracks should have other tracks or at least some hits behind them.

In other words they must have hits very close to the extrapolated helix. On the other hand real tracks should have no other tracks or hits behind them since they are all outgoing. In the context of this thesis a two-step algorithm was developed utilising the helix extrapolation method for the detection of fake tracks, shown in Figure 9.11.

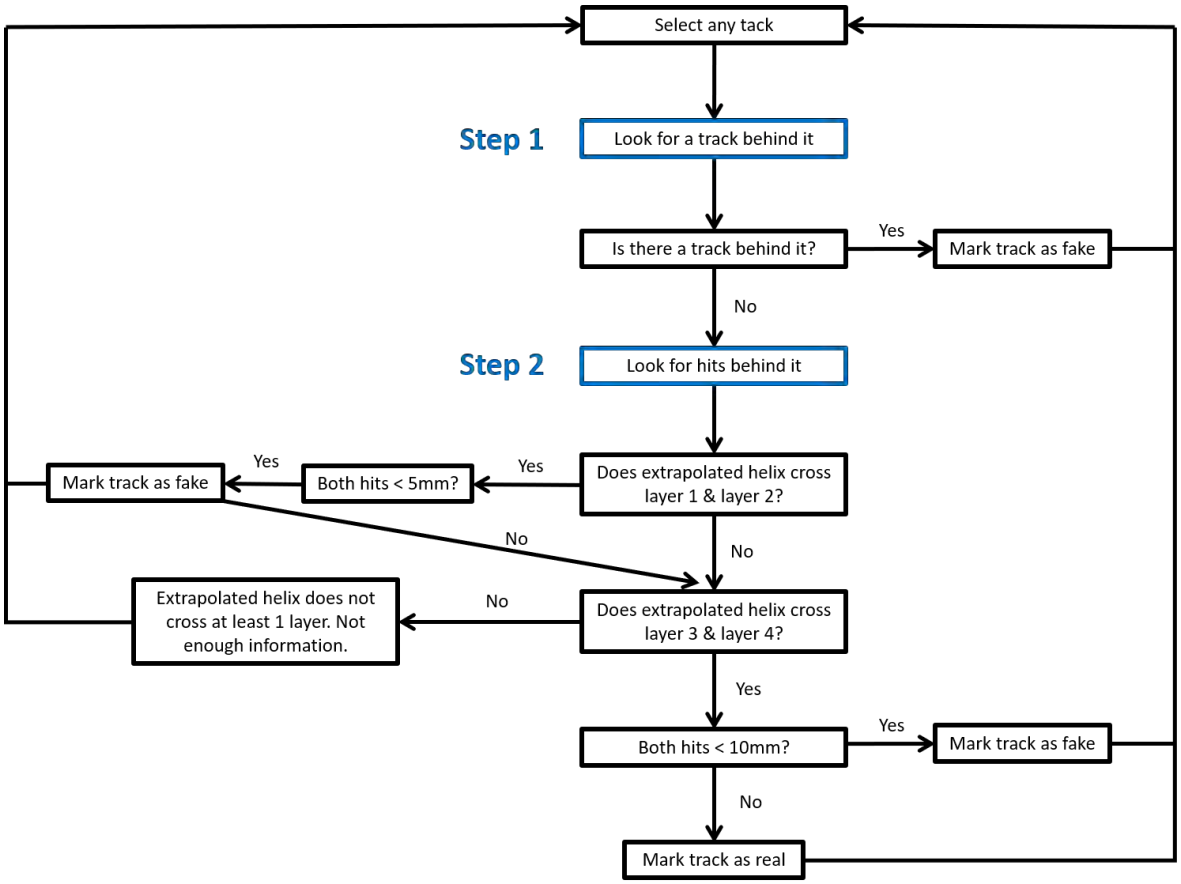

Figure 9.11: Backward helix extrapolation algorithm for the detection of fake tracks.

In the first step, the algorithm only searches for other tracks behind the track, on the other side of the tracker. If a track is indeed matched to a track in the backward direction, an inner L8 track is formed (L8i), as shown in Figure 9.12. This simply means that the particle is ingoing and it continues its trajectory on the other side of the pixel tracker. In this case it means that the track did not start on this turn. To match a track, we loop over all tracks in the time frame and certain criteria must be met in the following order:

1. The two tracks must have opposite curvature signs.

2. The difference between the two Φ angles of the first hit of each track, $|\Phi_1 - \Phi_2| < 0.5$ rad.

3. The longitudinal distance between the first hit of each track, $|z_1 - z_2| < 10$ mm.
4. The significance of the curvature difference, $sk = \frac{|k_1+k_2|}{\sqrt{k_{1,err}^2+k_{2,err}^2}} < \frac{1}{10}$
5. The χ^2 of the final L8i track must be less than 48.

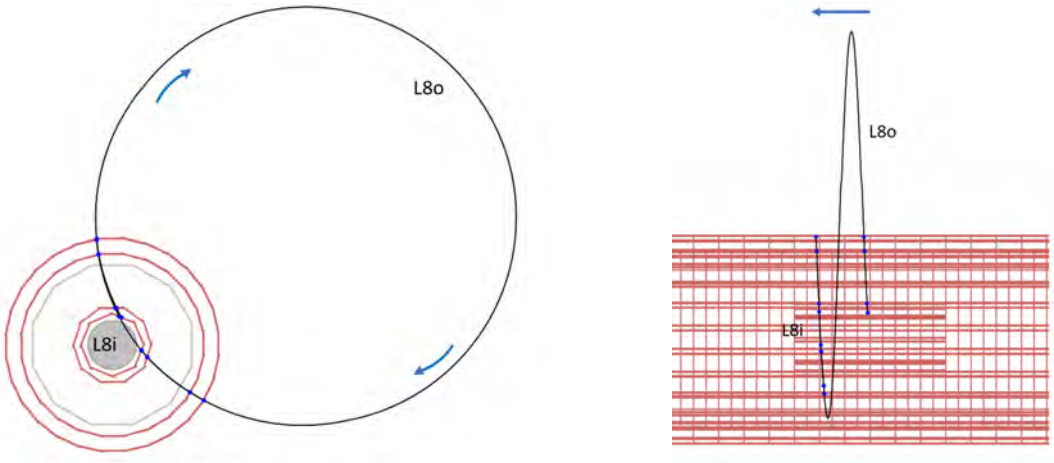

(a) Transverse view.

(b) Longitudinal view.

Figure 9.12: An example of an inner L8 (L8i) track. Arrows indicate the direction of flight of the real track.

The second step of this algorithm is the search for hits behind the track. This is the case where for example there is no track behind because the track did not pass the χ^2 criterion. In this case we have no option left other than looking for hits. The helix is extrapolated on all four pixel layers and the distance to the closest hit on each layer is saved for further analysis. Figure 9.13 shows the distance from the extrapolated helix to the closest hit on each layer for both real and fake tracks, where real and fake tracks are selected using the MC information (particle ID) and the sign of the reconstructed momentum. It is apparent that fake tracks have hits very close to the extrapolated helix on all four pixel layers, as one would expect and that the hits get further away from the extrapolated helix as we go from the first layer to the fourth layer. This is because the ingoing particle can pass through the target before continuing its trajectory on the other side of the pixel tracker, undergoing scattering and altering the trajectory of the particle. Thus the backward helix will not match exactly with the true trajectory. This is the reason why a cut of 5mm is chosen for

layers 1 & 2 and 10mm for layers 3 & 4. Real tracks on the other hand, most of the times do not have hits close to the helix, as one would also expect. However from Figure 9.13 we can see that some real tracks do have hits close to the helix. This is due to the fact that some real tracks are highly perpendicular to the magnetic field, with a very small lambda angle. In this case the extrapolated helix detects hits that are part of the track from a later turn in time. This is one of the main limiting factors of this method. By applying the algorithm shown in Figure 9.11 we can correctly assign the direction to 89% of the reconstructed tracks. This outcome is slightly higher than the previous algorithm but it has the advantage of including all types of tracks.

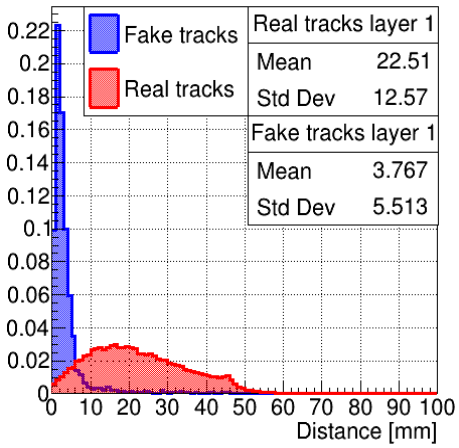

(a) Layer 1.

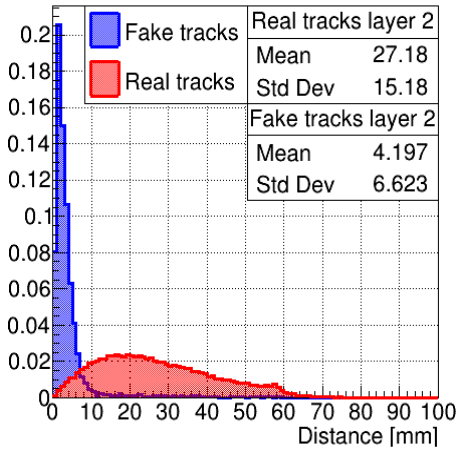

(b) Layer 2.

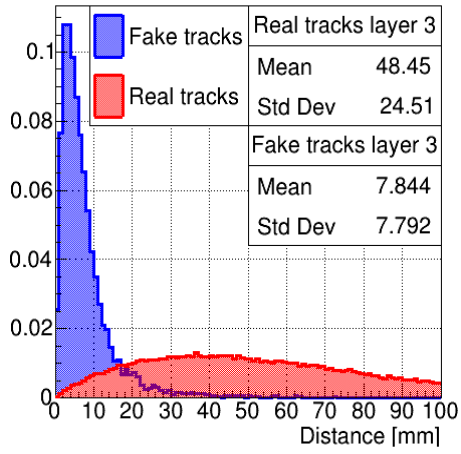

(c) Layer 3.

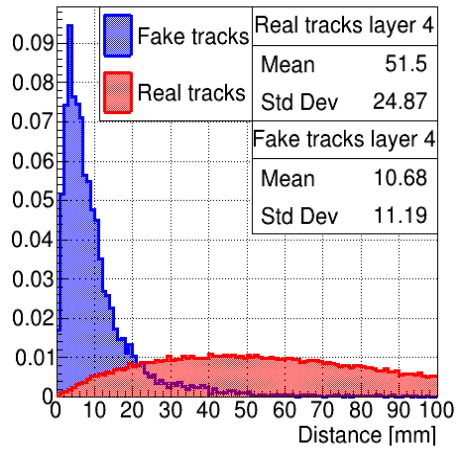

(d) Layer 4.

Figure 9.13: Distance of the closest hit to the extrapolated helix for each pixel layer. Fake tracks are shown in blue and real tracks are shown in red. The simulated muon rate is $10^8 \mu^+/\text{s}$.

9.3 Summary

The presence of fake tracks is a known problem for Mu3e. Both algorithms have shown that they are capable of correctly assigning track directions to over 80% of the tracks, but they essentially both fail to deal with perpendicular tracks having a lambda angle < 0.1 rad. Results are summarised in Table 9.1. This is of course far from what Mu3e requires as the rest of the tracks with a wrong direction can create a very large amount of backgrounds. From this study it is also clear that there is no single "magic remedy" that one can use to correctly assign a track direction to all tracks. This requires more work and further investigation by the collaboration in the future. In the future it might be also necessary to simply discard perpendicular tracks to keep the fake rate low but this will also decrease the sensitivity of the experiment. These kind of tracks is a known problem for Mu3e, due to the high occupancy in the central pixel tracker, resulting in tens or hundreds of hits adding more to the confusion to the reconstruction. Both methods can yield a higher efficiency by simply rejecting tracks having a lambda angle between -0.1 and 0.1 rad. Ignoring these tracks increases the efficiency but it must be noted that a certain amount of tracks is discarded. By using first the helix extrapolation method and then the timing information the efficiency increases slightly by 1% when compared to the helix extrapolation method alone.

Algorithm	Tracks	Correct assignment of direction [%]	Incorrect assignment of direction [%]
Timing	All	83	17
Information	$\|\lambda\| > 0.1$ rad	89	11
Helix	All	88	12
Extrapolation	$\|\lambda\| > 0.1$ rad	96	4
Helix Extr. then	All	89	11
Timing Info.	$\|\lambda\| > 0.1$ rad	97	3

Table 9.1: Summary of the results from the two algorithms for the detection of fake tracks.

A Magnet Cooldown

In total three cooldowns were carried out. The second and third cooldowns are shown in Figure A.1 and Figure A.2 respectively. For the third cooldown, the cooldown time is greater due some technical problems with the helium supply of one of the four compressor units.

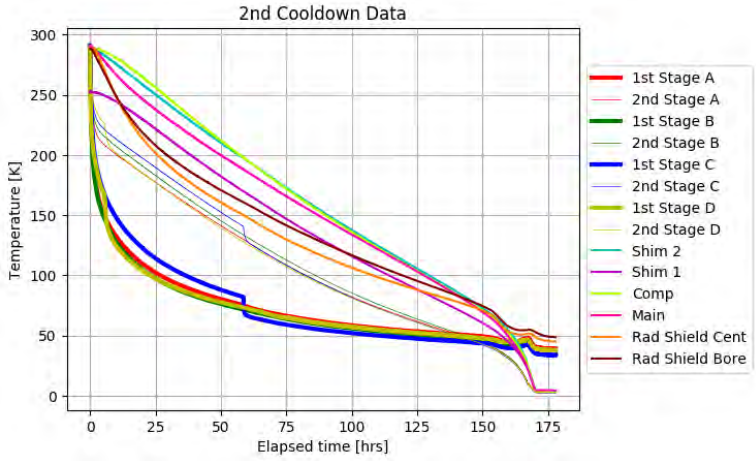

Figure A.1: Second cooldown of the Mu3e magnet.

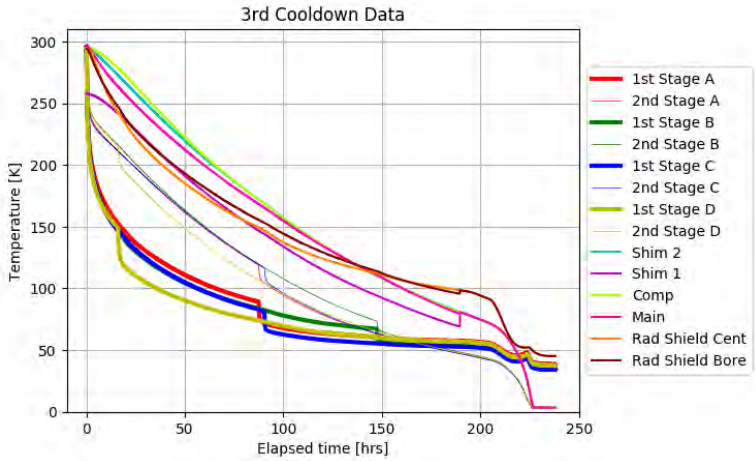

Figure A.2: Third cooldown of the Mu3e magnet.

B | Beamline Elements

All dipole and quadrupole magnets were simulated according to the 2018 CMBL setup, as shown in Table B.1.

Element	Current [A]
QSK41	20.4
QSK42	-40.5
QSK43	28.8
SML41	-22.2
ASL41	-73.9
QSO41	34.0
QSO42	-10.8
ASK41	-91.5
QSM41	-107.6

Table B.1: Amount of current for each beamline element used in the beamline simulation.

Colophon

This document was composed on Overleaf with Helvetica font of size 12 pt and line spacing of 1.5. All Feynman diagrams were generated using JaxoDraw Java software. Figures were created using ROOT, Matplotlib library for Python, Mathematica and MS PowerPoint, except those taken from other sources.

Bibliography

[1] D. Laërtius, *"Lives of the Eminent Philosophers"*, vol. IX, 44.

[2] R. Ade *et al.*, "Planck 2015 results - xiii. cosmological parameters," *A&A*, vol. 594, p. A13, 2016.

[3] A. D. Sakharov, "Violation of cp invariance, c asymmetry, and baryon asymmetry of the universe.," *JETP Lett. (USSR)(Engl. Transl.), 5: 24-7(Jan. 1, 1967).*

[4] C. Patrignani *et al.*, *"Review of Particle Physics"*, vol. In: Chin. Phys. C40.10 (2016), p.100001.

[5] J. Hewett *et al.*, "Fundamental physics at the intensity frontier," *Argonne National Laboratory*, pp. 1–223, 2012.

[6] P. G. L. Leach *et al.*, "Noether's theorem and symmetry," *arXiv e-prints*, p. arXiv:1812.03682, Dec 2018.

[7] Y. Fukuda *et al.*, "Evidence for oscillation of atmospheric neutrinos," *Phys. Rev. Lett.*, vol. 81, pp. 1562–1567, Aug 1998.

[8] F. P. An *et al.*, "Improved measurement of electron antineutrino disappearance at daya bay.," *Chinese Physics C*, vol. 37, p. 011001, Jan 2013.

[9] Y. Kuno *et al.*, "Muon decay and physics beyond the standard model," *Reviews of Modern Physics*, vol. 73, p. 151–202, Jan 2001.

[10] U. Bellgardt *et al.*, "Search for the decay $\mu^+ \to e^+e^+e^-$," *Nuclear Physics B*, vol. 299, no. 1, pp. 1–6, 1988.

[11] M. Aoki, "An experimental search for muon-electron conversion in nuclear field at sensitivity of 10^{14} with a pulsed proton beam," 2012.

[12] J. Abrams *et al.*, "Mu2e conceptual design report," *arXiv e-prints*, p. arXiv:1211.7019, Nov 2012.

[13] A. M. Baldini *et al.*, "Measurement of the radiative decay of polarized muons in the meg experiment," *The European Physical Journal C*, vol. 76, Feb 2016.

[14] W. H. Bertl *et al.*, "A Search for muon to electron conversion in muonic gold," *Eur. Phys. J. C*, vol. 47, pp. 337–346, 2006.

[15] W. J. Marciano *et al.*, "Charged lepton flavor violation experiments," *Annual Review of Nuclear and Particle Science*, vol. 58, no. 1, pp. 315–341, 2008.

[16] A. Baldini *et al.*, "MEG Upgrade Proposal," *arXiv e-prints*, p. arXiv:1301.7225, Jan. 2013.

[17] A. Blondel *et al.*, "Research proposal for an experiment to search for the decay $\mu \rightarrow$ eee," no. 1301.6113, 2013.

[18] R. Abramishvili *et al.*, "COMET Phase-I technical design report," *Progress of Theoretical and Experimental Physics*, vol. 2020, Mar 2020.

[19] L. Bartoszek *et al.*, "Mu2e technical design report," *arXiv e-prints*, Jan. 2015.

[20] Z. Maki *et al.*, "Remarks on the Unified Model of Elementary Particles," *Progress of Theoretical Physics*, vol. 28, pp. 870–880, 11 1962.

[21] C. Albright *et al.*, "Physics at a neutrino factory," *arXiv e-prints*, pp. arXiv:hep–ex/0008064, Aug. 2000.

[22] G. H. Tomé, "Revisiting the flavor violating decays of the Tau and Mu leptons in the Standard Model with massive neutrinos," *SciPost Phys. Proc.*, p. 17, 2019.

[23] M. Tanabashi *et al.*, "Review of particle physics," *Phys. Rev. D*, vol. 98, p. 030001, Aug 2018.

[24] Capozzi *et al.*, "Global constraints on absolute neutrino masses and their ordering.," *Phys. Rev. D*, vol. 95, p. 096014, May 2017.

[25] F. Borzumati *et al.*, "Large muon- and electron-number nonconservation in supergravity theories," *Phys. Rev. Lett.*, vol. 57, pp. 961–964, Aug 1986.

[26] M. Aiba *et al.*, "Science case for the new high-intensity muon beams himb at psi," *arXiv e-prints*, p. arXiv:2111.05788, Nov. 2021.

[27] M. Tanabashi *et al.*, "Review of particle physics," *Phys. Rev. D*, vol. 98, p. 030001, Aug 2018.

[28] K. Arndt *et al.*, "Technical design of the phase I mu3e experiment," *Nuclear Instruments and Methods in Physics Research Section A: Accelerators, Spectrometers, Detectors and Associated Equipment*, vol. 1014, p. 165679, Oct 2021.

[29] I. Perić, "A novel monolithic pixelated particle detector implemented in high-voltage cmos technology," *Nucl.Instrum.Meth.*, vol. A582, 2007.

[30] R. Akhmetshin *et al.*, "The proton accelerator at the paul scherrer institute: Forty years of top-flight research.," *www.psi.ch/en/media/our-research/the-proton-accelerator-forty-years-of-top-flight-research*, 2014.

[31] F. A. Berg, "CMBL - a high-intensity muon beam line scintillation target with monitoring system for next-generation charged lepton flavour violation experiments.," *[PhD Thesis]*, 2017.

[32] S. Corrodi, "A timing detector based on scintillating fibres for the mu3e experiment," *PhD thesis. ETH Zürich*, 2018.

[33] Y. Munwes, "Tile detector - preliminary testbeam results," *Talk at an internal Mu3e collaboration meeting*, 2018.

[34] D. vom Bruch, ""pixel sensor evaluation and online event selection for the mu3e experiment," *https://doi.org/10.11588/heidok.00023689*, Nov 2017.

[35] N. Berger *et al.*, "The mu3e data acquisition," *arXiv e-prints*, p. arXiv:2010.15648v2, Jan 2021.

[36] S. Agostinelli *et al.*, "Geant4–a simulation toolkit," *Nuclear Instruments and Methods in Physics Research Section A*, pp. 250–303, 2003.

[37] Cryogenic, "Cryogen free magnet system for mu3e," 2020.

[38] P. Elleaume *et al.*, “Computing 3D magnetic fields from insertion devices,” vol. 3, pp. 3509–3511 vol.3, 1997.

[39] J. Adam *et al.*, “The MEG detector for $\mu \rightarrow e\gamma$ decay search,” *al., The European Physical Journal C*, Nov 2012.

[40] M. Seidel *et al.*, “Production of a 1.3 mw proton beam at psi,” *IPAC 2010 1st International Particle Accelerator Conference*, June 2010.

[41] Heidenreich, “Carbon and beryllium targets at psi.,” *AIP Conference Proceedings, https://doi.org/10.1063/1.1522602*, Nov 2002.

[42] O. B. van Dyck *et al.*, “Cloud and surface muon beam characteristics,” *IEEE Transactions on Nuclear Science*, vol. 26, no. 3, pp. 3197–3199, 1979.

[43] T. Roberts, “G4beamline user’s guide,” *http://g4beamline.muonsinc.com*, Feb 2017.

[44] Z. D. Hodge, “Production, characterization, and monitoring of surface muon beams for charged flavor lepton violation experiments.,” 2018.

[45] C. Elliott *et al.*, “National instruments labview: A programming environment for laboratory automation and measurement,” *Journal of The Association for Laboratory Automation*, vol. 12, pp. 17–24, Feb 2007.

[46] Kozlinskiy, Alexandr, “Track reconstruction for the mu3e experiment based on a novel multiple scattering fit,” *EPJ Web Conf.*, vol. 150, p. 00005, 2017.